Università degli Studi di Palermo

AREA RICERCA E TRASFERIMENTO TECNOLOGICO
SETTORE DOTTORATI E CONTRATTI PER LA RICERCA
U. O. DOTTORATI DI RICERCA

PhD Course in Technologies and Science for Human Health
Department of Biological, Chemical and Pharmaceutical Sciences and Technologies
SSD – CHEM-07/A

Investigation on MMACHC pathological mutants involved in *cblC* disease, a rare inborn metabolic disorder of vitamin B12

PhD CANDIDATE
Lisa Longo

PhD COURSE COORDINATOR
Prof. Valeria Vetri

SUPERVISOR
Prof. Marco Tutone

CO-SUPERVISORS
Dott. Vincenzo Martorana
Dott. Silvia Vilasi

XXXVIII CYCLE
2024/2025 ACADEMIC YEAR

Abstract

The *cblC* disease is a rare inborn disorder of the vitamin B12 (cobalamin, Cbl) metabolism characterized by combined methylmalonic aciduria and homocystinuria. The clinical consequences are heterogenic and severe, and even when early treated with current therapies, the affected children manifest neurocognitive, ophtalmological and cardiovascular dysfunctions.

The molecular genetic cause of the disease was found in the mutations the *MMACHC* gene coding for MMACHC, a 282 amino acid protein responsible for the intracellular trafficking and processing of the various forms of Cbl.

Although the crystal structure of the wild-type protein (WT) has been solved, many molecular features of MMACHC physiopathology remain to be understood and a study on the effect of each specific pathogenic mutation on the resulting protein is still lacking.

In this PhD thesis we present a comprehensive methodological approach for the biophysical characterization of MMACHC-WT and the MMACHC-R161Q variant, resulting from the most frequent missense pathological mutation found in *cblC* patients.

The recombinant MMACHC-WT protein produced in *Escherichia coli* was first characterized using circular dichroism, UV-visible absorbance, fluorescence spectroscopy, molecular dynamics, size exclusion chromatography and native gel electrophoresis. These analyses provided a detailed description of the protein's secondary and tertiary structure, stability, oligomerization propensity, and ability to correctly process Cbl. The same experimental pipeline was applied to the MMACHC-R161Q variant, revealing a different stability and an impaired dimerization, that directly correlate to its reduced enzymatic activity. These results were further enriched by calorimetric studies: differential scanning calorimetry unveiled a complex thermal unfolding pathway that is significantly different among the two variants, while isothermal titration calorimetry directly quantified the binding of the two proteins to the natural ligands, confirming the weaker interactions established by MMACHC-R161Q, and provided the thermodynamic parameters governing these interactions. Moreover, we demonstrated as a proof-of-principle that the use of non-specific stabilizers (osmolytes) can partially restore functionality in MMACHC-R161Q, establishing the basis for a therapeutic treatment based on protein stabilization. In this framework, we also performed an *in silico* screening of drug-like

small molecules to identify potential pharmacological chaperones, followed by an *in vitro* evaluation of their effects on the isolated protein.

Taken together, these results provide a molecular interpretation of the MMACHC-R161Q pathogenic mechanism and establish a biophysical platform suitable for investigating disease-causing variants. This comparative approach also provided the opportunity to investigate previously unexplored biophysical aspects of the wild-type enzyme, thereby deepening our understanding of the molecular mechanisms responsible for MMACHC function and dysfunction. Our results not only advance the current knowledge of the alterations underlying the disease but also represents the first step toward the rational design of personalized therapeutic strategies. Furthermore, the biophysics-based methodological toolbox presented here may be extended to the study of other rare disorders sharing similar molecular mechanisms driving the pathogenic events.

Preface

This PhD thesis entitled “Investigation on MMACHC pathological mutants involved in cblC disease, a rare metabolic disorder of vitamin B12 metabolism” was submitted to the Department of Biological, Chemical and Pharmaceutical Science and Technologies at the University of Palermo to obtain the PhD degree in Technologies and Sciences for Human Health. The research project was carried out in the molecular biology and biophysics laboratories of the Institute of Biophysics (IBF) of the National Research Council (CNR), under the supervision of Dr. Vincenzo Martorana and Dr. Silvia Vilasi, and in the Computational Medicinal Chemistry laboratory of the Department of Biological, Chemical and Pharmaceutical Science and Technologies of the University of Palermo under the supervision of Prof. Marco Tutone.

During the PhD program, I completed a six-month research stay abroad at the Institute of Biocomputation and Physics of the Complex Systems (BIFI) in Zaragoza, Spain, part of the MOSBRI Infrastructure. The research, focused on calorimetric analysis, was carried out under the supervision of Prof. Adrian Velazquez Campoy.

The following research papers resulted from the work of this PhD project:

- S. Vilasi on behalf of L. Longo, L. Randazzo, M. Bollati, R. Carrotta, M. A. Costa, M. De Rosa, M. R. Mangione, V. Martorana, M. Milani, M. G. Ortore, M. Tutone, R. Passantino, *Studying an orphan disease by a biophysical approach: The case of cblC*, 2024, Il Nuovo Cimento C 47, 318 10.1393/ncc/i2024-24318-2

- L. Longo, L. Randazzo, M. Bollati, R. Carrotta, M. A. Costa, M. De Rosa, M. R. Mangione, V. Martorana, G. Culletta, M. Tutone, E. Mari, M. G. Ortore, P.M. Garcia-Franco, A. VelazquezCampoy, R. Passantino, S. Vilasi, *Missense mutations in MMACHC protein from cblC disease affect its conformational stability and vitamin B12-binding activity: The example of R161Q mutation*, 2025, Molecular Genetics and Metabolism, 145, 3, 109150 https://doi.org/10.1016/j.ymgme.2025.109150

- L. Longo, M. A. Costa, R. Carrotta, M. De Rosa, M. R. Mangione, V. Martorana, M. Tutone, M. G. Ortore, P.M. Garcia-Franco, S. Vega, A. Velazquez-Campoy, R. Passantino, S. Vilasi, *Modulation of conformational features and oligomerization of MMACHC by cobalamin variants: impact of the R161Q mutation in cblC disease*, 2025, European Biophysics Journal https://doi.org/10.1007/s00249-025-01777-5

Table of contents

List of common abbreviations

Cbl	cobalamin
AdoCbl	5-deoxyadenosylcobalamin
CNCbl	cyanocobalamin
MeCbl	methylcobalamin
OHCbl	hydroxocobalamin
DMB	5.6-dimethylbenzimidazole
GSH	gluthatione
cblC	complementation group C of the cobalamin metabolic disorders
MMACHC	methylmalonic aciduria cblC type with homocysteinuria protein
E. coli	Escherichia coli
BN-PAGE	blue native polyacrylamide gel electrophoresis
SDS-PAGE	sodium dodecyl sulphate polyacrylamide gel electrophoresis
CD	circular dichroism
DSC	differential scanning calorimetry
ITC	isothermal titration calorimetry
MD	molecular dynamics
SEC	size exclusion chromatography

1. Introduction

This chapter provides a general introduction to cobalamin (vitamin B12) and its central role in human metabolism. MMACHC, a key protein in the intracellular processing of vitamin B12 and the main focus of this research, is then introduced, as its pathogenic mutations cause the rare inherited disorder known as *cblC* disease. The structural and biochemical features of MMACHC, together with the pathological variants most frequently associated with the disease, are described. Finally, the current state of the art in the field is then reviewed, highlighting the molecular mechanisms proposed so far.

1.1. Vitamin B12

1.1.1. Chemical structure

Vitamin B12 is a complex organic cofactor and the only known biomolecule with a stable cobalt-carbon bond, which gives the alternative name of cobalamin (Cbl).

Referred as "Nature's most beautiful cofactor" [1], its crystallographic structure was first determined by Dorothy Hodgkins in 1958 [2], for which she was awarded with the Nobel Prize in Chemistry in 1964.

Structurally, vitamin B12 consists of a corrin ring coordinated by its four nitrogen atoms to a central cobalt ion and decorated with three acetamide and four propionamide groups, one of which phosphorylated by a ribose moiety and further connected to a 5,6-dimethylbenzimidazole (DMB). The DMB moiety can serve as a lower axial (α-axial) ligand to the cobalt, determining the *base-on* configuration of cobalamin (Fig. 1A). When this binding does not occur, the DMB forms a flexible tail, and the cobalamin adopts its *base-off* configuration (Fig.1C). The cobalt can be further bound to a variety of upper axial (β-axial) ligands, which determines the specific form of the vitamin, i.e., the natural occuring, hydroxocobalamin (OHCbl), 5-deoxyadenosylcobalamin (AdoCbl), and methylcobalamin (MeCbl) and the synthetic cyanocobalamin (CNCbl) (Fig. 1B) [3].

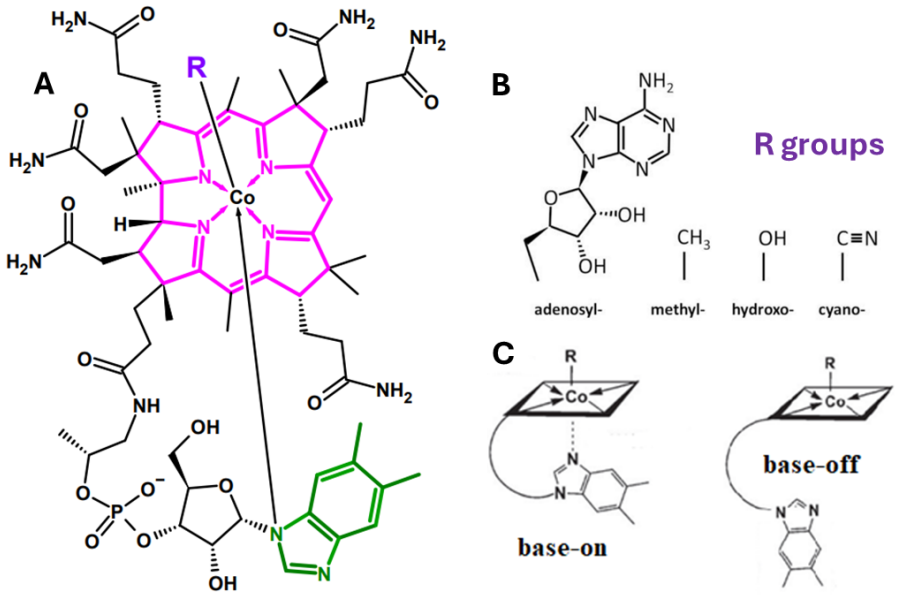

Figure 1. Chemical structure of vitamin B12. **A.** The diagram displays the corrin ring (magenta) system centered around a cobalt ion, flanked by axial ligands including the 5,6-dimethylbenzimidazole group (green) and the β-axial ligand R (violet). **B.** β-axial ligands **C.** Schematic representation of *base-on* and *base-off* configuration of cobalamin

1.1.2. Spectroscopical properties

Vitamin B12 exhibits complex and versatile spectroscopic properties due to its unique tetrapyrrole corrin ring system and central cobalt ion. The absorption spectra are classified by three main bands: two visible bands designated as α and β bands and the NEAR-UV γ band. While the absorption bands are attributed to transitions involving electrons of the conjugated corrin chromophore rather than the cobalt atom itself, they are significantly influenced by the axial ligands bound to the cobalt, making them diagnostic of the form of Cbl in solution [4]. In Fig. 2A spectra of *base-on* OHCbl, CNCbl, AdoCbl and MeCbl are shown. UV-VIS spectra of cobalamins are also a powerful tool to monitor both the conformational *base-on/base-off* transition (Fig. 2B) and the conversion of one cobalamin form into another (Fig. 2C), e.g. after an enzymatic reduction.

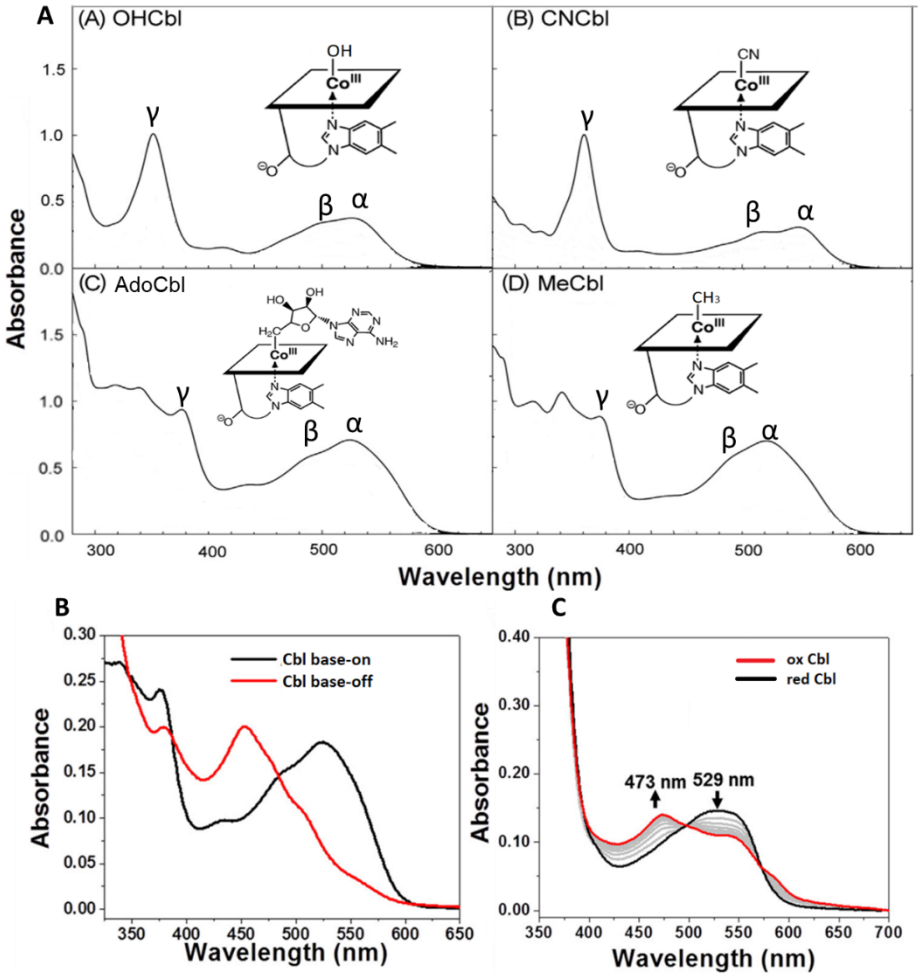

Figure 2. Absorption spectra of different forms of cobalamin. **A.** Spectroscopical differences among OHCbl, CNCbl, AdoCbl and MeCbl. **B.** *base-on/base-off* transition of AdoCbl upon binding to MMACHC **C.** Spectroscopical changes associated with the enzymatic reduction of CNCbl. Panel A adapted from *Juzeniene et al., J Photochem Photobiol B (2013)* and panels B and C adapted from *Li et al., J Biol Chem (2014)*

1.1.3. Gastroenteric absorption

Humans rely on dietary supplements of the vitamin since its biosynthesis is missing in higher organisms, and only few Archaea and Bacteria are able to synthesize it *de novo* [5]. The dietary intake derives from animal sources, with a recommended daily allowance (RDA) of 2.4 µg/day [6]. After its release from dietary proteins, Cbl is bound in the stomach by Haptocorrin (HC) [7], to prevent the acidic gastric hydrolysis. The Cbl is then released from the HC:Cbl complex in the duodenum after the proteolytic pancreatic degradation of HC and bound by the Intrinsic Factor (IF) [8], forming a complex required for receptor-mediated endocytosis in the terminal ileum via the cubam receptor. Once inside the enterocyte, the IF is degraded and the Cbl is released in the bloodstream via multidrug resistance protein 1 (MDR1) [9], where it binds its systemic carrier transcobalamin (TC) [10]. A graphical representation of cobalamin absorption is presented in Fig. 3.

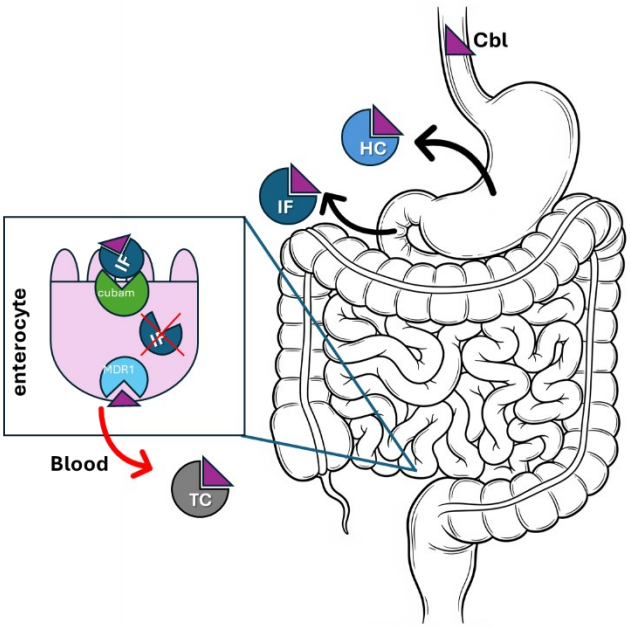

Figure 3. Graphical representation of cobalamin gastro-enteric absorption. Cobalamin is represented as a purple triangle and enzymes as coloured circles

1.1.4. Intracellular metabolism

In mammals, vitamin B12 plays an essential role in DNA synthesis and in the catabolism of both odd-chain fatty acids and branched-chain amino acids, serving as a cofactor for cytosolic Methionine Synthase (MS) in the form of MeCbl and for mitochondrial Methylmalonyl-CoA Mutase (MUT) in the form of AdoCbl [11].

Although only two enzymes utilize Cbl as a cofactor, the cobalamin metabolic pathway is complex and involves several different proteins, each of them responsible for transporting and/or processing a specific conformation of Cbl [12]. The circulating TC:Cbl is internalized by receptor-mediated endocytosis after the recognition of the complex by the TC-receptor (TCR) on the cell surface, followed by the lysosomal acidic degradation of the TC [13]. The free Cbl is released from the lysosome via two integral membrane proteins: lipocalin-1 interacting membrane receptor domain-containing protein 1 (LMBD1) and adenosine triphosphate (ATP)-binding cassette subfamily D member 4 (ABCD4) [14]. Impaired function of either protein results in lysosomal accumulation of free Cbl and is associated with the inherited defects *cblF* (LMBD1) and *cblJ* (ABCD4) [15]. The cytosolic entry of the Cbl is mediated by MMACHC (methylmalonic aciduria type C and homocystinuria protein), responsible for processing and transporting whatever form of cobalamin it encounters. Deficiency of MMACHC is associated with the inherited defect *cblC* [16]. The transport of MMACHC-processed Cbl to the final users requires MMADHC (methylmalonic aciduria type D and homocystinuria protein), associated with the *cblD* defect [17]. The formation of the MMACHC:Cbl-MMADHC heterodimer guarantees the delivery of the cobalamin to the end-

users [18], [19], which are MS and MUT, associated with *cblG* [20] and *inherited methylmalonic aciduria (mut)* [21] respectively. In the cytosol the MS catalyzes the methylation of homocysteine involving the transfer of a methyl group from 5-methyltetrahydrofolate to Cbl in the +1 reduced state (cob[I]alamin), forming methylcob(III)alamin that in turn transfers its methyl to homocysteine, ultimately producing methionine [22]. It is currently not known how the Cbl digresses from the cytosol and enters the mitochondria, but once there the protein MMAB (methylmalonic aciduria type B protein) is required for the generation of AdoCbl, which transfers it to the MUT with the help of MMAA (methylmalonic aciduria type A protein), related respectively with the *cblB* [23] and *cblA* [24] disorders. The mitochondrial MUT exploiting the radical nucleophile of AdoCbl finally catalyses the isomerisation of methylmalonyl-CoA to succinyl-CoA [10], [25]. A graphical summary of the cobalamin intracellular metabolism is reported in Fig. 4.

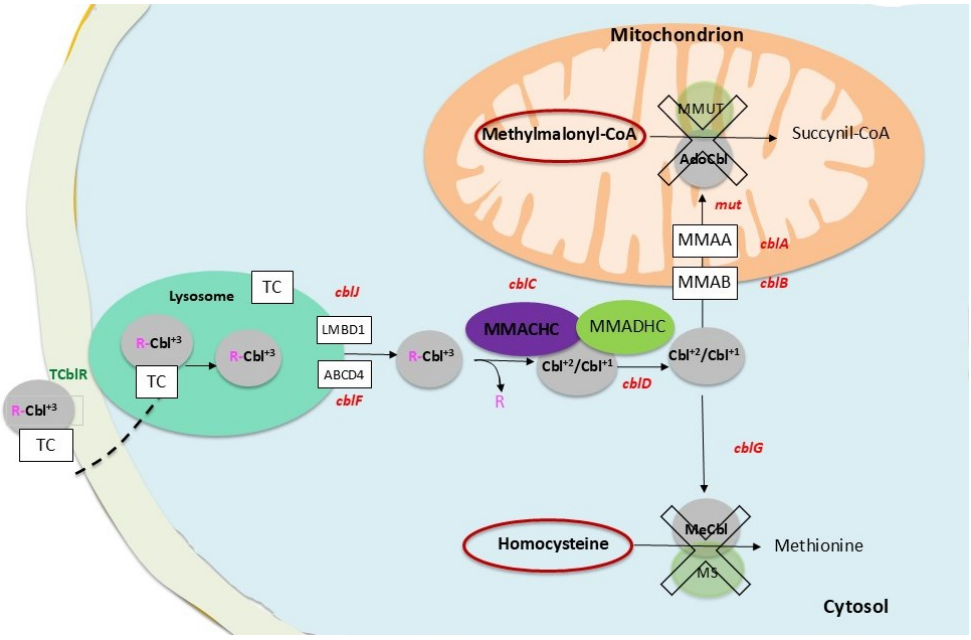

Figure 4. Graphical summary of cobalamin intracellular metabolism. Inherited disorders associated with the different enzymes are reported in red

1.2. *cblC* disease (OMIM #277400)

1.2.1. Causes and phenotypes of the disease

Mutations in the genes coding for the proteins involved into the vitamin B12 cellular trafficking lead to inborn errors of cellular cobalamin metabolism (IECM), classified as *cblA-J* and *mut* [26], [27]. Among these proteins, MMACHC plays a crucial role into vitamin B12 metabolic pathway, since it binds the Cbl in whatever form it was assimilated, and catalyzes the removal of the β-axial ligand, a mandatory step to ensure a proper partition into MeCbl and AdoCbl [28].

Since its enzymatic role is performed upstream the divergence between the cytosolic and mitochondrial pathway of the Cbl metabolism, pathological mutations in the MMACHC gene will lead to combined methylmalonic aciduria and homocystinuria, *cblC* type [29], with autosomal recessive inheritance. This rare genetic disorder, that is the most common among the IECM [30], with an estimated incidence rate of 1/200.000 births [31], is characterized by severe and heterogenic clinical manifestations, including neurocognitive, ocular and cardiovascular dysfunctions [32], [33].

Two distinct phenotypes have been recognized: the early-onset form (within the first year of life) is characterized by a systemic disease with neurological, and haematological abnormalities accompanied by ophthalmological deterioration, while patients with the late-onset form (after the fourth year of life) present progressive neurological symptoms and behavioral disturbances, and usually respond better to treatment [34]. The long-term outcome however is usually poor, leading to neurological impairment [35] and degenerative maculopathy [36].

At the cellular level, *cblC* mutant fibroblasts suffer from increased apoptosis likely owing to the overproduction of reactive oxygen species (ROS) [37]. Proteomic analysis of *cblC* fibroblasts revealed alteration of proteins related to cytoskeleton, the nervous system and cellular detoxification [38]. Low expression of vimentin in *cblC* fibroblasts could be responsible for the altered cellular morphology, while high levels of collagen, typical of homocystinuria, can be related to the cardiovascular dysfunctions because of the formation of collagen-rich atherosclerotic plaques. A severe downexpression of ubiquitin carboxy-terminal hydrolase L1, one of the most abundant neuronal proteins, that is not restored to normal levels upon therapeutic treatment, can explain the neurocognitive impairment and the poor improvement observed after treatment. Lastly, reduced expression of Glutathione S-transferases may compromise the detoxification of metabolites and explain the altered GSH/GSSH pool observed in patients, leading to severe oxidative stress. In summary, dysregulation in the proteome may also contribute to oxidative damage and aggravation of *cblC* manifestations [39].

The biomarkers of the *cblC* disease are elevated concentrations of total homocysteine and urinary/plasma methylmalonic acid, accompanied by normal or elevated vitamin B12 levels. Confirmation of the diagnosis is primarily done by molecular genetic analysis in dermal fibroblasts obtained from skin biopsy. Once the diagnosis is confirmed, therapy must be immediately initiated, since early treatment was found to improve long-term outcomes in *cblC* patients. In addition, regular follow-up is required to monitor and adapt the treatment and ensure early recognition of possible complications [40]. In light of the cruciality of early therapeutic

intervention, mandatory newborn screening for *cblC* was introduced in Italy and several other European countries in 2016.

1.2.2. Mutation spectrum

To date 115 pathogenic mutations have been identified, with genotypes and disease frequency differing significantly between populations. Among these, the most common mutation is c.271dupA (p.Arg91LysfsTer14), causing an arginine to lysine substitution at position 91 followed, 14 sites downstream, by a premature termination codon due to a frameshift and thus to a truncated protein. In homozygous states and in several heterozygous combinations it is associated with early onset disease and probably subjected to nonsense-mediated mRNA decay (NMD) [41]. The second most prevalent mutation is c.394C>T (p.Arg132Ter) in Caucasians [41] and c.609G>A (p.Trp203Ter) in Asians [42], both leading the to the formation of premature stop codons and thus to truncated proteins. Although these mutations often occur in heterozygosity with c.271dupA, they are related to late-onset disease and seems to be not involved in NMD. Whereas the disease more frequently results from frameshift and nonsense mutations, the majority of pathogenic mutations are missense [43], among which c.482G>A (p.Arg161Gln) is the most common. This mutation is always found in heterozygosity with a variety of other mutations, and is usually related to the late-onset form [42].

1.2.3. Current treatment

The only existing therapy for the *cblC* consists in betaine, folic acid, and L-carnitine administration, and in hydroxocobalamin (OHCbl) injections, which just mitigate the symptoms and cannot stop the progression of the disease [44]. Among the various forms of Cbl, parenteral administration of high-dose OHCbl, generally by painful intramuscular injections, was clinically proved as the most effective treatment among the various forms of Cbl to compensate for the deficiency. Oral betaine is recommended since it enables the hepatic MeCbl-independent remethylation of homocysteine to methionine via betaine homocysteine-methyltransferase [45]. Folate compounds as well as L-carnitine, are generally very well tolerated, yet clinical benefit remains unclear as case numbers are low and long-term data is missing [40].

1.2.4. Innovative therapies

The most common variant found in *cblC* patients, c.271dupA, is a frameshift mutation combined with the introduction of a premature termination codon (PTC), and generated a

protein, p.Arg91Lysfs*14, that is supposed to undergo nonsense-mediated RNA decay (NMD) [41]. For this mutation, gene therapy or enzyme replacement seems the only available perspective. However, different pharmacological approaches could be contemplated for the several missense or nonsense mutations not associated with the gene's reading frame change and not leading to NMD.

Wingert et al. proposed a therapy based on substrate replacement using synthetic thiolatocobalamins, that have been shown to undergo facilitated β-deligation and serve as antioxidant agents in vitro [46].

Concerning missense mutations, using small molecules to correct the protein misfolding defects and thus helping proteins to recover their activity, has revealed a successful therapeutic route for other rare conditions [47], [48], [49], [50]. The same approach is auspicious for the enzymes involved in metabolic disorders since exposure to pharmacological chaperones enhances many clinical mutants' stability and enzymatic activity [51]. In this respect, the affected stability profile shown by some MMACHC mutants [52], [53], [54] suggested that the folding correction could also have an impact on the *cblC* therapeutic approach.

Regarding *cblC* nonsense mutations, a therapeutic strategy could be represented by the use of translational readthrough-inducing drugs (TRIDs), which enhance ribosomal readthrough of premature termination codons (PTCs), partially restoring the production of a full-length protein [55]. This strategy has proven effective in reconstituting the biosynthesis of the full-length protein involved in another pathology of vitamin B12 metabolic pathway, *cblD*, in pathogenetic nonsense mutations harboring PTCs [56]. An example of TRIDs is Ataluren, capable of promoting the readthrough of TGA, TAG, and TAA codons, with the highest readthrough activity for the TGA codon and conditionally approved as therapy for some cases of Duchenne muscular dystrophy [57], [58]. Pibiri et al. recently designed and synthesized new oxadiazoles Ataluren-like compounds, which are able to induce readthrough of PTC in CFTR mutations involved in Cystic Fibrosis [59]. The most frequent nonsense mutation found in *cblC* patients, c.394C>T, associated to a significantly increased level of MMACHC transcript compared to c.271dupA (10), results in the production of a truncated MMACHC product, p.R132X. The stop codon associated with this mutation, UGA, and its position relative to the exon-exon junction supposed to elude NMD renders c.394C>T an ideal candidate to be corrected by readthrough activity. Other PTCs found in *cblC* variants (c.331C>T, c.609G>A, c. 666C>A) also have characteristics that make them suitable for readthrough activity. Since the readthrough strategy via TRIDs associates a different amino acid than the one present in the WT protein [58], [60],

if necessary, folding correctors for missense mutations can be used in combination with the TRIDs.

1.3. MMACHC protein

1.3.1. Structure

According to the crystal structure [61], human MMACHC is a 282 aminoacid protein (M.W. = 34 kDa) with an alpha/beta-scaffold that comprises two modules: N-terminal (a.a. 1–172) and C-terminal (a.a. 183-282), connected by a long unordered linker (a.a. 173-182). The N-terminal module contains a four stranded antiparallel beta-sheet flanked by α-helices and a short antiparallel two-stranded β-sheet. The C-terminal module is composed of four helices that cap the N-terminal core and a disordered tail, rich in proline. Three disordered protrusions (Pr1, Pr2, Pr3) were also found in the protein structure. Upon cobalamin binding, the main structural modifications consist in the movement of Pr2 toward Cbl, creating the floor of the pocket and the repositioning of the LIJ loop of the cap to form part of the Cbl-binding site. Cobalamins are found in the *base-off* configuration when bound to the MMACHC. In this configuration, the cobalamin tail resides in a hydrophobic crevice, which is formed between helix HF and the two-stranded antiparallel β-sheet, while the side chains of the corrin ring have polar interactions with the cavity surface, which is defined on the top by part of the cap module, on the bottom by the Pr2 and on the side by Pr3. The GSH binding site consists in an electro-positive, arginine rich pocket, where the residue R161 plays a major role in anchoring the cofactor to the protein by the interaction between the guanidinium group of arginine and the carboxamide group of the cysteine residue in GSH, assisted primarily by the help of residues R230 and R206 [62], [63]. MMACHC in complex with MeCbl and GSH is presented in Fig. 5; a QR code linking to a video showing the 3D structure is also provided. The putative binding site for the flavins (FMN/FAD) could reside between helix HE and the first β-sheet [61], but no crystal structure of the complex is currently available, and Froese et al. suggests that this binding mode would not guarantee an effective electron transfer [62].

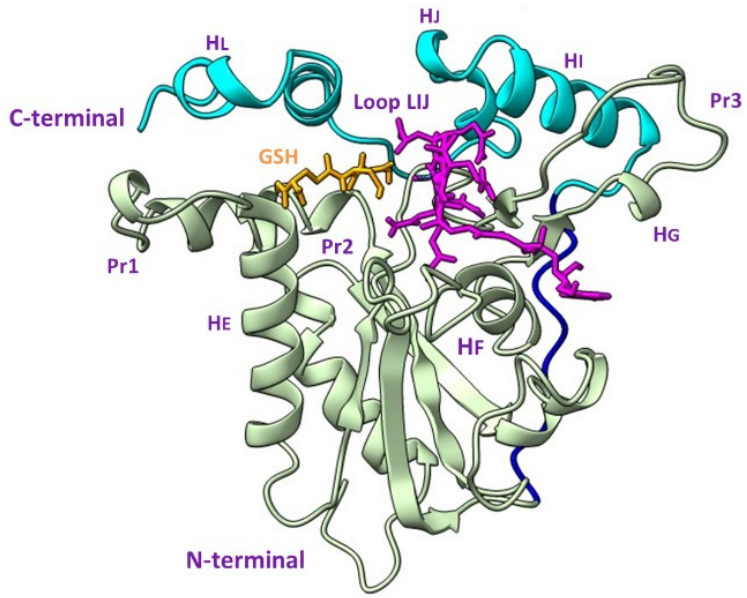

Figure 5. MMACHC in complex with MeCbl (magenta) and GSH (orange). The N-terminal module is shown in green, the unordered linker in blue and the C-terminal module in cyan; the QR code links to a video showing the 3D structure of the complex. Figure adapted using ChimeraX from 5UOS and 3SC0

1.3.2. Dimeric assembly

Initially believed to exist exclusively in a monomeric state [61], in 2012 Froese et al. found that MMACHC is able to homodimerize both *in vitro* and the crystal in the presence of AdoCbl [62]. Two ligand-binding monomers can assemble into a homodimer, which is largely mediated by protrusions Pr1 and Pr2 from both subunits. In particular, Pr2 from each subunit, crosses over, and interacts with the Ado moiety of AdoCbl in the opposing monomer, forming a cap for the upper axial ligand. The involvement of active site regions into the dimer formation, suggests a functional role, however the purpose of the dimerization process still remains elusive.

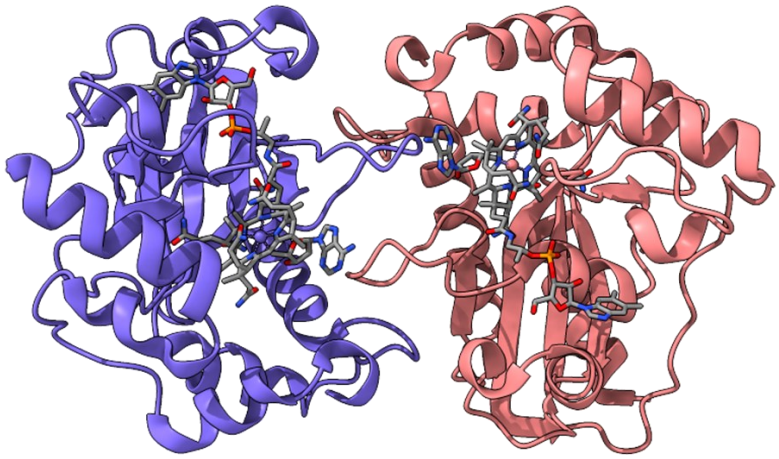

Figure 6. Dimer structure of two MMACHC–AdoCbl subunits showing the key mediating role of Pr2. Figure adapted using ChimeraX from 3SOM

1.3.3. Biochemical role

MMACHC protein is the downstream acceptor of the Cbl exiting the lysosome and the protein responsible for processing the upper-axial ligand of Cbls, in order to obtain an intermediate that will be further converted into the bioactive forms, i.e. MeCbl and AdoCbl.

The lysosome-to-cytosol transfer of Cbl is mediated by the interaction of the cytosolic MMACHC protein with the lysosomal transporters LMBD1 and ABCD4 [64]. Once bound to the Cbl, MMACHC catalyzes the removal of its upper-axial ligand, leading to the reduction of the central cobalt. Depending on the nature of the encountered cobalamin, this reaction consists in a dealkylation, using GSH as cofactor [65], or in a decyanation in the presence of flavin redox system [66], [67]. Both the reactions are favored by the binding of the cobalamins in the *base-off* configuration, that guarantees an easier scission of the Co-C bond [68]. The dealkylation consists in the nucleophilic attack of the Co-C bond by the thiolate anion of glutathione, giving as a product the S-alkylated variant of GSH and the so called *superreduced* cob(I)alamin, which spontaneously undergoes one-electron oxidation to form the more stable reduced cob(II)alamin. The reduced cob(II)alamin is instead the direct product of the cyanide reductive elimination in the presence of FMN/FAD and nicotinamide adenine dinucleotide phosphate (NADPH).

The enzymatic activity of MMACHC, capable of both reductive dealkylation and decyanation, makes it the first member of a novel subfamily of both the Glutathione S-transferases (GSTs) [69] and the Flavin reductases [61]. In particular, MMACHC lacks the active serine or tyrosine residue that induces the deprotonation of GSH typical of the GSTs and although its N-terminal core exhibits a fold characteristic of the flavin reductase, it shows poor structure alignment with other members of this family. Hence, MMACHC represents a novel structural solution for both the decyanation and dealkylation activities.

After the obtainment of the reduced cobalamin, this can form can be delivered to the end-user MS and MUT through the help of MMADHC protein, that is likely involved into the partition of the Cbl between the cytosolic and the mitochondrial route, although the mechanism is still unknown [19]. MMADHC can coordinate its Cys261 to cob(II)alamin bound to MMACHC, that rapidly oxidizes to thiolato-cob(III)alamin. This is the only known example of a heterodimer consisting in an interprotein coordination complex involving a rare Co-S bond [70].

The final delivery of Cbl to the cytosolic MS is probably favoured by a direct interaction with MMACHC [71], while it is currently not known how and when Cbl moves from the cytosol and enters the mitochondria [72]. A schematic representation of the reactions catalyzed by MMACHC protein is reported in Fig.7.

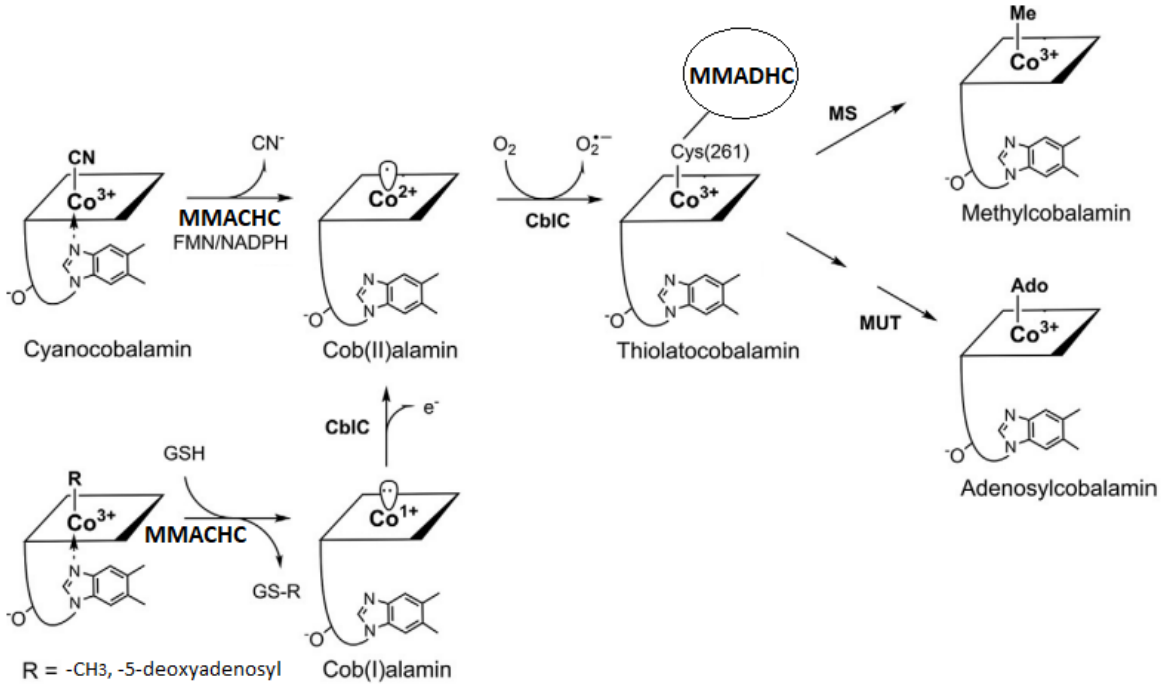

Figure 7. Biochemical reactions catalyzed by MMACHC. Figure adapted from *Esser et.al, iScience (2022)*

1.3.4. State of the art

Since the discovery of the *MMACHC* gene coding for the MMACHC protein, whose mutations are responsible for *cblC* disease in 2006 [16] two major research groups have focused their interest in uncovering the mechanisms underlying the function of the wild-type protein. After demonstrating its decyanase [66] and dealkylation activity of vitamin B12 [69], the first crystal structures in both apo and MeCbl-bound forms were obtained in 2011 by Koutmos et al [61], revealing the organization of the cobalamin binding pocket. In parallel, Froese et al. demonstrated the thermolability of the wild-type protein [52], and in 2012 obtained a crystal structure of the wild type revealing an homodimeric assembly when bound to AdoCbl and an arginine-rich region, that was addressed as the GSH binding pocket [62]. This latter supposition was confirmed five years later by the first crystal structure of MMACHC bound to GSH by Ruetz et al. [63], obtained by binding the protein to an anticobalamin (i.e. an inactive form of vitamin B12) thus allowing the co-crystallization of the cofactor. The research subsequently focused on the understanding of the interaction between MMACHC and the other proteins of the vitamin B12 metabolic pathway, leading to the discovery of the formation of a MMACHC-MMADHC heterodimer [19], [70], [73] and the subsequent interaction of the complex with the MS [71]. These findings proposed a new role of MMACHC, not only responsible for chemically processing the vitamin B12, but also for transporting it.

Regarding the biophysical and biochemical characterization of pathological mutants involved in *cblC* disease, Gherasim et al. demonstrated that mutations affecting the GSH-binding pocket

(R161Q and R161G) lead to a loss-of-function of MMACHC and induce an increased redox cycling that could explain the oxidative stress observed in the patients' cells [54]. Later they found synthetic cobalamins able to repair the enzymatic activity of these mutant *in vitro* [46]. To be thorough, we report that in 2013 Backe et al. found the novel mutation ΔGln131 that induces the deletion of one of the aminoacid involved in binding the cobalamin tail and suggested that this mutation induces a misfolding of the resulting protein and a reduced enzymatic activity [74], However, the biophysical data presented in this study have certain limitations. Last, in 2022 Passantino et al. characterized the R132X mutant, finding that while it retains secondary structure elements and remains compact in solution, its stability is affected by the mutation [53].

Overall, these findings have provided a solid framework for understanding MMACHC role and function in the vitamin B12 metabolic pathway. At the same time, studies on pathological variants have highlighted how mutations can compromise folding, stability, and enzymatic activity of the resulting proteins, thereby leading to the manifestations of *cblC* disease. Nevertheless, many aspects of the molecular mechanisms underlying MMACHC function, and the genotype–phenotype correlations of its variants, are still poorly resolved, thus requiring further investigation.

2. Aim of the thesis

A rare disease is defined by the European Union as a condition affecting fewer than 5 people per 10,000. Despite their rarity, these diseases pose a significant societal challenge, as effective treatments are often lacking due to limited investments. The *cblC* defect is a genetic disorder that, like many other rare diseases, is often overlooked by the pharmaceutical industry, so that the efforts of the scientific community in this framework are invaluable.

Given the key role of MMACHC in the complex vitamin B12 metabolic pathway, understanding the molecular mechanisms underlying *cblC* disease requires a detailed characterization of the wild-type protein and its pathogenic variants. In particular, although the crystal structure of the wild type has been resolved, many molecular features of *cblC* pathogenesis remains to be understood and the study of the precise impact of the pathological mutations is still lacking.

The present work aims to implement an experimental strategy, complemented by computational studies, to investigate the structure-function relationship of MMACHC-WT protein and the pathological MMACHC-R161Q mutant, resulting from the most frequent missense mutation found in *cblC* patients. We aim to characterize *in vitro* the impact of this missense mutation on the MMACHC molecular properties, such as structure, stability, binding to substrates and cofactors, oligomerization propensity and catalytic activity, in order to reveal previously unexplored aspects of MMACHC chemico-physical properties and provide a strong basis for further therapeutic development. The experimental workflow consisted in the production of the recombinant proteins from *E. coli* and their characterization by spectroscopical (Circular Dichroism, UV-Visible spectroscopy, fluorescence spectroscopy), calorimetric (Differential Scanning Calorimetry and Isothermal Titration Calorimetry) and separation (Blue-Native gel electrophoresis, size exclusion chromatography) techniques, assessing the effect of different cobalamin forms and glutathione. Our experimental findings were also supported by Molecular Dynamics simulations, that allowed a better understanding of the different behaviour of the two proteins and provided a molecular explanation of the misfolding of MMACHC-G147A, an insoluble pathological mutant protein. Moreover, we evaluated the effect of chemical chaperones on the functionality of the MMACHC-R161Q mutant, in order to suggest a therapeutic approach based on the stabilization of the protein structure. In this regard, we also

conducted preliminary studies on the effect of small molecules selected through *in silico* approaches, with potential therapeutic effect for missense mutations. Last, we generated a reporter system that will be used to assess the potential effect of TRIDs in model cells.

Our findings contribute to a better understanding of the molecular mechanisms underlying *cblC* pathogenesis and, at the same time, demonstrate how the combination of experimental and computational biophysical approaches can offer new insights on the study of this rare condition. Furthermore, since many rare diseases share common molecular mechanistic features driving the pathogenic events, the biophysics-based methodological toolbox presented here could also be valuable for investigating other rare diseases.

3. Methods

This chapter provides an overview of the biophysical techniques adopted to characterize wild-type MMACHC and its pathogenic variants, followed by the specific description of the experimental setup used. The approaches used for protein production and purification are described, along with the techniques applied to assess protein folding, stability, cofactor binding, dimerization propensity and effect of small molecules. Computational analyses complement the experimental data, offering additional insights into the molecular mechanisms underlying MMACHC dysfunction in *cblC* disease. Unless otherwise specified, each experiment was performed in triplicate.

3.1. Plasmids and site-directed mutagenesis

The generation of the plasmid coding for MMACHC-R161Q for the recombinant production of the protein in *E. coli* was generated from the plasmid coding for the WT by site-directed mutagenesis.

Polymerase Chain Reaction (PCR) is a technique used to amplify a specific DNA fragment *in vitro* [75]. Each amplification cycle consists of three steps:

1. **Denaturation** at high temperature that separates the two DNA strands of the template
2. **Annealing** of synthetic primers to complementary sequences on the template
3. **Extension** by a thermostable DNA polymerase (Taq Pol) that synthesizes new DNA strands.

By repeating these steps 25–40 times, the target DNA fragment is exponentially amplified.

In **site-directed mutagenesis** (schematic representation in Fig. 8), a modified version of PCR is used. Instead of standard primers, mutagenic complementary primers containing the desired base changes are employed. During thermal cycling, the DNA polymerase incorporates these mutations into newly synthesized plasmids. After digestion of the parental plasmid DNA with DpnI (an endonuclease specific for methylated DNA**)**, the resulting mixture is enriched in mutated plasmids, which are then transformed into competent *E. coli* [76].

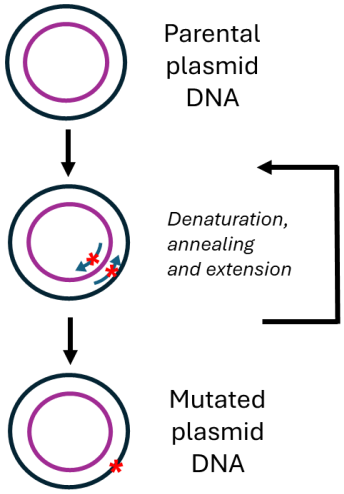

Figure 8. Schematic representation of site-directed mutagenesis

The plasmid pNIC28-Bsa4-MMACHC expressing the human MMACHC-WT as a TEV protease cleavable N-terminal His-tag protein was a gift from Nicola Burgess-Brown (Addgene plasmid #39096; the map of the plasmid is reported in Fig. 9). R161Q mutant sequence was generated by site-directed mutagenesis of the wild-type vector using QuikChange Lightning Site-Directed Mutagenesis Kit (Agilent Technologies, Inc.) and the primers GCTGGTTTGCCATCCA**A**GGGGTAGTGCTGCT and AGCAGCACTACCCC**T**TGGATGGCAAACCAGC, where the letters in bold represent the mutated nucleotides. The resulting plasmid pNIC28-Bsa4-MMACHC-R161Q leads to the expression of MMACHC-R161Q, a protein where the arginine residue in position 161 is substituted by a glutamine. The nucleotide sequence was confirmed by Sanger sequencing.

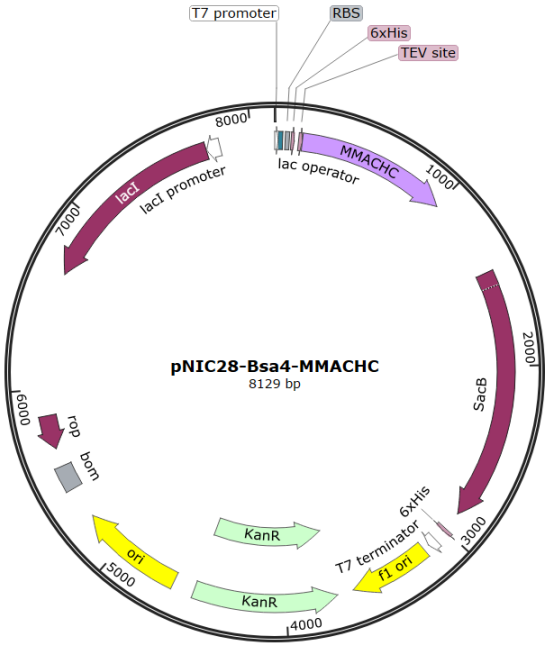

Figure 9. Map of pNIC28-Bsa4-MMACHC plasmid

3.2. Expression and purification of MMACHC-WT and MMACHC-R161Q

In order to perform the biophysical analyses presented in this thesis, we produced recombinant MMACHC-WT and MMACHC-R161Q proteins using *E. coli* BL21-Gold (DE3) as expression system. The proteins were purified from the soluble fraction of the bacterial lysate by affinity chromatography followed by a buffer exchange, and their purity was verified by SDS-PAGE.

Immobilized affinity chromatography (IMAC) is a specific separation technique that exploits the reversible interaction between a target molecule and a ligand immobilized on a solid matrix. The mixture containing the molecule of interest (i.e. the protein containing a polyhistidine tag, so called His-tagged protein) is passed through a column containing a matrix functionalized with bivalent metal ions (e.g., Ni^{2+}, Co^{2+}), that only the His-tagged protein binds due to its specific affinity. Unbound molecules are washed away, and the target molecule is subsequently eluted with a buffer containing imidazole, the competing ligand of histidine (Fig. 10) [77].

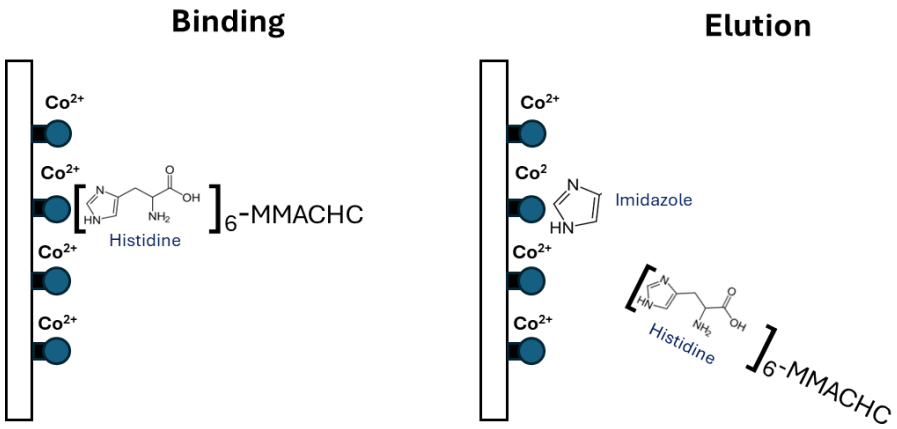

Figure 10. Schematic representation of the principle of IMAC

Gel electrophoresis is a technique that uses an electric field to drive the migration of charged molecules through a gel matrix. In **SDS-PAGE**, the gel is made of cross-linked acrylamide and bis-acrylamide, creating a porous structure that acts as a molecular sieve. By adjusting the ratio of acrylamide to bis-acrylamide, the pore size can be controlled, making the gel able to separate proteins within specific size ranges. Sodium dodecyl sulfate (SDS) is an anionic detergent that denatures proteins by disrupting non-covalent bonds, linearizing them, and conferring a uniform negative charge to the proteins, ensuring that the migration depends only by size, as the charge-to-mass ratio is constant. In addition, the samples are boiled to ensure denaturation and a reducing agent, such as β-mercaptoethanol or dithiothreitol, is added to disrupt disulfide bonds. Proteins are loaded into wells at the top of the gel, and an electric field is applied to

make them migrate towards the anode. The polyacrylamide gel consists of two parts: the stacking gel, which has a lower acrylamide concentration and a pH around 6.8, that concentrates the proteins into well-defined bands and the resolving gel, with a higher acrylamide concentration and a more basic pH (around 8.8), that resolves the proteins based on size. Smaller proteins pass more easily through the gel pores and move faster, while larger proteins migrate more slowly, resulting in separation. A molecular weight marker, composed of proteins with known sizes, is run alongside the samples. By comparing the migration distances of unknown proteins to these standards, their approximate molecular weights can be determined. After the course, proteins are visualized using a stainer [78].

Expression and purification of recombinant MMACHC-WT and MMACHC-R161Q proteins were carried out following the procedure previously described, with minor modifications [53].

Briefly, *E. coli* BL21-Gold (DE3) harboring pNIC28-Bsa4-MMACHC was grown at 37 °C in Terrific Broth (TB) medium supplemented with kanamycin (30 μg/mL). When OD_{600} of the culture reached 2, expression was induced by addition of 0.1 mM isopropyl 1-thio-β-d-galactopyranoside (IPTG) overnight at 18 °C. Upon harvesting, cells were suspended in pre-chilled lysis buffer 20 mM PB (10 mM Na_2HPO_4, 10 mM NaH_2PO_4) pH 7.4, 0.5 M NaCl, supplemented with 25 U/mL Benzonase ® (Merk-Millipore), 5 mM $MgCl_2$, 0.4 mg/mL lysozyme, one tablet of cOmplete™ EDTA-free protease inhibitor mixture (Roche), 5 % (*v*/v) glycerol and 10 mM imidazole. The cells were disrupted on ice by sonication (Bandelin HD 2070) and the supernatant was collected after centrifugation at 20.000 *xg*, 4 °C for 30 min, filtered using 0.2 μm filter, and loaded onto a 5 mL HiTrap TALON crude (Cytiva) column equilibrated in the same buffer of the protein sample. The His-tagged protein was eluted, on a FPLC ÄKTA Primeplus GE Healthcare, with a linear gradient from 10 to 300 mM of imidazole in 10 CV at room temperature, using prechilled elution buffers. A buffer exchange was then obtained using a HiPrep Desalting 26/10 column (Cytiva).

Purity of both proteins was verified by SDS-PAGE using NZYtech BlueSafe as stainer. Proteins were stored in 20 mM PB, pH 7.4, 0.3 M NaCl, 5 % (*v*/v) glycerol, at −80 °C.

3.3. Circular dichroism (CD)

Circular dichroism spectroscopy is a widely used technique to investigate the secondary structure and the folding of proteins in solution [80].

Plane polarised light can be viewed as being made up of two circularly polarised components (Fig. 11) of equal magnitude, one rotating counter-clockwise (left handed, L) and the other clockwise (right handed, R).

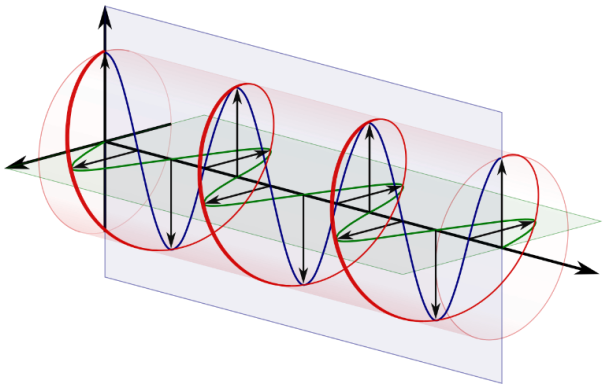

Figure 11. Illustration of circularly polarized light showing the helical rotation of the electric field vector along the propagation axis.

Circular dichroism (CD) refers to the differential absorption of these two components. Over corresponding wavelengths, a circular dichroism signal can, therefore, be positive or negative, depending on whether L light is absorbed to a greater extent than R light (CD signal positive) or to a lesser extent (CD signal negative).

The linearly polarised light becomes elliptically polarised when the magnitudes of the two components are differently absorbed:

$$CD = \Delta A = A_L - A_R$$

This is what happens, for example, when the two circular components encounter a chiral molecule, which interacts differently with left- and right-circularly polarized light.

The ellipse of the resulting elliptically polarised light can be described by the lengths of its axes (Fig. 12):

- The length of the major axis is the sum of the magnitudes of the electric field vectors of the R and L circularly polarized light, $E_R + E_L$
- The length of the minor axis is the difference between the magnitudes of the electric field vectors of the R and L circularly polarized light, E_R - E_L.

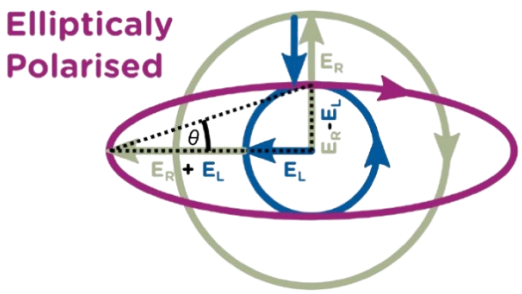

Figure 12. Components of the elliptically polarized light (purple). Figure adapted from Applied Photophysics

The degree of ellipticity is then defined as the tangent of the angle θ, whose tangent is equal to the ratio of the minor to major elliptical axis:

$$\tan\theta = (E_R - E_L)/(E_R + E_L) \approx \theta$$

As the difference in absorbances of L and R circularly polarized light is typically very small, tan θ can be approximated as θ (in radians). From the logarithmic definition of absorbance, the following relationship is obtained:

$$\theta(degrees) \approx \Delta A \times 32.982$$

Due to the small magnitude of CD signals in most measurements, θ is often expressed in millidegrees.

In the case of a protein solution, the ellipticity value can be normalized for the number of aminoacids of the protein, giving the mean residue ellipticity (MRE):

$$MRE = \frac{\frac{MW}{N-1} \times \theta}{10 \times l \times C}$$

where MW is the molecular weight of the protein, N the number of aminoacids, l the pathlength in cm and C the concentration in mg/mL. This normalization makes the MRE independent of both the path length and the protein concentration, allowing direct comparison between spectra of different proteins or experimental conditions

In the far-UV region (240-180 nm), the chromophore that dominates the spectral signal of proteins is the peptide bond (Fig. 13); the chiral center is the α-carbon atom in the protein backbone (i.e. the continuous chain of atoms that forms the structural framework of a polypeptide, consisting of the repeating sequence of amide nitrogen, alpha carbon, and carbonyl carbon N–Cα–C′ from each amino acid residue). There is a weak but broad n → π* transition at ~ 210-230 nm and a more intense π → π* transition at ~ 190 nm.

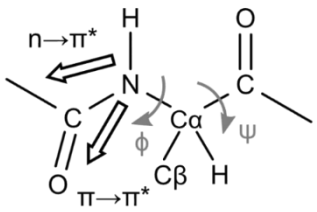

Figure 13. Peptide bond

Depending on the orientation of the peptide bonds within the array, the optical transitions of the amide bond can be split into multiple components. The wavelengths of these transitions may shift to higher or lower values, and their intensities can either increase or decrease. As a consequence, the far-UV CD spectrum of a protein provides a fingerprint of its secondary

structure. The secondary structure of a protein is formally defined as the pattern of hydrogen bonds between the amino hydrogen and carboxyl oxygen atoms in the backbone. The two most common types of secondary structure are α-helices and β-sheets [79]. In an α-helix, hydrogen bonds between the carbonyl oxygen of residue *i* and the amide hydrogen of residue *i+4* form a right-handed helical structure, while a β-sheet is formed by the side by side alignment of two or more β-strands stabilized by hydrogen bonds between backbone carbonyl and amide groups. These secondary structures provide rigidity to the protein molecule, that can be counterbalanced by the flexibility induced by random coil regions. The different types of regular secondary structure found in proteins give indeed rise to characteristic CD spectra (Fig. 14) [80]:

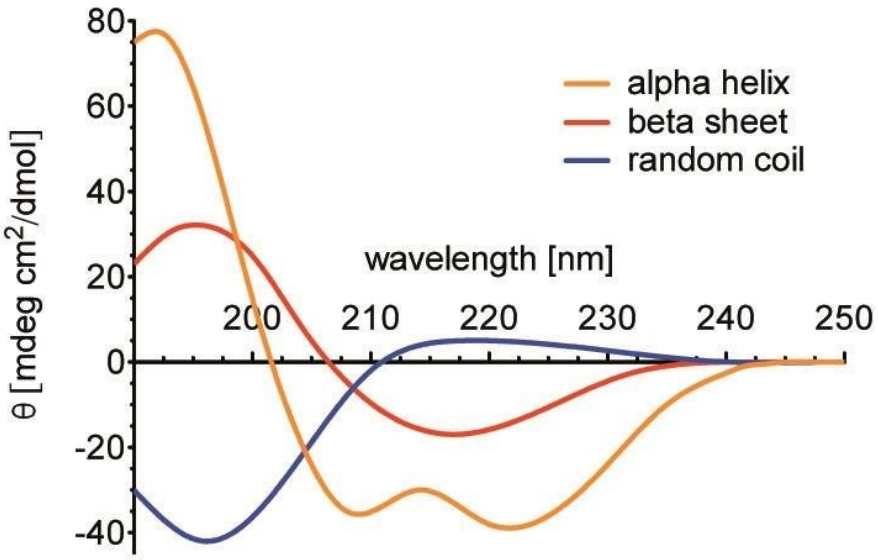

Figure 14. Standard CD spectra of polypeptides/proteins with representative secondary structures. Figure adapted from *Greenfield, Nat Protoc (2006)*

The α-helices spectrum is characterized by two typical minima near 222 nm and 208 nm, and a positive band near 192 nm. β-sheets spectrum presents a negative band near 218 nm, and positive peak around 195 nm. Random coils spectrum shows a strong negative band with a broad peak around 200-205 nm. An estimation of the secondary structure composition of a protein can be provided by some algorithms.

The CD spectrum in the region 260– 320 nm arise from the aromatic amino acids. The actual shape and magnitude of the near-UV CD spectrum of a protein will depend on the number of each type of aromatic amino acid present, the nature of their environment (H-bonding, polar groups and polarisability) and their spatial disposition in the protein. Tryptophan (Trp) shows a peak close to 290 nm with fine structure between 290 and 305 nm, tyrosine (Tyr) a peak between 275 and 282 nm, with a shoulder at longer wavelengths often obscured by bands due

to Trp and Phenylalanine (Phe) shows weaker but sharper bands with fine structure between 255 and 270 nm. The near-UV CD spectrum gives information on the tertiary structure of the protein [80]. The tertiary structure of a protein is the three-dimensional spatial conformation that it adopts, that is determined by the interactions between the residues and interactions with the solvent. The specific arrangement of these interactions creates a unique conformation that is critical for the protein function [81].

Proteins indeed virtually regulate every biological process. Their biological activity depends on their intrinsic dynamics and ability to adopt and maintain a defined three-dimensional conformation. Protein folding is the physical process by which a protein, after its synthesis by a ribosome as a linear chain of amino acids, changes from an unstable random coil into a more ordered three-dimensional structure. This process is governed by the interplay of numerous non-covalent interactions, including hydrogen bonds, hydrophobic effects, electrostatic forces, and van der Waals interactions, which collectively drive the polypeptide chain toward its native folded state, a thermodynamically favorable conformation corresponding to the global minimum of the free energy of unfolding ($\Delta G = \Delta H - T\Delta S$). Conformational stability reflects the balance between enthalpic contributions (ΔH) that favor the stabilizing interactions of the folded state and entropic factors ($-T\Delta S$) that promote disorder of the unfolded state, and it is influenced by both intrinsic properties (the aminoacidic composition) and extrinsic conditions (including temperature, pH, ionic strength, and ligand binding). Temperature plays a key role in modulating this equilibrium: as temperature increases, the entropic contribution becomes more significant, gradually destabilizing the folded state until leading to the unfolded state. The thermal unfolding process of small proteins is typically cooperative, following a two-state model involving one transition in which the native folded structure converts to a fully unfolded state without stable intermediates. However, for most proteins, additional intermediate conformations (less folded than the native state but more folded than the denatured state) are populated during the thermal denaturation process. For proteins displaying equilibrium intermediates, the global equilibrium between the native and the unfolded states can be divided into partial equilibria between the different species, each one governed by an equilibrium constant and, therefore, by a free energy difference. The study of temperature-dependent conformational changes represents a powerful approach to quantify protein stability and to assess how mutations and ligand binding affect the energetic landscape of folding [82].

CD spectroscopic measurements for this research were performed by using a Chirascan v100 spectrometer (Applied Photophysics) equipped with a temperature control unit. This allowed

the study of secondary structure changes in the far-UV region at increasing temperature values, in order to characterize the conformational stability properties of the proteins.

3.3.1. Far-UV measurements

A quartz cell with a path length of 1 mm was used for recording at 20 °C far-UV (190–250 nm) spectra of the MMACHC-WT (10 μM) and MMACHC-R161Q (10 μM) protein in the absence and in the presence of AdoCbl, MeCbl, CNCbl and OHCbl (Sigma Aldrich) in a molar Cbl to protein of 2:1. The concentration of the cobalamins was calculated considering the extinction molar coefficient according to [83]. Spectra were acquired with a 5 nm/min scan rate, band width 3 nm, response 32 s and data pitch 0.5 nm.

The analysis of thermal denaturation was monitored by measuring the ellipticity values at 222 nm upon gradually heating from 15 °C to 90 °C for both the MMACHC-WT (10 μM) and MMACHC-R161Q (10 μM), in the presence and in the absence of cobalamins (20 μM) or with the addition of betaine (0.5 M), with a heating rate of 0.5 °C/min, path length 1 mm, band width 3 nm, data pitch 1 min, response 16 s.

MMACHC-R161Q ellipticities at 222 nm were fitted according to the single-transition unfolding model. Under equilibrium F $\rightleftarrows$ U, at any temperature T the conformational equilibrium constant K is:

$$K(T) = \frac{X_F}{X_U} \tag{1}$$

where X_F and X_U are the molar fractions of folded and unfolded molecules, respectively and the free energy of unfolding ΔG is:

$$\Delta G(T) = -RT \ln K(T) \tag{2}$$

The temperature dependence of the Gibbs energy is given by:

$$\begin{gathered} \Delta G(T) = \Delta H(T_m)\left(1 - \frac{T}{T_m}\right) + \Delta C_P\left(T - T_m - T\, ln\, \frac{T}{T_m}\right) \\ K(T) = exp\left(-\frac{\Delta G(T)}{RT}\right) \\ X_F(T) = \frac{1}{1+K(T)}, X_U(T) = \frac{K(T)}{1+K(T)} \end{gathered} \tag{3}$$

where T_m is the temperature corresponding to denaturation midpoint (at which X_F=X_U).

The observed spectroscopic signal (S) is given by:

$$S(T) = S_F(T)X_F(T) + S_U(T)X_U(T) \tag{4}$$

where S_F and S_U correspond, respectively, to the signal arising from a protein solution of the same concentration that would contain only folded or only unfolded molecules [82].

MMACHC-WT ellipticities at 222 nm were analyzed using the two-transition unfolding model, assuming a single intermediate state (I). The corresponding equations can be derived similarly to those for the single-transition by combining equations equivalent to Eqs. (1)–(3), considering that there are three coexisting species in equilibrium (F ⇄ I ⇄ U) and two conformational equilibrium constants K_1 and K_2 governing each transition (F ⇄ I and I ⇄ U):

$$\Delta G_i(T) = \Delta H_{mi}\left(1 - \frac{T}{T_{m,i}}\right) + \Delta C_{P,i}\left(T - T_{m,i} - T\ ln\ \frac{T}{T_{m,i}}\right)$$

$$K_i(T) = exp\left(-\frac{\Delta G_i(T)}{RT}\right) \quad (5)$$

$$X_F(T) = \frac{1}{1+K_1(T)+K_1(T)K_2(T)}, X_I(T) = \frac{K_1(T)}{1+K_1(T)+K_1(T)K_2(T)}, X_U(T) = \frac{K_1(T)K_2(T)}{1+K_1(T)+K_1(T)K_2(T)}$$

and the observed spectroscopic signal (S) is given by:

$$S(T) = S_F(T)X_F(T) + S_I(T)X_I(T) + S_U(T)X_U(T) \quad (6)$$

where S_F, S_I, and S_U correspond, respectively, to the intrinsic signals for the folded molecules, partially folded molecules (intermediate state), and unfolded molecules.

3.3.2. Near-UV measurements

A quartz cell with a path length of 1 cm was used for recording at 20 °C near-UV (250-350 nm) spectra of the MMACHC-WT (14 μM) and MMACHC-R161Q (14 μM) protein. Spectra were acquired with a 20 nm/min scan rate, band width 1 nm, response 4 s and data pitch 0.1 nm.

3.4. Intrinsic fluorescence

Fluorescence is a physical process in which a molecule absorbs light of a specific wavelength and subsequently emits light at a longer wavelength. Upon absorption of a photon, an electron of the fluorophore is promoted from the ground state to an excited electronic state. The excited molecule rapidly undergoes vibrational relaxation, dissipating part of the absorbed energy as heat. The electron then returns to the ground state by emitting a photon, a process that typically occurs within nanoseconds. Because of the prior energy loss, the emitted photon has lower energy and therefore a longer wavelength than the absorbed one (Fig. 15).

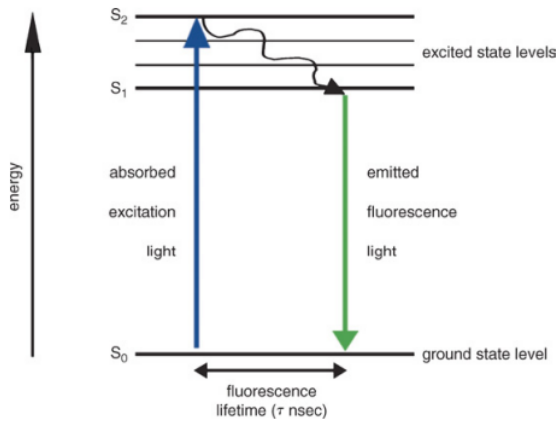

Figure 15. Jablonski diagram displaying the energy states of a molecule. Figure extracted from *Lleres et al., Curr Protoc Cytom (2007)*

A fluorescence emission spectrum represents the intensity of the emitted light as a function of wavelength, following excitation of the sample at a chosen excitation wavelength. The position of the emission band is commonly expressed as the maximum emission wavelength.

Proteins exhibit intrinsic fluorescence, which derives from its fluorophores, the aromatic amino acids: tryptophan, tyrosine, and phenylalanine. These residues are generally located in the hydrophobic core of the folded protein, and their emission properties are highly sensitive to the local environment. Most of the intrinsic fluorescence emissions of a folded protein are due to excitation of tryptophan residues, whose emission spectrum is strongly affected by the polarity of the surrounding environment and the proximity of other residues, making it a probe of protein folding, conformational changes, and interactions [84].

Thus, the fluorescent properties of aromatic residues can provide insights into the tertiary structure and dynamics of proteins.

Fluorescence experiments were performed by using a JASCO FP6500 spectrofluorimeter (JASCO Corporation, Tokyo, Japan) at T=20 °C. Emission spectra were registered after excitation at 295 nm, 275 nm and 260 nm (excitation slit width = 3 nm, emission slit width = 3 nm, response 2 s, scanning rate 100 nm/min) of a sample containing 0.1 mg/ml (3 µM) MMACHC-WT or MMACHC R161Q using a quartz cell with a path length of 1 cm.

3.5. Differential scanning calorimetry (DSC)

Differential Scanning Calorimetry (DSC) is the gold standard technique to study thermally induced transitions in proteins. DSC measures the heat capacity of a solution of the molecule under study as a function of temperature in a differential mode [85]. Calorimeters are equipped with two twin cells: the solution containing the protein is placed in the sample cell and an equal volume of buffer in the reference cell (Fig. 16). The system is heated at a constant rate and the

instrument continuously monitors temperature differences. When the protein undergoes thermal denaturation, that is always an endothermic process, the heat capacities of the solution in the sample cell and the buffer in the reference cell will differ, hence a certain amount of electrical power is required to zero the temperature difference between the two cells. The power difference, divided by the scanning rate, is a direct measure of the heat capacity difference between the solution and the buffer. This generates the typical endothermic peak in the DSC thermogram.

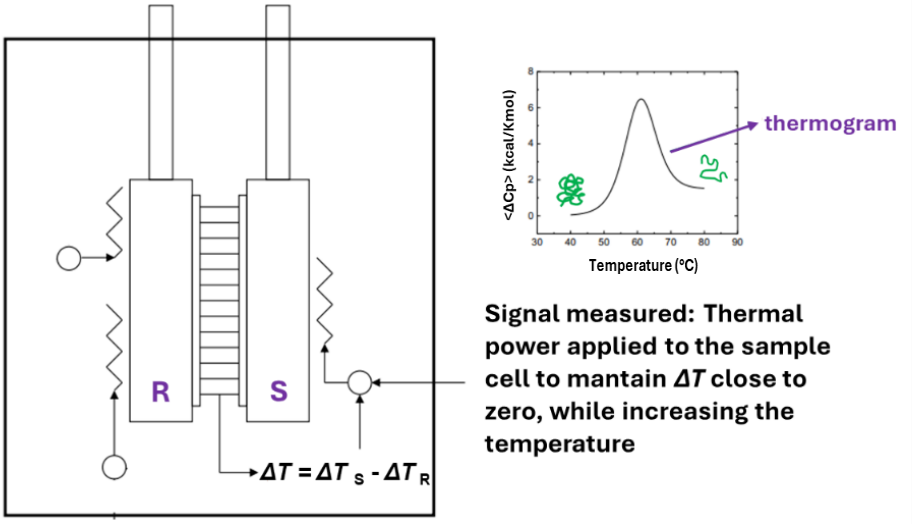

Figure 16. Schematic representation of a calorimeter and a thermogram from DSC

The first approach in DSC usually consists in model-free data analysis for discriminating between different possibilities: single transition unfolding, non-single unfolding, and oligomer unfolding of the protein. In the thermogram it is possible to estimate the unfolding enthalpy (ΔH_{cal}) by the area under the peak, the unfolding temperature (Tm) as the maximum of the curve and the maximal unfolding heat capacity (CP_{max}) as its height. From these parameters it is possible to calculate the van't Hoff enthalpy (ΔH_{vH}):

$$\Delta H_{vH} = \frac{(4RT_m^2 CP_{max})}{\Delta H_{cal}} \quad (7)$$

From the ratio $\Delta H_{vH}/\Delta H_{cal}$ three different possibilities may arise:

- ΔHvH/ΔHcal = 1, the thermogram would reflect a single transition and the protein unfolds according to a two-state model
- ΔHvH/ΔHcal < 1, the thermogram would reflect at least two transitions and the protein unfolds according to a non-two model
- ΔHvH/ΔHcal > 1, the thermogram would reflect an unfolding transition coupled to subunit dissociation

The thermal stability of apo MMACHC-WT (17 µM) and apo MMACHC-R161Q (17 µM) was assessed by differential scanning calorimetry in a MicroCal VP-Capillary DSC (MicroCal, Malvern-Panalytical). The partial molar heat capacity at constant pressure of the protein solution was measured as a function of the temperature at a scanning rate of 1 °C/min.

Several buffer-buffer scans were performed to ensure proper instrument and sample equilibration. After instrumental buffer baseline subtraction and concentration normalization, a baseline calculated from the progress of the unfolding process was subtracted to obtain the excess molar heat capacity of the protein.

The thermograms obtained for both MMACHC-WT and MMACHC-R161Q were analyzed applying a two-transition unfolding model using Origin7 package implemented in Prof. Adrian Velazquez-Campoy laboratory.

From the estimation of the van't Hoff enthalpy, both the proteins resulted in a non-single transition unfolding.

In the case of n independent transitions, each one characterized by the three unfolding parameters (unfolding temperature T_m, unfolding enthalpy $\Delta H(T_m)$, and unfolding heat capacity ΔC_P), the excess average heat capacity is given by:

$$\langle \Delta C_P \rangle = \sum_{i=1}^{n} \Delta C_{P,i}(T) = \sum_{i=1}^{n} \frac{K_i(T)}{\left(1+K_i(T)\right)^2} \frac{\Delta H_i(T)^2}{RT^2} \quad (8)$$

where the parameters are defined as:

$$\begin{aligned} K_i(T) &= exp\left(-\frac{\Delta G_i(T)}{RT}\right) \\ \Delta H_i(T) &= \Delta H_{mi} + \Delta C_{P,i}\left(T - T_{m,i}\right) \end{aligned} \quad (9)$$

The partition function for the model with two independent transitions (n = 2) is written as a product of two elemental sub-partition functions:

$$Z(T) = \left(1 + K_1(T)\right)\left(1 + K_2(T)\right) \quad (10)$$

with each factor representing a certain region or domain folding independently within the protein molecule, and it can be considered as a global partition function:

$$Z(T) = 1 + K_1(T) + K_2(T) + K_1(T)K_2(T) \quad (11)$$

corresponding to a conformational landscape with four conformational states: folded state, first intermediate state, second intermediate state, and unfolded state. From *Z(T)* the population of each state as a function of temperature can be calculated as follows:

$$\begin{aligned} P_F(T) &= \frac{1}{Z(T)} \\ P_{I1}(T) &= \frac{K_1(T)}{Z(T)} \\ P_{I2}(T) &= \frac{K_2(T)}{Z(T)} \\ P_U(T) &= \frac{K_1(T)K_2(T)}{Z(T)} \end{aligned} \quad (12)$$

3.6. Isothermal titration calorimetry (ITC)

Isothermal Titration Calorimetry (ITC) is a highly sensitive technique used to directly measure the thermodynamics of molecular interactions in solution, such as protein–ligand, protein–protein, or protein–nucleic acid binding. The principle relies on detecting the heat released or absorbed when two molecules interact [86].

The instrument consists of two identical cells: a reference cell filled with buffer and a sample cell containing one interaction partner, usually a macromolecule (Fig. 17). The other binding partner is titrated into the sample cell through a microsyringe in a stepwise manner. Each injection of the syringe solution triggers the binding reaction and a certain amount of complex is formed, accompanied by the release (exothermic reaction) or the absorption (endothermic reaction) of heat, that causes a difference in temperature between the two cells. Then, the feedback system either lowers or raises the thermal power applied to compensate such temperature unbalance. After each injection, the system reaches equilibrium and the temperature balance is restored. Therefore, the recorded signal shows a series of a peaks (thermogram). The integration of the area under the peak provides the amount of heat associated with the injection. By integrating the heat signal from each injection, a binding isotherm is obtained, which can be fitted to a thermodynamic model. This yields quantitative parameters such as binding constant (Ka) and enthalpy change (ΔH), from which entropy change (ΔS) and Gibbs free energy (ΔG) can be obtained.

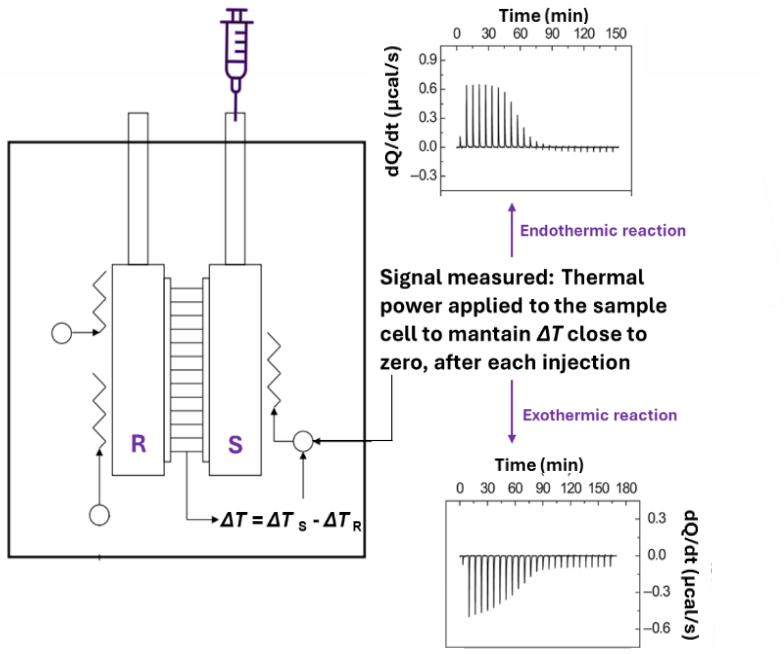

Figure 17. Schematic representation of a calorimeter and thermograms from ITC

The interaction between MMACHC-WT or MMACHC-R161Q and their ligands was assessed by isothermal titration calorimetry using a high precision Auto-iTC200 calorimeter (MicroCal, Malvern-Panalytical). Protein and ligands were separately dissolved in 20 mM PB, pH 7.4, 300 mM NaCl, 5% v/v glycerol. Compounds were titrated into protein solution by performing 19 injections of 2 µL each, and mixed using a stirring speed of 750 rpm, maintaining a spacing between injections of 150 s, and applying a reference power of 10 µcal/s.

3.6.1. Titration of AdoCbl

200 µM AdoCbl were titrated into a solution of 10 µM MMACHC-WT or MMACHC-R161Q. The experiments were performed at 25 °C.

3.6.2. Titration of MeCbl

200 µM MeCbl was titrated into a solution containing 10 µM MMACHC-WT or 15 µM MMACHC-R161Q. The experiments were performed at 25 °C.

3.6.3. Titration of CNCbl

400 µM CNCbl was titrated into a solution of 40 µM MMACHC-WT, while 560 µM CNCbl was titrated into a solution containing 56 µM MMACHC-R161Q.

3.6.4. Titration of GSH

500 µM of GSH were titrated into a solution of 10 µM MMACHC-WT or MMACHC-R161Q in the absence and in the presence of 20 µM AdoCbl. The experiments were performed at 25 °C and at 15 °C.

3.6.5. Titration of small molecules

200 µM of molecules M3, M6 and rutin diluted in sodium phosphate 20 mM, pH 7.4, NaCl 300 mM, glycerol 5% w/V from stock solutions in DMSO were titrated into a solution of 10 µM MMACHC-WT or MMACHC-R161Q mutant, supplemented with the corresponding amount of DMSO to ensure the same buffer composition between the cell and the syringe. The experiments were performed at 25 °C.

A model with a single ligand binding site was employed for data analysis. Briefly, the concentration of ligand and protein inside the calorimetric cell after each injection j are calculated as follows:

$$[L]_{T,j} = [L]_{syr}\left(1 - \prod_{k=1}^{j}\left(1 - \frac{v_k}{V_0}\right)\right) [P]_{T,j} = [P]_{cell}\prod_{k=1}^{j}\left(1 - \frac{v_k}{V_0}\right) \quad (13)$$

where $[L]_{syr}$ is the concentration of ligand in the syringe, $[P]_{cell}$ is the initial concentration of protein in the cell, v_k is the volume of each injection, V_0 is the cell volume, and j is the injection number. Normally, a factor n multiplying $[P]_{cell}$ is included in Equation 9 to account for a

fraction of non-binding-competent protein in the calorimetric cell. The binding isotherm (ligand-normalized injection heats as a function of the molar ratio) was built by integrating the injection heat effects recorded in the thermogram (thermal power as a function of time) and the theoretical heat exchanged for the jth injection was calculated as follows:

$$Q_j = \frac{1}{v_j[L]_{syr}} V_0 \Delta H \left([PL]_j - [PL]_{j-1} \left(1 - \frac{v_j}{V_0}\right)\right) + Q_d \quad (14)$$

where $[PL]_j$ is the concentration of complex formed after injection *j* and Q_d is the background injection heat (usually called "dilution heat", but it includes many other unspecific phenomena such as mechanical mixing and buffer neutralization). The concentration of complex after each injection was calculated using the following expression:

$$[PL] = \frac{1+K_a[P]_T+K_a[L]_T-\sqrt{(1+K_a[P]_T+K_a[L]_T)^2-4K_a^2[P]_T[L]_T}}{2K_a} \quad (15)$$

The equilibrium association constant, K_a, the binding enthalpy, ΔH, and the binding stoichiometry, n, were estimated through non-linear least squares regression analysis of the data in Origin 7.0 (OriginLab) [87]. From K_a, we also derived $\Delta G = -RT \ln K_a$ and $-T\Delta S = \Delta G - \Delta H$

3.7. Molecular dynamics (MD)

Molecular dynamics (MD) is a computational technique that simulates the time-dependent behavior of molecular systems at the atomic level. In classical MD, atoms are treated as particles whose motions are governed by Newton's laws. Molecular interactions are described by a force field, which approximates the potential energy of the system through bonded (bonds, angles, dihedrals) and non-bonded (electrostatic and van der Waals) terms. By integrating the equations of motion, MD provides trajectories that describe how the positions and velocities of atoms evolve over time. Simulations are typically performed within statistical ensembles (e.g., NVT, NPT) and under periodic boundary conditions, replicating the box in all directions, to approximate bulk behavior. A flowchart describing the steps of a typical MD simulation are reported in Fig. 18. This approach allows the exploration of conformational flexibility, stability, and interactions of the systems under near-physiological conditions, complementing the experimental data [88].

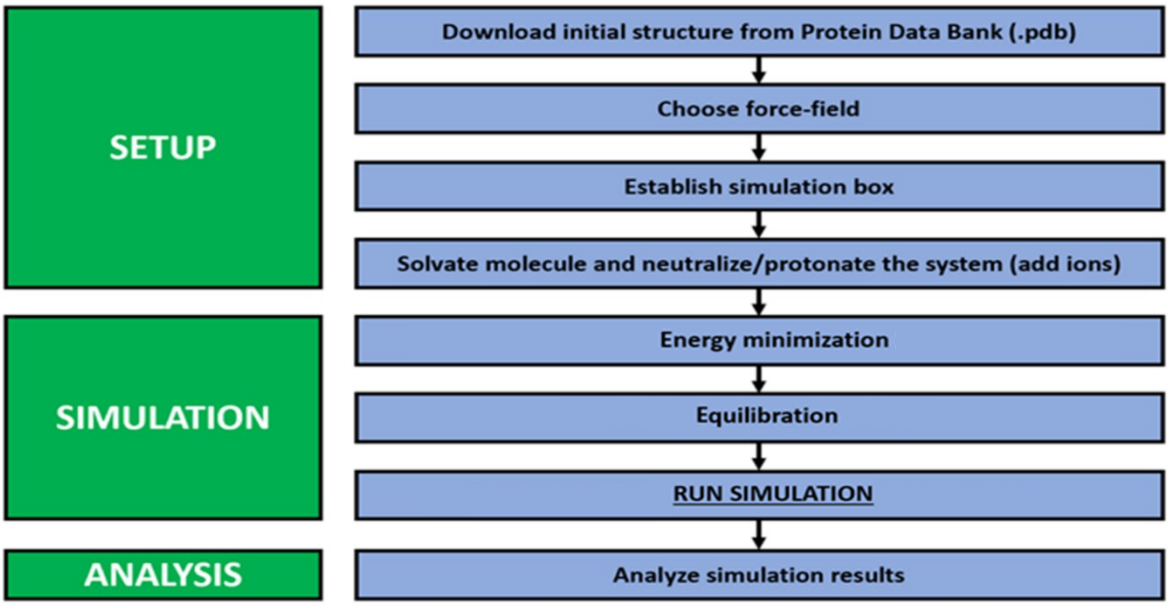

Figure 18. Flowchart of classical molecular docking. Figure adapted from *Smith et al., Processes (2022)*

3.7.1 Simulations of the complexes

The coordinates of the wild type MMACHC, in complex with GSH, were extracted from the pdb file 5UOS [63]. MeCbl coordinates were extracted from the pdb file 3SC0 [61]. Charmm-36 force field was used [89] and integrated with a set of charmm-compatible parameters to include MeCbl, published by Pavlova et al. [90]. The latter was modified to obtain the parameters for MeCbl(III) in the *base-off* conformation. Briefly, The DMB tail topology was extracted from "RESI CO1" (see S.I. of [90]), while the rest of the molecule was obtained from "RESI CO2", replacing CO6 with CO5 atom type. The methyl patch was applied manually, deleting the N of CN group, reassigning the partial charges and adding the hydrogen atoms of the methyl; the excess of charge was assigned to the Co atom (from 0.382 to 0.674), in order to obtain null total charge on MeCbl. Parameters for GSH were obtained using Ligand Reader & Modeler tool from CHARMM-GUI [91], [92]. The protein was solvated using water molecules such that there is minimum distance of 1.0 nm between the simulation box and the closest protein atom. Sodium and chloride ions were added to ensure charge neutrality. An adequate number of Na and Cl ions were added to maintain neutrality and to reach a concentration of 150mM of NaCl. The simulations were performed using GROMACS 2023.1 [93] using periodic boundary conditions.

Firstly, the system was minimized using the steepest descent algorithm**.** Position restraints were applied to solutes' heavy atoms, with force constants of 400 $kJ \cdot mol^{-1} \cdot nm^{-2}$ for backbone atoms

and 40 kJ·mol^{-1}·nm^{-2} for side chains. Minimization was performed until the maximum force converged below 1000 kJ·mol^{-1}·nm^{-1}**,** or for a maximum of 5000 steps. Then an equilibration was performed in the NVT ensemble maintaining positional restraints on solute heavy atoms. Equilibration was carried out using a leap-frog integrator with a 1 fs timestep, for 2.5 ns or 1.25 ns.

For the production MD the Verlet cutoff scheme was employed for neighbor searching, with the neighbor list updated every 20 steps. Electrostatic interactions were calculated using the particle-mesh Ewald (PME) method [94], with a real-space cutoff of 1.2 nm. Van der Waals interactions were tapered between 1.0–1.2 nm to 0, and the cutoff distance was set to 1.2 nm.

Temperature was maintained at 303.15 K using the Nosé–Hoover thermostat with a coupling constant of 1.0 ps, applied separately to solute and solvent groups. Pressure was maintained at 1 bar using the Parrinello–Rahman barostat with isotropic coupling, a relaxation time of 5.0 ps, and a compressibility of 4.5×10^{-5} bar^{-1}.

All bonds involving hydrogen atoms were constrained using the LINCS algorithm [95], allowing the use of the 2 fs integration time step. Energies were written to the trajectory every 1 ps, while coordinates were saved every 20 ps for the analysis.

Four 500 ns long independent simulations were run for a total length of 2 μs.

To model the MMACHC-R161Q mutant Arg-161 was changed to Gln using the rotamers tool in UCSF ChimeraX 1.5. The simulation of the mutant was run in the same conditions as the wild type.

3.7.2. Simulation of the apo forms

The coordinates of the wild type MMACHC were extracted from the pdb file 3SB0 [61]. The model included three malonate ions that were present in the crystallographic cell. The input was generated using the module “Solution Builder” on CHARMM-GUI, using ParamChem NSF [96] service to parametrize the malonate ions. Ten parallel simulations of a total length of 300 ns were run as described above. The last simulation was prolonged to 1 μs and the configuration of the latter was used as a starting point for ten additional independent simulation of 300 ns.

To model the MMACHC-R161Q and the MMACHC-G147A mutant Arg-161 was changed to Gln and Gly-147 to Ala respectively using the rotamers tool in UCSF ChimeraX 1.5. The simulations of the mutants were run in the same conditions as the wild type, extending them to 2 μs in the case of MMACHC-R161Q and 1 μs in the case of MMACHC-G147A.

3.7.3. Simulations of the apo forms at high temperature

For MMACHC-WT and MMACHC-R161Q the configurations at t = 1 μs from the simulations described in the above subparagraph were used to perform a 40 ns simulation increasing the temperature from 303.15 K to 343.15 K at a constant rate. After 100 ns of simulation at 343.15 K, the temperature was further increased to 383.15 K in 40 ns as described above and then 1 μs of simulation was run. The MD simulation protocol is presented in Fig. 19. The stepwise increase in temperature allowed us to monitor the degree of disorder at different simulated temperatures.

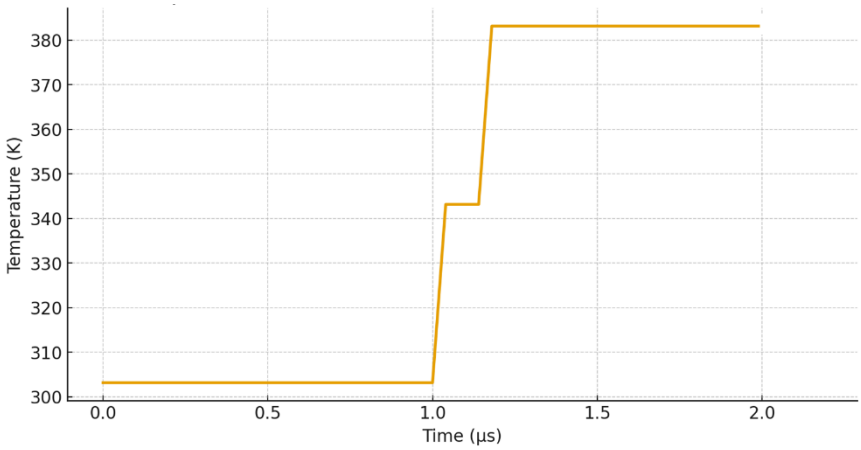

Figure 19. Schematic representation of the MD simulation protocol used to reach 383.15 K through two thermal jumps of 40 ns each

The analysis of the resulting trajectories was performed using VMD 1.9.4 [97], UCSF ChimeraX 1.5 and homemade code using the python library MDAnalysis [98].

To run the simulations and the analysis we used initially nodes of the Galileo supercomputer and then, for most of the work, a local server featuring nodes each with two AMD EPYC 7552 48-core processors.

3.8. Oligomer formation

The investigation on the oligomer formation of MMACHC-WT and MMACHC-R161Q was performed by using two separation techniques: Blue Native polyacrylamide gel electrophoresis (BN-PAGE) and size exclusion chromatography (SEC).

3.8.1. Blue native gel electrophoresis (BN-PAGE)

Native PAGE is an electrophoretic technique specifically designed to separate protein complexes under native conditions, thus preserving their structure and functional interactions. In **Blue Native PAGE (BN-PAGE)** proteins are bound by the anionic dye Coomassie Brilliant Blue G-250, which confers a uniform negative charge proportional to protein mass and independent of their isoelectric point, without disrupting their native conformation. As a result, the migration and the separation depend primarily on the hydrodynamic size of the species in the sample [99].

Blue native-PAGE was conducted using 12 μM protein (wild type MMACHC or R161Q mutant) in the presence or absence of 120 μM AdoCbl, MeCbl, CNCbl, and/or 4 mM GSH. Samples were pre-incubated in the dark at room temperature for 1 hour before being loaded on a native 4–16% Bis-Tris polyacrylamide gel (Life Technologies).

Electrophoresis was performed at 4°C, initially in Dark Blue Cathode Buffer for 40 minutes at 150 V. The buffer was then replaced with Light Blue Cathode Buffer, and the run continued at 250 V for 60 minutes. Gels were stained with InstantBlue™ and scanned using the LiCor Odyssey Imaging System 9120. Band intensities were analyzed using Image J software for densitometric quantification [100].

3.8.2. Size exclusion chromatography (SEC)

Size exclusion chromatography (SEC) is a chromatographic technique that allows the separation of the components of a solution based on their size. Unlike other chromatograpic techniques, molecules do not bind to the resin, that consists of a porous matrix of spherical particles (beads) that act as a reverse sieve. After sample has entered the column, molecules larger than the pores are unable to diffuse into the beads, so they elute first, while smaller molecules will penetrate the pores to varying degrees based on their size and elute after (visual representation in Fig. 20A). The choice of the resin depends on the molecular-mass range that has to be separated. In the case of polar elution solvents, the technique is known as gel filtration chromatography.

The visual output of the chromatography is the chromatogram, that plots the detector response (in our case, the Abs at 280 nm) vs the retention time or volume (Fig. 20B). An optimal separation consists into well-resolved peaks, each of them corresponding to a single component of the mixture. The area under the peak is proportional to the concentration of the analyte.

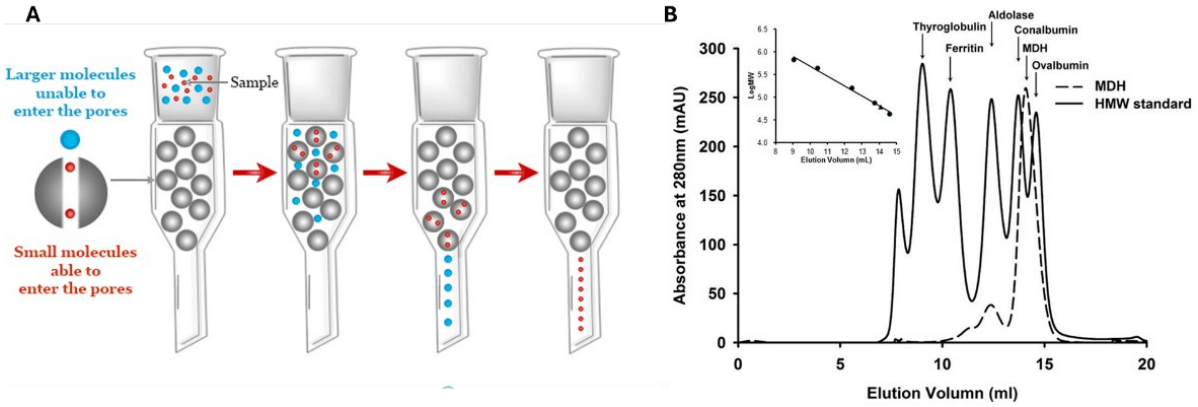

Figure 20. Schematic representation of the principle of size exclusion chromatography (**A**) and exemplificative chromatogram (**B**). Panel A adapted from Sino Biologicals and panel B from *Hung et al., PLoS One, (2013)*

Analytical gel filtration was performed using Superdex 200 Increase 10/300 GL (Cytiva) pre-equilibrated with 20 mM PB pH 7.4, 300 mM NaCl, 5% v/v glycerol, on a modular Prominance Shimadzu HPLC device, equipped with a mobile phase degasser (DGSU-20As), a quaternary pump (LC-2010 AT) and a photodiode array detector (SPD-M20A). MMACHC-WT or MMACHC-R161Q (15 µM) were incubated for 10 min at room temperature with AdoCbl in a molar ratio 1:10 and eluted with the same buffer used for the equilibration**.**

3.9. Dealkylation assay

Ultraviolet–visible (UV-Vis) spectroscopy is an analytical technique based on the absorption of electromagnetic radiation in the ultraviolet (200–400 nm) and visible (400–800 nm) regions of the spectrum. When a photon of suitable energy interacts with a molecule, it can promote an electron from a lower-energy orbital to a higher-energy orbital, thus inducing an electronic transition.

The recorded spectrum represents the absorbance as a function of wavelength and provides information on the electronic structure of the analyte.

The position of the absorption maxima (λmax) is characteristic of the specific chromophores present in the molecule, whereas the intensity of the bands is proportional to the concentration of the absorbing species according to the Lambert-Beer law:

$$A = \varepsilon \times C \times l$$

where A is the absorbance, ε the molar extinction coefficient, C the concentration, and l the optical path length.

In the context of proteins, UV absorbance is mainly due to aromatic amino acid residues (the absorbance at 280 nm, for example, is routinely used to estimate protein concentration) and to the peptide bond, which strongly absorbs at 190–220 nm. Regarding the vitamin B12, the

absorbance in the far-UV is related to the corrin π system, in the near-UV to the π→π* transitions of the corrinic ring, while the bands in the visible region are strongly influenced by the oxidation state of the cobalt and the nature of the β-axial ligand. These spectroscopical properties can be used to evaluate the enzymatic activity of MMACHC protein, evaluating the changes in the absorbance spectrum of MeCbl upon removal of the β-axial ligand due to the addition of GSH.

Dealkylation activity was monitored as previously described [65] with minor modifications. A solution containing 16 μM protein was incubated with 12.8 μM MeCbl in the absence or presence of 0.5 M betaine or 16 μM M3 or M6 or rutin for 10 minutes at room temperature. The reaction was started by the addition of 1 mM GSH. Spectra were recorded using a SHIMADZU UV-VIS Spectrophotometer at 20 °C. The time dependence of dealkylation activity was monitored following the increasing absorption at 353 nm in time. Data were expressed as the increase in absorbance at 353 nm normalized to the initial value, as follows $(Abs_{353nm}(t)–Abs_{350nm}(t_0))/Abs_{350nm}(t_0)$, where t_0 represent the time of GSH addition. The data were analysed by interpolating experimental points with a single exponential fit of the form $y = y_0 + a(1 - \exp(-bt))$. The observed dealkylation rate constants k_{obs} were determined from the fit as $y'(0) = ab$.

3.10. Isothermal denaturation (ITD)

High-throughput screening for osmolyte-induced stabilization was performed by monitoring the isothermal denaturation of MMACHC-WT and MMACHC-R161Q in the presence of the extrinsic fluorescent probe SYPRO Orange (Invitrogen).

MMACHC-WT and MMACHC-R161Q were diluted to 0.1 mg/ml (3 μM) in buffer containing 20 mM PB pH 7.4, 300 mM NaCl, 5% v/v glycerol with 1:1000 SYPRO Orange (Invitrogen) and 0.5 M of different osmolytes (betaine, proline, arginine, trehalose). Samples of both proteins were kept at a constant temperature of 38 °C while the fluorescence of the probe was monitored by a Fluoroskan™ FL Microplate Fluorometer, equipped with 485 nm excitation and 538 nm emission filters.

3.11. Active Site Prediction, Ligand Preparation and Docking

Molecular docking is the most frequently used structure-based approach to predict interactions between protein targets and small molecules.

This method allows the prediction of the most favorable binding pose of each ligand within a protein's binding region and provides an estimation of the associated binding free energy. In brief, docking simulations rely on the three-dimensional structure of the target and the chemical structure of the ligands to generate multiple possible orientations of each compound inside a defined region of the protein. A sampling algorithm explores the conformational space to identify the most energetically favorable configuration of each molecule, evaluating each pose by a scoring function. These steps yield a predicted binding mode for each compound, together with a numerical score that reflects the strength of the interaction, from which a ranking is obtained (Fig. 21) [101].

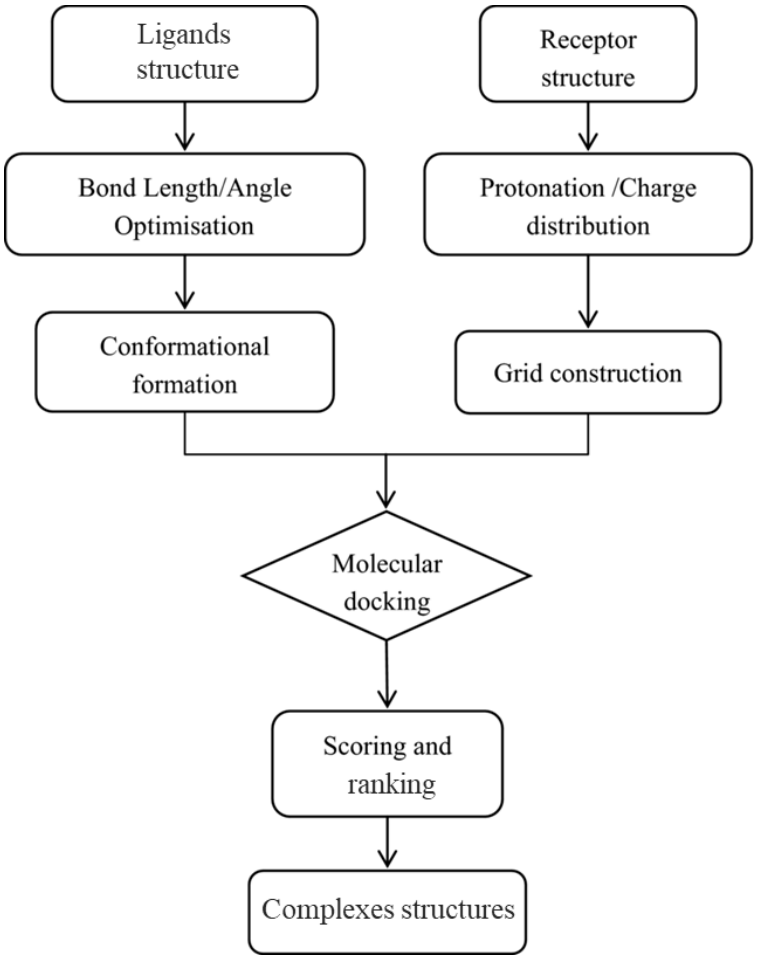

Figure 21. Flowchart of classical molecular docking. Figure adapted from *Tao et al., Int. J. Food Sci. Technol. (2019)*

The coordinates of MMACHC protein, in complex with GSH, were extracted from the pdb file 5UOS [63]. MeCbl coordinates were extracted from the pdb file 3SC0 [2]. The two pdb files

were aligned using the matchmaker tool of UCSF ChimeraX 1.5 [102]. To model the MMACHC-R161Q mutant, Arg-161 was changed to Gln using the rotamers tool in ChimeraX. The protein was prepared with the Protein Preparation Wizard of Maestro Suite Software [103], adding bond orders and hydrogen atoms to the crystal structure using the OPLS_2005 force field [104]. Next, Prime [105] was used to fix missing residues or atoms in the protein and to remove co-crystallized water molecules. The protonation states at pH 7.2 ± 0.2 of the protein and the ligands were evaluated using Epik [106]. The hydrogen bonds were optimized through the reorientation of hydroxyl bonds, thiol groups, and amide groups. In the end, the systems were minimized with the value of convergence of the RMSD of 0.3 Å.

The binding pocket of MMACHC-R161Q mutant model, has been searched by using the SiteMap tool of Maestro Suite Software [107]. The Sitemap tool was used on the entire protein (all atoms in the workspace), setting at least 15 site points per receptor site and reporting up to 5 sites. The hydrophobicity parameter was set as more restrictive and a standard grid was chosen. The site maps identified were then cropped at 4 Å from the nearest points. A grid of 20 Å was centered on the first map obtained, in order to perform a virtual screening of DrugBank Database [108] and FDA-approved drugs library. The molecules were prepared using Schrödinger LigPrep. The Force Field adopted was OPLS_2005, and Epik was selected as ionization tool at pH 7.2 ± 0.2. The maximum number of conformers generated was set at 32. The docking was performed using Glide docking tool [109]. The Van der Waals radius was 1 Å, and the partial charge cut-off was 0.15 Å with flexible ligand sampling. Bias sampling torsion penalization for amides with non-planar conformation and Epik state penalties were added to the docking score. The Virtual Screening was performed following three different consecutive docking steps: High Throughput Virtual Screening (HTVS), Standard Precision (SP), and Extra Precision (XP).

3.12. Differential scanning fluorimetry

High-throughput screening for ligand-induced stabilization was performed by monitoring the thermal denaturation of MMACHC-WT and MMACHC-R161Q in the presence of the extrinsic fluorescent probe SYPRO Orange (Invitrogen).

Experiments were performed in Thermo Fisher StepOnePlus Real-Time PCR System. Protein-ligand solutions were dispensed into 96-well microplates, overlaid with an adhesive film. Protein solutions contained 0.1 mg/ml of protein (3 μM) in 20 mM PB pH 7.4, 300 mM NaCl, 5% v/v glycerol and 1:1000 SYPRO Orange. Ligands dissolved in DMSO were added at a final concentration of 150 μM to microplates containing the protein solutions and incubated at room

temperature for 30 minutes before loading onto the microplate reader. Control experiments in the absence of DMSO and/or ligands were routinely performed in each microplate. Thermal denaturation was monitored by following the temperature-depending SYPRO Orange fluorescence intensity associated with protein unfolding, using the ROX filter (λ_{exc} = 586 and λ_{em} = 612 nm, where λ_{exc} is excitation wavelength and λ_{em} is emission wavelength). Unfolding curves were registered from 25 to 95°C, at a 1°C/min scan rate. Each experiment was run in triplicate.

3.13. Construction of p-EGFP-N1-MMACHC-WT and mutagenesis

In order to obtain the reporter system for the test of TRIDs we generated a plasmid coding for MMACHC-GFP by restriction cloning.

Restriction cloning is a molecular biology technique that uses restriction enzymes to cut a DNA fragment (insert) and a plasmid vector at specific recognition sites, producing compatible ends. A DNA ligase then joins these DNA pieces together, creating a circular recombinant DNA molecule (Fig. 22) [110]. The process involves the following steps:

1. **Selection of the restriction enzymes:** commercial vectors usually contain a multicloning site (MCS), a sequence rich in restriction sites of different enzymes
2. **Amplification of the insert:** a gene of interest (the insert) is amplified using techniques like PCR, which can be used to insert the restriction sites
3. **Digestion of the DNA:** both the insert and the plasmid vector are digested with the same restriction enzymes. This process creates DNA fragments with compatible ends, such as single-stranded sticky ends or blunt ends.
4. **Ligation of the fragments:** the cut insert and vector are mixed together with DNA ligase. The ligase induces the formation of covalent bonds between the DNA fragments into a single, circular recombinant plasmid.
5. **Transformation:** the recombinant plasmid is then introduced into host cells, usually *E. coli*, through a process called transformation.
6. **Amplification:** the transformed bacteria replicate the plasmid, allowing for the extraction and verification of the desired recombinant DNA.

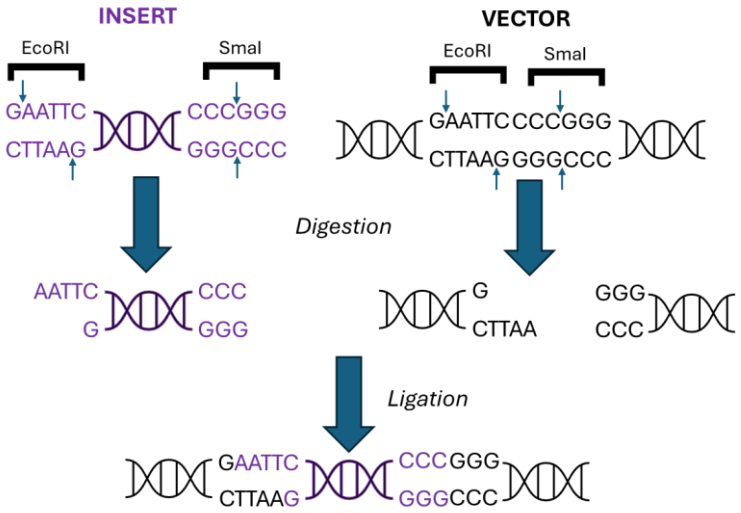

Figure 22. Schematic representation of restriction cloning using EcoRI and SmaI. Restriction sites are highlighted in purple for the insert and in black for the vector

The steps of the cloning are monitored by **agarose gel electrophoresis**, a technique that separates DNA fragments by size, using an electric field to drive the negatively charged DNA through a sieve-like agarose gel matrix. Smaller fragments move faster through the gel's pores than larger fragments, resulting in a separation based on size. The DNA bands are then visualized using a stain, often under UV light [111].

2 µg of pEGFP-N1 vector (GenBank Accession #U55762) was digested with the restriction enzymes EcoRI and SmaI (New England Biolabs) in a final volume of 35 µL for 4 hours at 37 °C. The digestion mixture was resolved on a 0.8% agarose gel and the band corresponding to the plasmid was excided from the gel and purified with GenElute Gel Extraction Kit (Sigma-Aldrich).

The insert coding for MMACHC-WT (without the stop codon) with the EcoRI restriction site on the 5' end and the SmaI restriction site on the 3' end was obtained by PCR from the plasmid pNIC28-Bsa4-MMACHC-WT using **GGAATTCATG**GAGCCGAAAGTCGCAGAGCTGAAGCAGAAGATCGAGG and **TCCCCCGGG**TAGGGCCAGGGGATGCAGGTGGTGAGACCCT as primers (letters in bold represent the restriction sites). PCR was performed using Taq DNA polymerase (Sigma-Aldrich D4545), with the following protocol, repeating steps 2 to 4 for 25 cycles:

1. Initial denaturation 95 °C for 2 min
2. Denaturation 95 °C for 20 s
3. Annealing 57 °C for 20 s
4. Extention 68 °C for 30 s
5. Final extention 68 °C for 5 min

After digesting the parental DNA with DpnI, the amplified DNA insert was purified using GenElute PCR Clean Up kit (Sigma). The insert was then digested with the restriction enzymes EcoRI and SmaI (New England Biolabs) in a final volume of 15 µL for 4 hours at 37 °C and then purified again with GenElute PCR Clean Up kit (Sigma).

The digested insert and plasmid were ligated in a molar ratio 3:1 in a final volume of 10 µL using T4 DNA ligase (Promega M8221) for 2 hours at room temperature and then at 4 °C overnight.

The ligation product was transformed into ultracompetent *E. coli* XL-10 Gold (Agilent Technologies, Inc.), from which the plasmid DNA was extracted. The nucleotide sequence was confirmed by Sanger sequencing.

The p-EGFP-N1-MMACHC-R132X and p-EGFP-N1-MMACHC-Y222X plasmids carrying the nonsense mutations c.394C>T and c.666C>A in the MMACHC coding region were generated by site-directed mutagenesis of the wild-type vector using QuikChange Lightning Site-Directed Mutagenesis Kit (Agilent Technologies, Inc.) and the primers

- CTGCTTACTACTACCAA**T**GACAAGATGTGGAGGC and GCCTCCACATCTTGTC**A**TTGGTAGTAGTAAGCAG for R132X
- GAAGAGCAGAAGGCCTA**A**TTCTCCACTCCACCTG and CAGGTGGAGTGGAGAA**T**TAGGCCTTCTGCTCTTC for Y222X

where the letters in bold represents the mutated nucleotide that generates the stop codon.

The nucleotide sequence was confirmed by Sanger sequencing.

3.14. Attempts of purification of other MMACHC pathological variants

Mutants sequences were generated by site-directed mutagenesis of the wild-type vector pNIC28-Bsa4-MMACHC-WT using QuikChange Lightning Site-Directed Mutagenesis Kit (Agilent Technologies, Inc.) and the primers

- AACCAGCGCATATCAG**C**TGTGTGCATACACCCCC and GGGGGTGTATGCACACA**G**CTGATATGCGCTGGTT for G147A
- GTGATTGGACTTACC**C**GGATGCTGTGACACCCC and GGGGTGTCACAGCATCC**G**GGTAAGTCCAATCAC for R206P
- GGGGCTGCTTACTACT**G**CCAACGACAAGATGTGG and CCACATCTTGTCGTTGG**C**AGTAGTAAGCAGCCCC for Y130C

where the letters in bold represent the mutated nucleotides.

The nucleotide sequence was confirmed by Sanger sequencing.

The strategies used to recover the MMACHC-G147 protein, after the failure of the protocol used for the purification of MMACHC-WT and MMACHC-R161Q, consisted in both denaturing (subparagraphs *3.14.1* and *3.14.2*) and non-denaturing (subparagraphs *3.14.3* and *3.14.4*) approaches. In general, the steps until the expression of the recombinant protein were carried out as described in *3.2*. Any modification of the protocol will be made explicit in the specific subparagraph.

3.14.1. In column refolding

The protocol in *3.2*. was followed until the mechanical lysis. After sonication, the supernatant was discarded and the pellet of inclusion bodies was washed with a buffer containing 20 mM PB (10 mM Na_2HPO_4, 10 mM NaH_2PO_4) pH 7.4, 0.5 M NaCl, 10 mM imidazole, 2 mM DTT and 1% (w/v) Triton X-100 twice and then suspended in the same prechilled buffer without Triton X-100 and centrifuged at 20,000 *xg* at 4°C for 15 min. Supernatant was discarded and pellets were suspended in a buffer containing 8 M urea, 20mM PB pH 7.4, 0.5 M NaCl, 2 mM DTT and kept for two hours at room temperature and then at 4 °C overnight. The supernatant was collected after centrifugation at 20,000 *xg*, 4 °C for 30 min, filtered using 0.2 μm filter and loaded onto a 5 mL HisTrap FF column (Cytiva). In column refolding of MMACHC-G147A protein was carried out with a linear gradient from 8 M to 0 M urea and then eluted with a linear gradient from 10 mM to 500 mM imidazole.

3.14.2. Dialysis

After the extraction of the inclusion bodies as in *3.14.1*, the sample was loaded into a dialysis membrane cut-off 1500 Da, in the absence or presence of AdoCbl (1:5) and dialyzed against 2 M urea, 20 mM PB pH 7.4, 0.5 M NaCl, 2 mM DTT overnight at 4°C first and then against 20 mM PB pH 7.4, 0.5 M NaCl, 2 mM DTT overnight at 4 °C. The experiment was repeated at various dilution ratios of the sample.

3.14.3. Use of N-lauroyl sarcosine during extraction and purification steps

The same protocol described in *3.2* was followed, adding 0.3% w/v N-lauroyl sarcosine to each buffer used.

3.14.4. Change of the host strain and supplementation of betaine for the induction

Rosetta 2(DE3) cells harboring pNIC28-Bsa4-MMACHC-G147A (or -R206P or -Y130C) were grown in Terrific Broth (TB) at 37 °C. When the OD_{600} reached 2, cultures were moved at 4 °C and a final concentration of 0.5 M NaCl and 5 mM betaine was added to the medium. From this point, the same protocol described in *3.2* was followed.

4. Results

In this chapter, the experimental and computational results concerning the biophysical characterization of the structural properties, conformational stability, binding to cofactors (cobalamins and GSH), oligomeric equilibrium, and functional features of the wild-type MMACHC protein (WT) are presented. These data are compared with those obtained for its pathogenic variant MMACHC-R161Q, involved in *cblC* disease, which proved to be soluble as recombinant protein and, together with other variants, has been predicted to be structurally destabilized. Additional results are reported on the effects of osmolytes, chemical compounds with stabilizing properties, on the stability and functionality of the R161Q mutant. Furthermore, a preliminar investigation into viable therapeutic strategies for the treatment *of cblC* disease is presented. Lastly, we report an overview of the attempts of purification of the MMACHC-G147A pathogenic variant as a recombinant protein, together with its characterization using molecular dynamics.

4.1. Selection of the pathological mutant

The MMACHC pathological variants to study were selected using PremPS [112], a computational tool that allows to predict the destabilizing effect of a missense mutation on the protein structure, evaluating the difference in folding free energy resulting from the substitution of the involved residue with alanine. Based on the free energy variation values (ΔΔG), we selected four point mutations: R161Q, R206P (both located in the GSH binding site), G147A and Y130C (both located in the cobalamin-tail binding site). After producing the plasmids for the heterologous expression of the proteins by site-directed mutagenesis from the WT plasmid, we performed an expression screening in *E.Coli* BL-21 (DE3) that showed that the recombinant proteins are present in the bacterial pellet, but not in the soluble fraction, except for the R161Q mutant protein (Fig. 23).

After several failed attempts to produce the insoluble proteins, that will be discussed in the last paragraph, and the succeed in producing the MMACHC-R161Q mutant, we decided to investigate its structural and stability properties to understand whether it could be representative of pathological mutations that affect the structure and stability of MMACHC, making it potentially susceptible to correction by pharmacological chaperones.

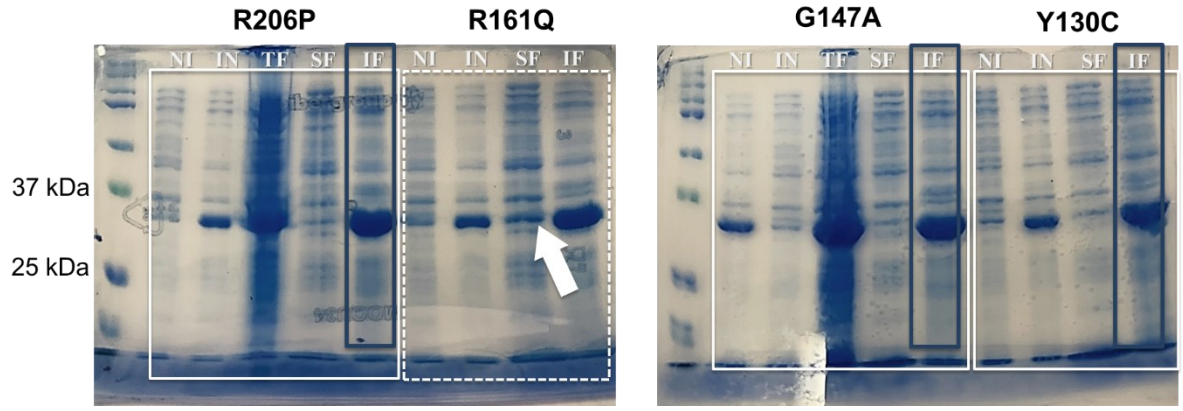

Figure 23. SDS-PAGE monitoring the expression and the solubility of four MMACHC pathogenic variants. The arrow indicates the band corresponding to the soluble His-tagged MMACHC-R161Q protein. Legend: NI (not induced), IN (induced), TF (total fraction), SF (soluble fraction), IF (insoluble fraction)

4.2. MMACHC-WT and MMACHC-R161Q display similar secondary and tertiary structures

Our first step was to compare the secondary and tertiary structures of MMACHC-WT with those of the MMACHC-R161Q pathological mutant to characterize the impact of the mutation on the protein structure. To this end, we used spectroscopic techniques, including circular dichroism (CD) in the near- and far-UV regions, as well as intrinsic fluorescence measurements.

First, we obtained the recombinant MMACHC-WT and R161Q mutant purifying them from the soluble fraction of the total bacterial lysate as His-tagged native proteins; these serve as the model system investigated in this thesis. The secondary structure of MMACHC-WT, verified by acquiring the CD spectrum in the far-UV region, revealed the abundance of alpha helices, as evidenced by characteristic minima at 208 and 222 nm, in good agreement with the crystal structure [61], [62]. The comparison with the mutant spectrum revealed minimal changes in the secondary structure content (Fig. 24). Although minimal, these changes can be considered significant, as they are consistently observed across several replicates performed on different batches and aliquots.

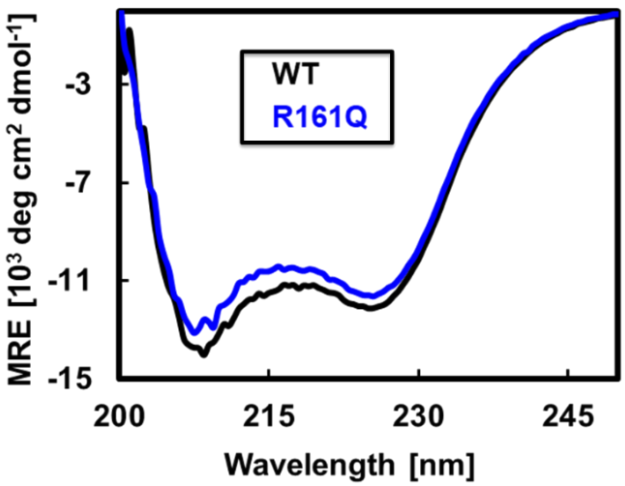

Figure 24. Far-UV CD spectra of apo MMACHC-WT (10 µM) and MMACHC-R161Q (10 µM)

Interestingly, also the near-UV CD spectra were superimposable, indicating that at T=20 °C the two proteins share a similar folding profile (Fig. 25A). This was further confirmed by analyzing the intrinsic fluorescence emission of both MMACHC-WT and MMACHC-R161Q. Of note, these proteins are rich in aromatic residues, comprising 12 phenylalanines, 10 tyrosines and 5 tryptophans; therefore, the fluorescence signal reflects a collective contribution rather than a localized response. The obtained emission spectra after excitation at 260, 275 and 295 nm are reported in Fig. 25B. Although MMACHC-WT and MMACHC-R161Q exhibit an identical spectral shape, peaking at the same maximum wavelength after each excitation, the intensity of the maximum is always lower in the case of the mutant, showing an approximate 25% reduction across all the examined excitation wavelengths. This difference in the quantum yield suggests an increase in the intramolecular quenching or an enhanced exposure to the solvent due to a higher flexibility in the case of the mutant, that is not surprising considering that mutation of the positive-charged arginine into a neutral glutamine can induce local alterations that propagate throughout the protein.

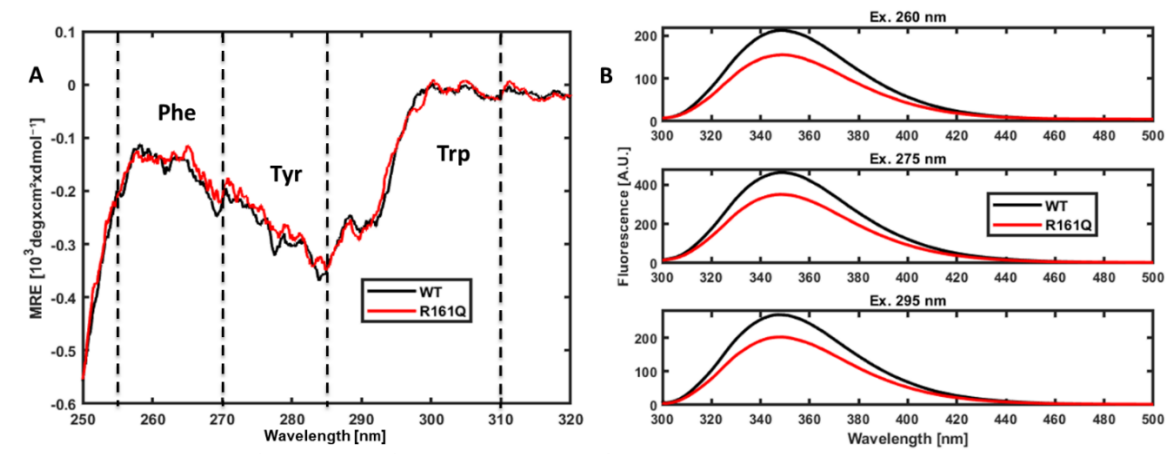

Figure 25. Comparison of the near-UV spectra and intrinsic fluorescence measurements of MMCHC-WT and MMACHC-R161Q. **A.** Near-UV CD spectra (protein concentration 14 µM) **B.** Emission spectra of after excitation at 260 nm (upper panel), 275 nm (middle panel) and 295 nm (lower panel) (protein concentration 3 µM)

4.3. MMACHC-WT and MMACHC-R161Q follow distinct thermal unfolding pathways

The next step was to analyze the stability of the two proteins by studying their thermal unfolding pathway and the populations of structural intermediates. To this end, in addition to CD measurements, we used differential scanning calorimetry (DSC), which provides access to all the thermodynamic parameters associated with the denaturation process. Further insights were gained from molecular dynamics simulations, which allowed us to explore the conformational landscape and the stability of key structural elements at the atomic level.

A strong similarity of the secondary structure and folding profile between WT and the R161Q mutant at 20 °C does not guarantee an identical thermal stability. Indeed, the thermal unfolding profile of MMACHC-R161Q, obtained by monitoring the changes in ellipticity at 222 nm as a function of temperature, revealed a markedly different behaviour from that of the WT, both in the presence and in the absence of AdoCbl, previously reported as the most stabilizing ligand among the different forms of cobalamin [52] (Fig. 26). In fact, although at first sight the two apoproteins showed minor differences in their melting temperatures, the shape of the two unfolding curves is appreciably different, with the WT one being associated to a more stretched profile. The unfolding profile of the wild-type protein indeed reveals the presence of two transitions, as also suggested by Froese et al. [52], and it could only be fitted using a two-transition model. On the other hand, the MMACHC-R161Q mutant CD thermal unfolding could be analyzed by using a single transition model.

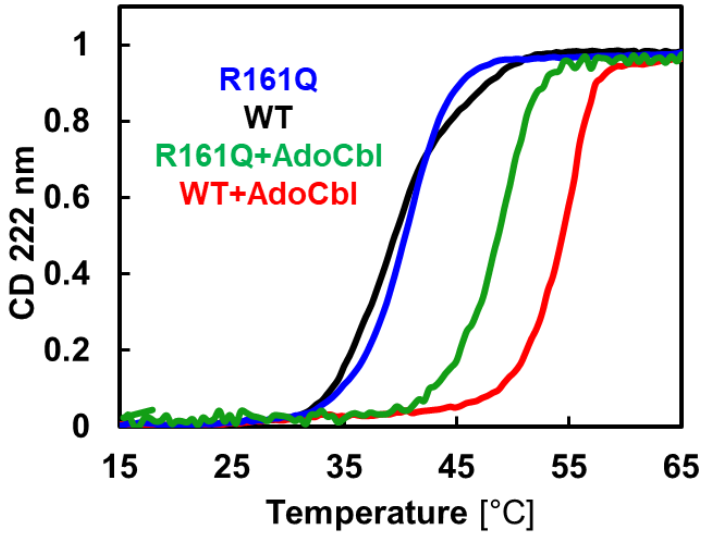

Figure 26. Thermal denaturation curves of MMACHC-WT (10 μM) and MMACHC-R161Q (10 μM) obtained by measuring the ellipticity at 222 nm as a function of temperature in the absence and in the presence of AdoCbl (20 μM). The ellipticity values have been normalized for appropriate comparison

In Table 1 the unfolding temperatures obtained for the two wild-type protein transitions and the single mutant transition are reported both in the absence and in the presence of AdoCbl.

		-Cbl	+Cbl
WT	T_{m1}	38.5 ± 0.1 °C	52.2 ± 0.1 °C
	T_{m2}	46.9 ± 0.1 °C	56.1 ± 0.1 °C
R161Q	T_m	40.2 ± 0.2 °C	45.8 ± 0.1 °C

Table 1. Unfolding temperatures resulting from the fitting of the CD thermal denaturation data with two-state model (single transition), in the case of MMACHC-R161Q mutant, and with three-state model (two-transition) in the case of MMACHC-WT protein

As shown in Table 1, the unfolding temperature changes substantially in the presence of AdoCbl both for wild type and for the mutant. Moreover, it appears that the less stable domain of MMACHC is more significantly influenced by the binding of AdoCbl.

The presence of two transitions in the thermal denaturation of MMACHC-WT protein becomes evident from the thermograms resulting from DSC experiments (Fig. 27).

As for the case of CD unfolding profile, the wild-type protein data could not be analyzed considering a single transition model, but an additional transition needs to be added to reproduce the experimental data. However, very interestingly, also the DSC curve for the MMACHC-R161Q mutant had to be analyzed by assuming the presence of two transitions, thus, considering low-populated intermediate conformations. The thermodynamic parameters obtained from the calorimetric analysis for both proteins are reported in Table 2. While the unfolding temperature of the first transition, T_{m1}, is the almost the same for the two proteins, the second unfolding temperature, T_{m2}, is significantly lower for the mutant with respect to wild-type, and close to T_{m1}. Hence, in the case of MMACHC-R161Q the two transitions considerably overlap giving rise to a single broader peak which can be apparently associated to a single transition. This also explains why the CD assay shows a single apparent transition (a trial to fit the profile with two distinct transitions failed due to convergence issues in the fitting procedure).

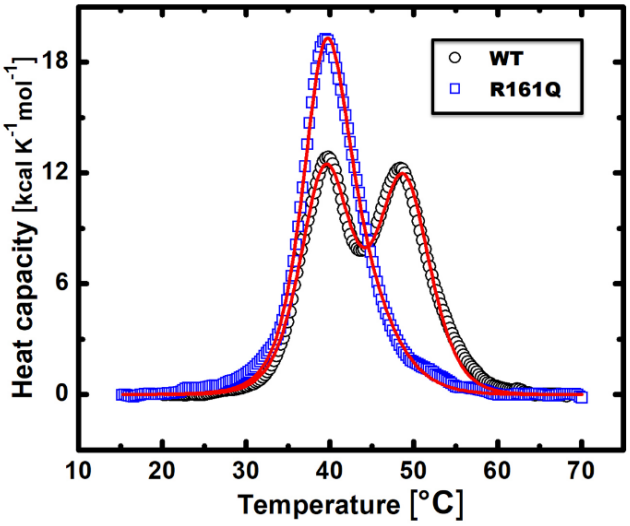

Figure 27. DSC thermograms of apo MMACHC-WT (17 μM, black circles) and MMACHC-R161Q (17 μM, blue squares). The experimental data (empty symbols) and the theoretical fit of the data to a two-transition model (continuous lines) for both proteins are shown

	T_{m1}(°C)	ΔH_{m1} (kcal/mol)	T_{m2} (°C)	ΔH_{m2} (kcal/mol)
WT	39.2 ± 0.1	96 ± 2	48.6 ± 0.1	97 ± 2
R161Q	39.3 ± 0.1	109 ± 2	42.1 ± 0.1	65 ± 2

Table 2. Thermodynamic parameters resulting from the analysis of the DSC thermograms

Since the unfolding enthalpy and the unfolding temperature of the first transition are similar for both proteins, the stabilization energy gap between the folded state and the first intermediate state are comparable. However, the lower unfolding enthalpy and unfolding temperature for the second transition in the mutant implies that the main intermediate conformational state for the mutant is either less stable or structurally different from that of the wild type, possibly leading to a more destabilized overall folding pathway. This can be observed when calculating the populations of the different states as a function of temperature, using the parameters obtained from the DSC assays, according to equation 12 (paragraph *3.4*. of the methods section) (Fig. 28). In the case of the WT, the first intermediate reaches a maximal population of 0.82 at 43.8 °C, but the second intermediate is barely populated, resulting in a three-state scenario (i.e. only one intermediate conformation is represented). Instead, in the case of the R161Q mutant, the first intermediate has a much lower presence with a maximal population of 0.43 at 41.3 °C, but the second intermediate has a non-negligible role with a maximal population of 0.15 at 38.7 °C, resulting in a four-state scenario (i.e. the unfolding process involves two intermediate conformations).

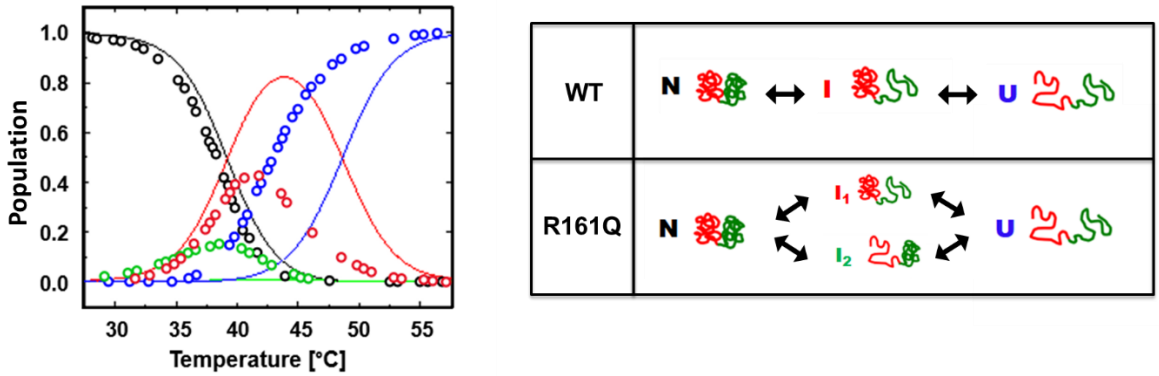

Figure 28. Temperature dependence of the populations of the different conformational states for MMACHC-WT (continuous lines) and MMACHC-R161Q (dotted lines): folded state (black), first intermediate state (red), second intermediate state (green), and unfolded state (blue). A graphical schematization of the two distinct unfolding pathways is also provided (N: native state; I1: first intermediate state, I2: second intermediate state, U: unfolded state).

The stability profile of the MMACHC protein was also assessed in the presence of different forms of cobalamins. Consistent with the earlier studies [52], the cobalamins showed a hierarchy of stabilizing effects on the WT, ranging from the least stabilizing CNCbl to the most

stabilizing AdoCbl, with MeCbl showing an intermediate stabilizing effect (Fig. 29A). In the case of the R161Q mutant, the same stabilization ranking was obtained for the ligands. However, the stabilization effects of the cobalamin cofactors were considerably reduced for the mutant compared to the WT (Fig. 29B).

Considering that the mutated residue is located outside the cobalamin-binding site, we propose that the effect of the R161Q mutation can be attributed to local structural changes elicited by the mutation that propagates in other regions, ultimately influencing the cobalamins binding.

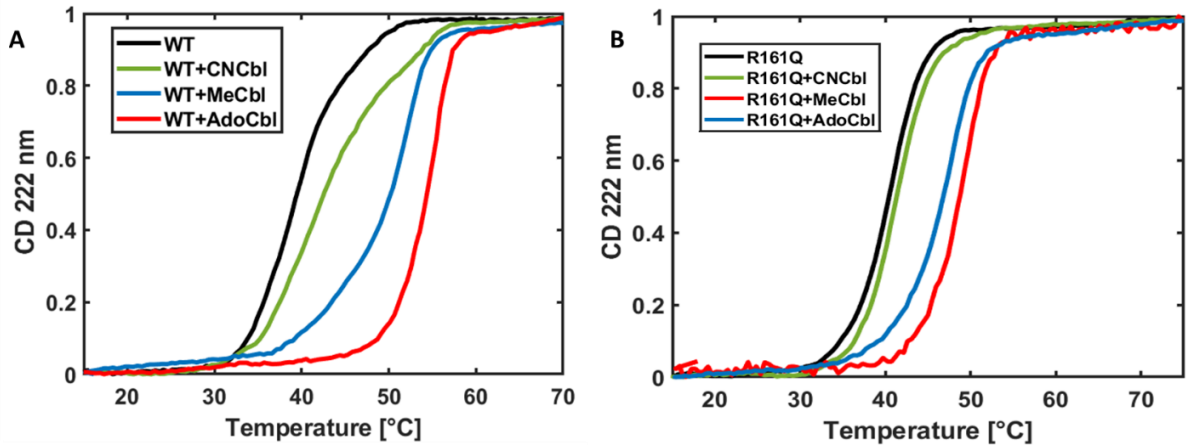

Figure 29. Thermal denaturation curves of MMACHC–WT (10 μM) (**A**) and MMACHC–R161Q (10 μM) (**B**) in the absence and in the presence of different cobalamins (20 μM) obtained by monitoring the ellipticity signal at 222 nm as a function of temperature. The ellipticity values have been normalized for appropriate comparison

To better understand the impact of the R161Q mutation on the thermal unfolding process of the protein, we conducted MD simulations at high temperatures. Specifically, the temperature of the MMACHC-WT and MMACHC-R161Q systems was increased in two steps of 40 K each, starting from 303.15 K, with heating ramps lasting 40 ns each. It is important to note that temperature increases in MD simulations do not directly correspond to real experimental conditions, since force fields tend to over stabilize the structures [113]. Due to the limited timescales accessible in MD [114], elevated temperatures are commonly used to accelerate unfolding events and enhance sampling [115], rather than to replicate physiological temperature changes. Thus, the observed effects should be interpreted in the context of comparative dynamics under controlled, yet artificial, thermal stress conditions. Because no relevant structural changes were detected in either protein after the first 40 K ramp, we performed a second ramp and then ran a 1 μs simulation. The results revealed that, while the root-mean-square deviation (RMSD) of the wild-type protein — calculated with respect to its most stable region (the N-terminal α-helix and the adjacent β-sheet strand) — remained below 10 Å, the R161Q mutant showed progressively higher RMSD values, peaking at 15 Å (Fig. 30A). This

indicates that, after the two thermal jumps, the mutant loses a significant portion of its tertiary structure, whereas the wild-type protein remains stable.

This also suggests that the simulated thermal jumps do not correspond to a complete unfolding leading to protein full denaturation, but rather to the attainment of an unfolding intermediate state. Moreover, the secondary structure of the R161Q mutant instead differed from the wild type solely by a minor increase in small β-strands (Fig. 30B).

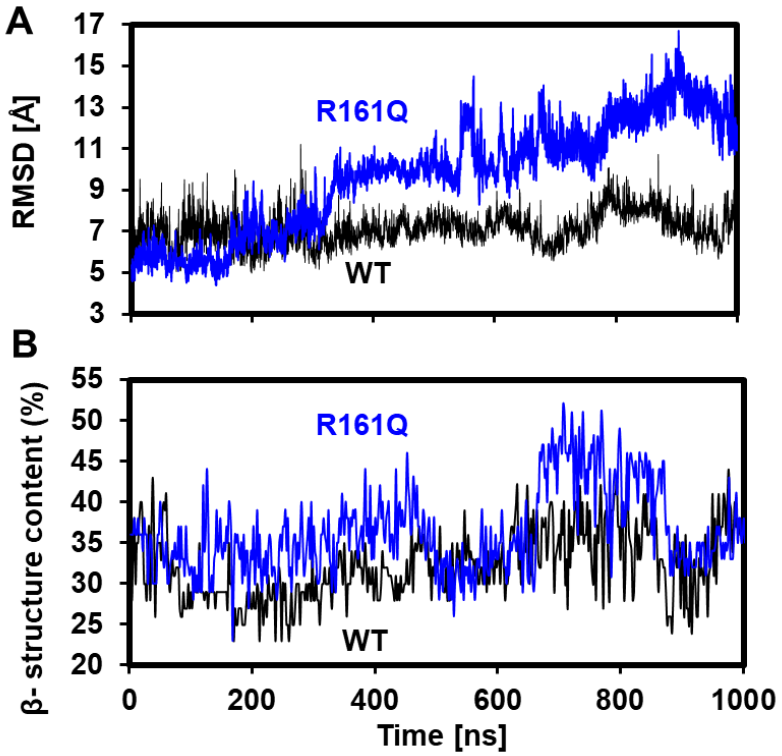

Figure 30. MD characterization of MMACHC-WT and MACHC-R161Q thermal unfolding intermediate along 1 μs of simulation carried out after two temperature jumps, 40 K each, from 303.15 K. **A.** Root-mean-square deviations (RMSD) **B.** Evolution of the β-structure content

4.4. Interaction of MMACHC with the different forms of cobalamin

The thermal unfolding of MMACHC-WT and MMACHC-R161Q proteins revealed that the ligand-induced stability increase for the mutant is considerably smaller than that observed for the wild type. Ligand-induced stabilization effects on proteins provide an indirect method to estimate ligand binding affinities, but they may be misleading because the extent of the stabilization effect is dependent not only on binding affinity and ligand concentration, but also on binding enthalpy, and binding heat capacity. Therefore, we used isothermal titration calorimetry (ITC) to obtain a direct estimation of the binding affinity and the thermodynamic parameters of the interaction. Data were analyzed using a single binding site model, which allowed us to compare the obtained parameters of MMACHC for the various forms of vitamin B12.

The thermograms obtained are shown in Fig. 31. While the binding stoichiometry was consistent across all cobalamins, with a single binding site identified for each, the affinity constants varied significantly among the different cobalamin forms (Table 3). Our data demonstrated that CNCbl exhibited the lowest affinity for MMACHC-WT, with a dissociation constant (K_d) in the micromolar range and in good agreement with Kim et al. [66]. In contrast, AdoCbl displayed a markedly higher affinity, with a $K_d = 15$ nM, while MeCbl showed an intermediate affinity.

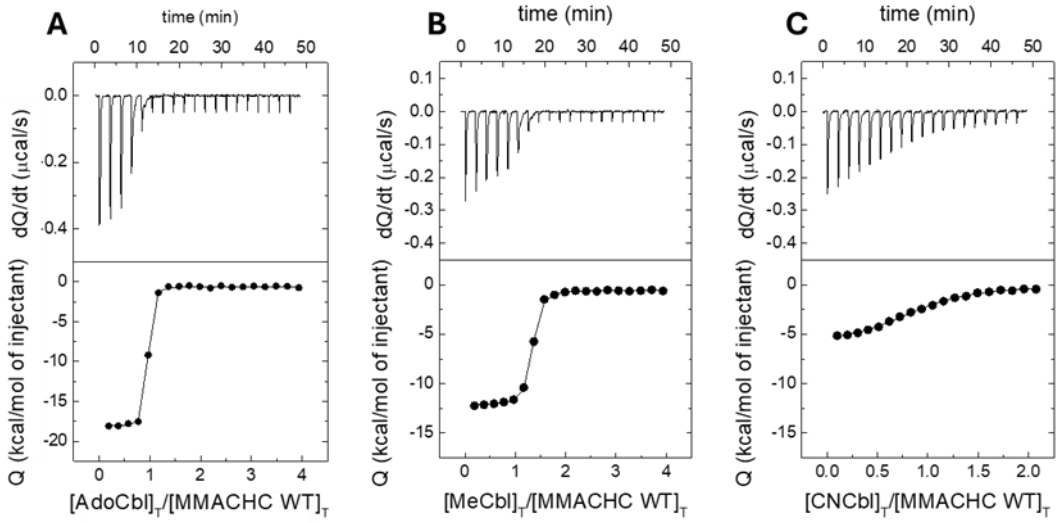

Figure 31. Calorimetric titrations for MMACHC-WT interacting with AdoCbl (**A**), MeCbl (**B**) and CNCbl (**C**). The upper plots provide the thermograms, while the lower plots display the binding isotherms fitted to a single binding site model

Kd	CNCbl	MeCbl	AdoCbl
WT	(5.6 ± 0.7) µM	(48 ± 4) nM	(15 ± 2) nM
R161Q	(56 ± 2) µM	(160 ± 20) nM	(104 ± 8) nM

Table 3. Dissociation constants $K_d=1/K_a$ resulting from ITC experiment obtained titrating MeCbl, CNCbl and AdoCbl into MMACHC-WT and MMACHC-R161Q proteins

As shown in Fig. 32, the binding is enthalpically driven for the three cobalamins. However, AdoCbl, which exhibits the highest affinity, presents also the strongest favorable enthalpic contribution, likely arising from a combination of additional favorable intramolecular interactions accompanying the structuring of MMACHC after AdoCbl binding and hydrogen bonds involving the bulkier adenosyl moiety. This large enthalpic gain compensates for a significant entropic penalty. Instead MeCbl displays a less favorable (less exothermic) enthalpic contribution compared to AdoCbl but also a reduced entropic penalty, suggesting that the MeCbl-MMACHC complex is more flexible than the AdoCbl one. Compared to AdoCbl and

MeCbl, CNCbl binding is less exothermic overall but exhibits a favorable entropic contribution, indicating that the complex remains more flexible (i.e., it undergoes a smaller loss in conformational degrees of freedom) upon binding compared to alkylcobalamins. This could also be addressed to the strong cobalt–cyano bond established in cyanocobalamin, which may inherently limit the conformational flexibility of the corrinic ring [40] and thus the formation of additional stabilizing contacts with the MMACHC protein.

A

MMACHC-WT			
Ligand	**ΔG (kcal/mol)**	**ΔH (kcal/mol)**	**–TΔS (kcal/mol)**
AdoCbl	–10.7	–17.6	6.9
MeCbl	–10.0	–11.7	1.7
CNCbl	–7.2	–5.5	–1.7

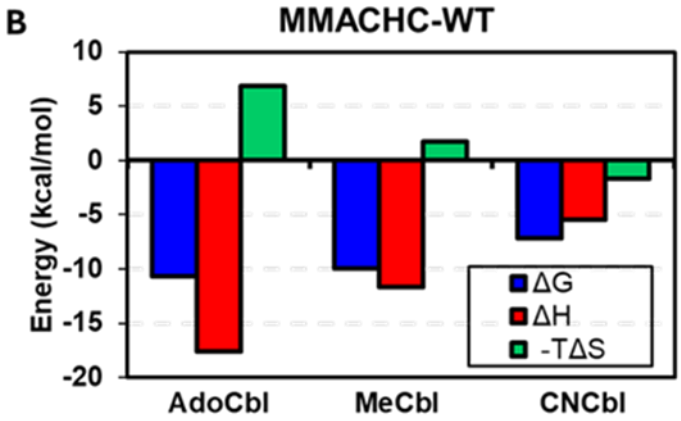

Figure 32. Thermodynamic parameters for the binding of MMACHC–WT to different cobalamins. **A.** Variations in Gibbs energy (ΔG), enthalpy (ΔH) and entropy (–TΔS), obtained by ITC experiments. Error in ΔG is 0.1 kcal/mol, and in ΔH and –TΔS is 0.4 kcal/mol. **B.** Visualization of the values reported in A

Next, we performed an ITC analysis to assess the impact of the R161Q mutation on the protein binding affinity for the various cobalamins. The obtained thermograms (Fig. 33) and the dissociation constants provided in Table 3 indicate that the R161Q mutant—despite the location of the point mutation outside of the vitamin B12 binding pocket—exhibits a decreased binding affinity for all the cobalamin variants. Cobalamin binding to the R161Q mutant follows the same affinity hierarchy as with the WT protein, according to the identical order of stabilization. However, the thermodynamic binding parameters, enthalpy and entropic contribution, reveal notable differences between the two protein variants. For every cobalamin examined, the R161Q mutation reduces the overall enthalpic contribution to binding, but partially compensates with a less-unfavorable (AdoCbl) or a more-favorable entropic contribution (MeCbl and CNCbl) (Fig. 34). This suggests that the R161Q mutation likely enhances the protein's conformational freedom, thereby increasing the entropic contribution upon cobalamin

binding, while simultaneously reducing certain favorable enthalpic interactions compared to the wild type.

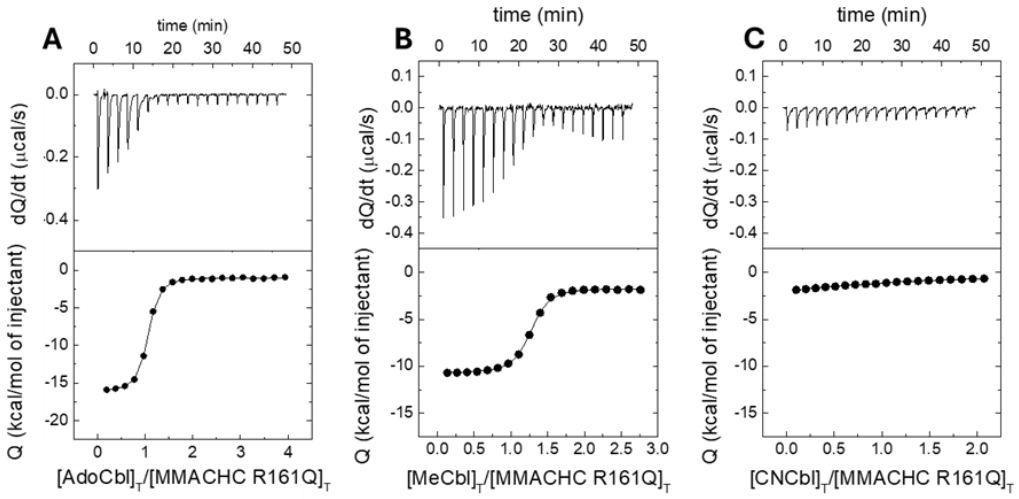

Figure 33. Calorimetric titrations for MMACHC-WT interacting with AdoCbl (**A**), MeCbl (**B**) and CNCbl (**C**). The upper plots provide the thermograms, while the lower plots display the binding isotherms fitted to a single binding site model

A

MMACHC-R161Q			
Ligand	**ΔG (kcal/mol)**	**ΔH (kcal/mol)**	**–TΔS (kcal/mol)**
AdoCbl	–9.5	–15.2	5.7
MeCbl	–9.3	–9.1	–0.2
CNCbl	–5.8	–3.4	–2.4

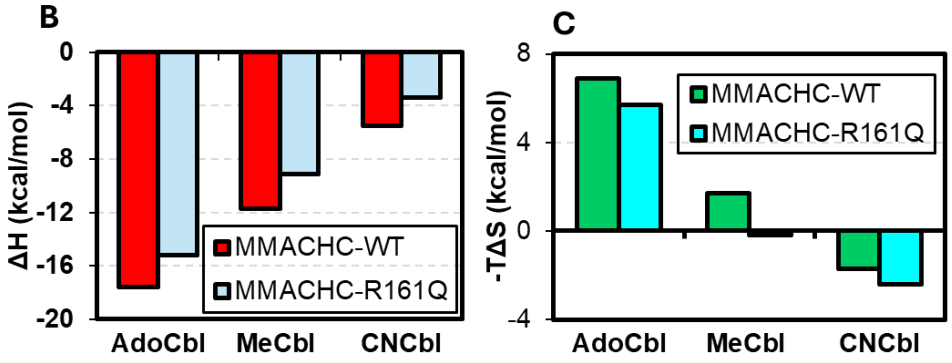

Figure 34. Thermodynamic parameters for the binding of MMACHC–R161Q to different cobalamins **A.** Variations in Gibbs energy (ΔG), enthalpy (ΔH) and entropy (–TΔS), obtained by ITC experiments. Error in ΔG is 0.1 kcal/mol, and in ΔH and –TΔS is 0.4 kcal/mol. **B.** Comparison of ΔH for MMACHC–WT and MMACHC–R161Q binding to the different cobalamins **C.** Comparison of –TΔS for MMACHC–WT and MMACHC–R161Q binding to the different cobalamins

4.5. The R161Q mutation impairs the binding to GSH

Concerning the binding to glutathione (GSH), the required cofactor for MMACHC dealkylation activity, the calorimetric experiments showed that no binding could be detected between the tripeptide and apo-MMACHC for both variants (data not shown). After verifying by absorption spectroscopy that the dealkylation rate of AdoCbl in the presence of MMACHC WT with GSH was sufficiently slow to avoid significant changes in AdoCbl concentration

during the ITC experiment (lasting approximately 1 h), we performed ITC measurements by titrating GSH into a solution of the binary complexes AdoCbl:MMACHC-WT or AdoCbl:MMACHC-R161Q. We found that while GSH was observed to interact with the complex AdoCbl:MMACHC-WT with $K_d = 2.1 \pm 0.2$ μM, no interaction could be detected between GSH and the complex AdoCbl:MMACHC-R161Q (Fig. 35).

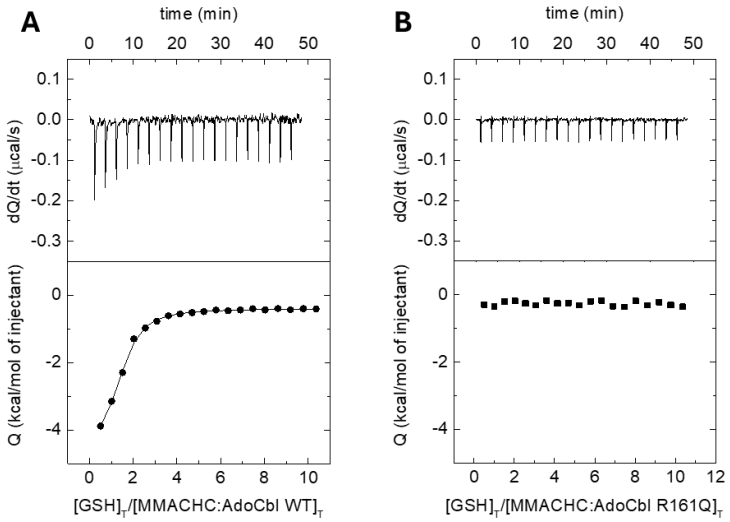

Figure 35. Calorimetric titrations for MMACHC-WT (**A**) and MMACHC-R161Q (**B**) interacting with GSH. The titrations with GSH were performed in the presence of AdoCbl, prebound to the protein in the calorimetric cell. The upper plots provide the thermograms, while the lower plots display the binding isotherms fitted to a single binding site model

Two important points follow from these ITC data: first, the structural rearrangements induced by Cbl binding to MMACHC [61] are necessary for glutathione subsequent binding. Second, these structural rearrangements induced by Cbl binding in MMACHC-R161Q do not guarantee the binding of the GSH to the protein. This was not surprising considering that arginine at position 161 is one of the residues involved in the tripeptide binding [62], [63].

A confirmation of the reduced affinity of MMACHC-R161Q for GSH also arised from MD simulation of ternary complexes (MMACHC:MeCbl:GSH) of the two proteins. We started the *in silico* investigation simulating the ternary complexes to evaluate the differences in the interaction with the natural ligand (MeCbl) and the dealkylation cofactor (GSH) for the wild type and the mutant. In Fig. 36, a clear difference in the behaviour of the GSH appears from the comparison of the RMSD between the mutant and the wild type simulations. The GSH, indeed, shows a strong instability in all the trajectories of the mutant, even going so far as to detach from the complex in the third simulation (red trace, Fig. 36B). This result is in good agreement with the ITC data, that shows no measurable binding between the GSH and the complex formed by Cbl:MMACHC-R161Q. On the contrary, MeCbl shows a strong stability during the simulations of both the mutant and the wild type (with the exception of the third

repetition of the mutant runs), also in agreement with Antony et al. [116]. This behaviour was not expected, considering the different affinity of the two proteins for the cobalamin (three-fold lower in the case of the mutant), revealed by the ITC. However, since both dissociation constants are in the nanomolar order of magnitude, it would be pretentious to expect to observe this difference in the MD simulations. Furthermore, also considering the high stability dispayed by both proteins, with RMSD values always below 3 Å (Fig. 36, green traces), we cannot exclude that the model of the mutant is biased by the presence of the cobalamin, that keeps the conformation close to the starting one, i.e. the crystallographic structure of the WT complex, while the mutant would be less available in binding the ligand.

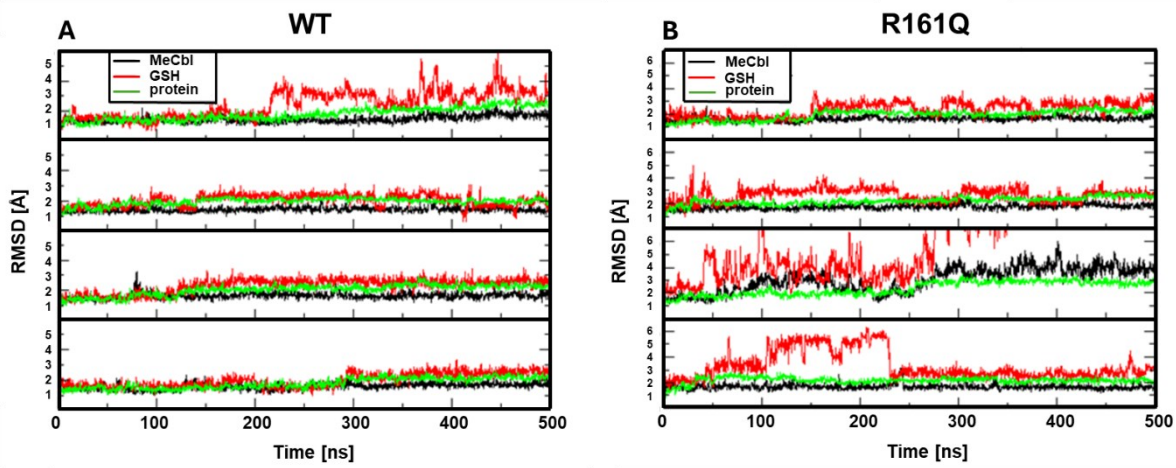

Figure 36. Time dependence of RMSD values from MMACHC-WT (**A**) and MMACHC-R161Q (**B**) simulations. Protein is shown in green, MeCbl in black and GSH in red

Nevertheless, we can observe a clear difference in hydrogen bonding between MeCbl and MMACHC-WT or MMACHC-R161Q: the analysis of the trajectories gives an average number of 6.12 hydrogen bonds for the WT and 5.3 for the mutant. In particular, the hydrogen bond between Arg132 of Pr3 and atom O4 of MeCbl is always missing in the mutant trajectories, as shown in Fig. 37, where the WT is depicted in cyan and mutant in beige.

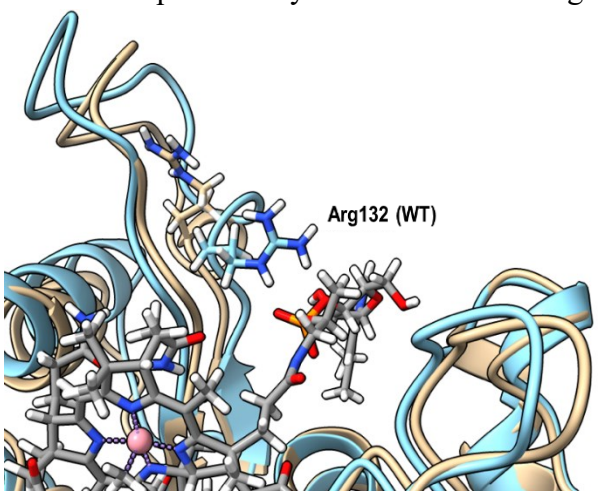

Figure 37. Hydrogen bond formed between Arg132 of MMACHC-WT (cyan) and the cobalamin tail (grey). The same bond is absent in the case of MMACHC-R161Q (beige)

The ten most populated hydrogen bonds between protein and cobalamin from the WT simulations are reported in Table 4 and compared with the occupancy measured in the mutant trajectories.

Hydrogen bond (Donor--Acceptor)	WT occupancy	R161Q occupancy
N62-COB--O-ASP104	0.69	0.48
N62-COB--O-ILE115	0.64	0.62
O7R-COB--OE1-GLN131	0.60	0.73
N29-COB--O-ILE160	0.45	0.36
N-CYS149--O34-COB	0.42	0.37
N-ILE160--O28-COB	0.42	0.21
NE-ARG132--O4-COB	0.38	X
NE2-GLN118--O34-COB	0.36	0.40
N29-COB--OD2-ASP104	0.28	0.28
OH-TYR129--O5-COB	0.25	0.19

Table 4. Comparison of the occupancy of hydrogen bonds between protein and cobalamin measured in the WT and the R161Q mutant simulations. The nomenclature of COB atoms (MeCbl) is according to S.I. of [90].

4.6. Conformational dynamics of apo MMACHC-WT and MMACHC-R161Q mutant

The obtained experimental results on the structure and stability of MMACHC-WT and MMACHC-R161Q allowed us to gain information on the different behavior of the two proteins on a molecular scale. To gain atomistic resolution, that would grant access to crucial molecular mechanisms, we would need to use experimental techniques that are not available for us at the time of this work. Instead, we resort to molecular modeling, and in particular to classical molecular dynamics [117], aiming to get insights about our system.

Moreover, simulating the apo forms looks more promising, as we do not have to account for the templating effect of the Cbl ligand observed in the simulation of the complexes. However, since we are not simulating the folding of the mutant protein, given that no 3D structure has been solved, we must hope that the most relevant conformations of MMACHC-R161Q can be achieved starting from the WT crystallographic structure.

After 1 μs of equilibrium simulation of the apo forms of the two proteins, the RMSD of the alpha carbons of the wild type, after a slight drift from the crystallographic structure at the beginning of the simulation, is stabilized around a value of 3 Å (black trace, Fig. 38). On the other hand, the mutant displays significant fluctuations in the values, that required to extend the simulation until 2 μs to detect a stabilization around 5.5 Å (red trace, Fig. 38).

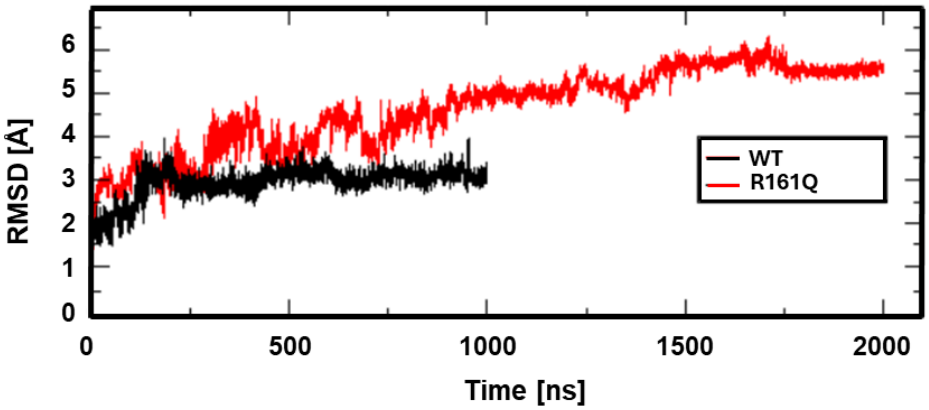

Figure 38. Time dependence of RMSD of apo MMACHC-WT (black) and MMACHC-R161Q (red)

This behaviour is also confirmed by the parallel shorter repetitions performed to enrich the sampling (all starting from the configuration at t=1 μs), whose results are shown as boxplots in Fig. 39. RMSD values for the mutant are not only higher than the WT ones, but their distribution is also larger, indicating a higher flexibility.

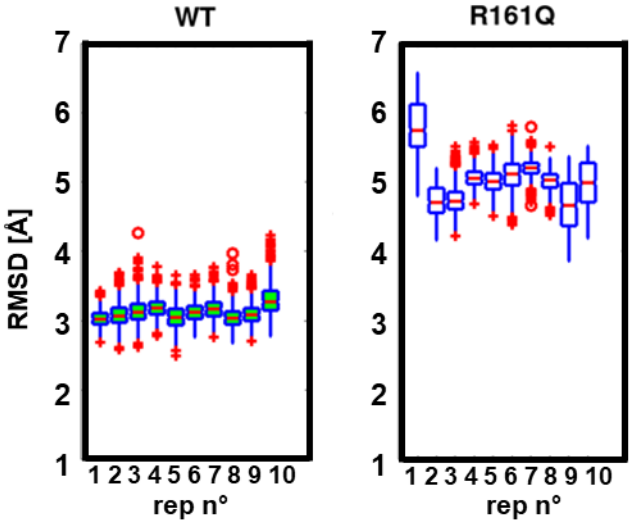

Figure 39. Distribution of RMSD after ten parallel trajectories of 300 ns each for MMACHC-WT (first panel) and MMACHC-R161Q (second panel)

The main structural difference observed between the two proteins consists in a widening of the cobalamin binding pocket of the mutant in the C-terminal region, due to the rotation of the helix HL, accompanied by the bending of the disordered Pr3 (Fig. 40, where the Cbl, not included in the simulation, is stitched in as reference).

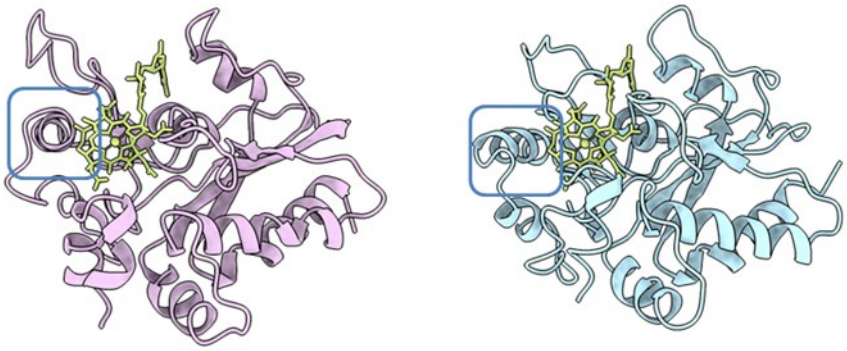

Figure 40. Superimposition of MeCbl (yellow) on the configuration at t=1 μs of wild type (pink) and mutant (cyan). Helix HL is framed by the blue box

This structural modification, observed for the mutant and not for the wild type, help to explain the difference in affinity revealed by the ITC experiments: a widening of the cobalamin pocket would reduce the number of contacts between the corrin ring of the ligand and the protein, leading to a weaker binding.

Moreover, we observed the destabilization of the protrusion Pr3, that after 1.5 μs forms a strong interaction with the protrusion Pr2, that persists until the end of the simulation (Fig. 41).

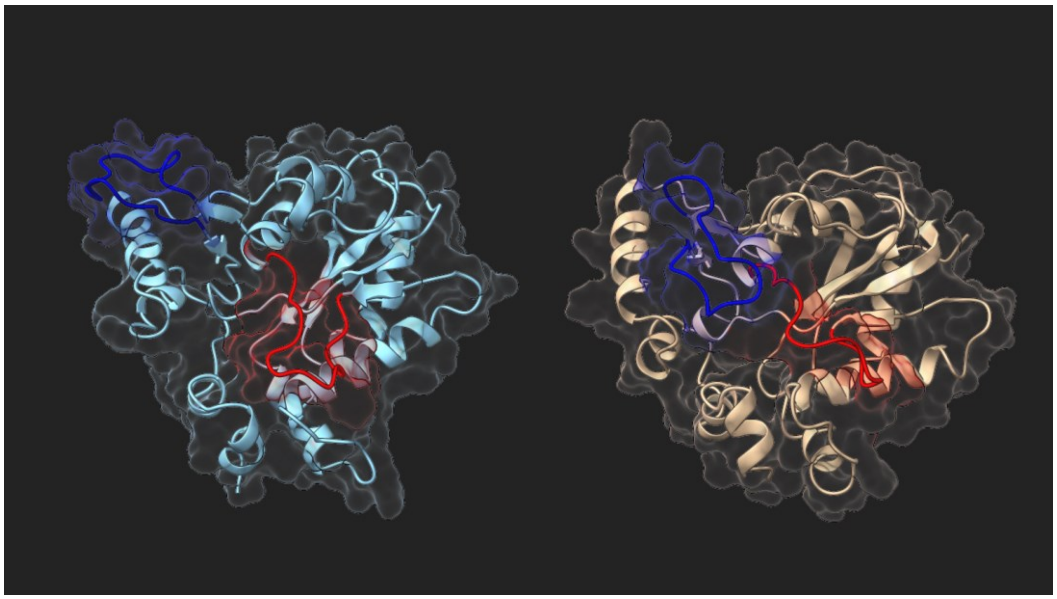

Figure 41. Snapshots from the MD simulations of MMACHC-WT (cyan, left) and MMACHC-R161Q (beige, right) showing the aberrant interaction between Pr2 (red) and Pr3 (blue) in the case of the mutant

Interestingly, the comparison between the RMSD of the structured part (i.e. residues involved in the formation of α-helices and β-strands) of the two proteins reveals a 20% increase in the case of the mutant with respect to that of the wild type, while the RMSD of the unstructured regions in the mutant is 60% higher than in the wild type (Fig. 42).

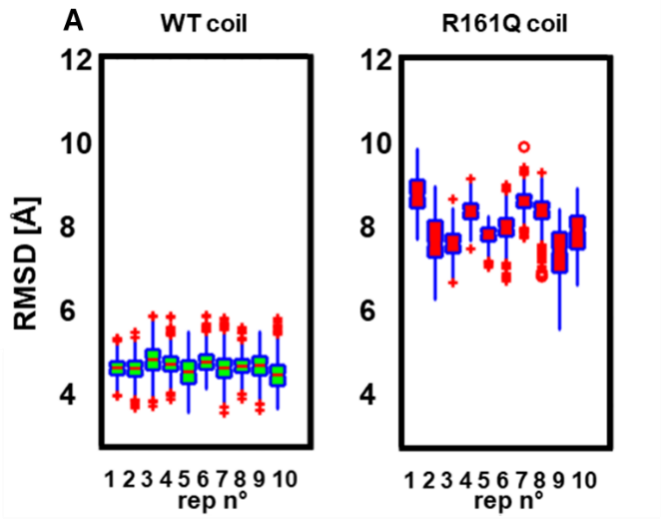

Figure 42. Distribution of RMSD of the unstuctured regions after ten parallel trajectories of 300 ns each for MMACHC-WT (first panel) and MMACHC-R161Q (second panel).

Our conclusion is that the mutation R161Q mainly destabilizes the disordered part of the protein, while its secondary structure remains similar to the wild type. In particular, the destabilization of the protrusions might have consequences on the functionality of the MMACHC, as they can obstruct the access to the binding sites of Cbl and GSH, essential cofactor for its enzymatical activity.

4.7. Impact of the R161Q mutation on protein oligomeric organization

Since we found that the R161Q mutation induces structural variations that affect the MMACHC Cbl-binding region, our next aim was to understand its role in the formation of MMACHC homodimers, supposed to result from domain swapping involving the two 5-deoxyadenosyl moieties of AdoCbl in the MMACHC subunits [62]. We assessed the assembly of the wild-type protein and R161Q mutant by using two different methodologies. First, we studied MMACHC-WT and MMACHC-R161Q oligomeric state in the absence and in the presence of AdoCbl, GSH and AdoCbl+GSH by using Blue Native-PAGE, a technique that separates multiprotein complex in a native conformation. A representative gel of five independent experiments is reported in Fig. 43A. This gel shows that both wild-type and R161Q mutant proteins predominantly exist in the monomeric state in their apo form, with only a very small amount of dimers detected more prominently in the MMACHC-WT sample (Fig. 43A, lane 2 and 6).

Similar results were obtained in the presence of GSH (Fig. 43A, lane 3 and 7). However, upon addition of AdoCbl, dimer formation significantly increased in the MMACHC-WT protein and in higher extent compared to the MMACHC-R161Q (Fig. 43A, lane 4 and 8). Additionally, a further increase in dimer population was observed only for the wild-type protein when GSH was added to the protein-Cbl complex (Fig. 43A, lane 5 and 9). Very interestingly, a band corresponding to a tetramer could be found in the MMACHC-WT sample in the presence of AdoCbl and AdoCbl+GSH, suggesting the formation of more complex hierarchical structures as also found by Froese et al. [62]. Densitometric analysis of the monomeric and oligomeric forms under various conditions revealed that the dimers/tetramers-to-monomer ratio was significantly higher for the wild-type protein compared to the R161Q mutant (Fig. 43B).

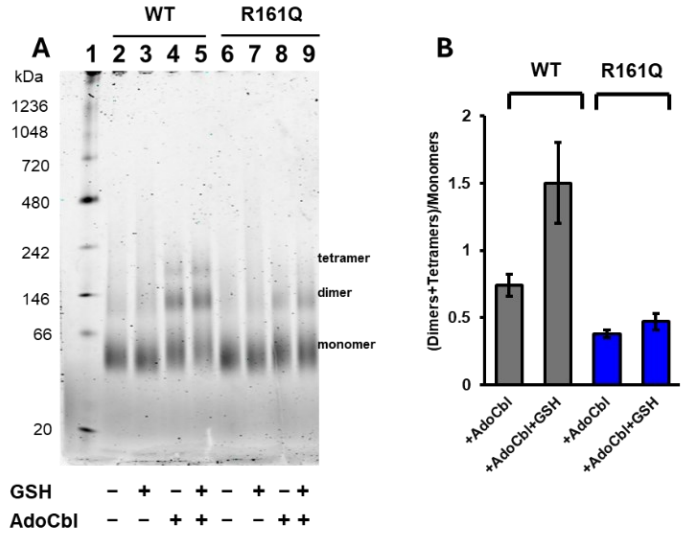

Figure 43. BN-PAGE of MMACHC-WT and MMACHC-R161Q mutant. **A.** BN-PAGE gel showing: MMACHC-WT (12 μM) or MMACHC-R161Q mutant (12 μM) protein in the absence (lanes 2 and 6) or presence of AdoCbl (120 μM) (lanes 4 and 8), or in the presence of GSH (4 mM) (lanes 3 and 7), or in the presence of GSH + AdoCbl (lanes 5 and 9). **B.** (Dimers+Tetramers)/Monomers ratio obtained from the densitometric analysis of the BN-PAGE

We confirmed the different propensity of MMACHC-WT and MMACHC-R161Q proteins to form homodimers by using SEC. In both cases, when incubated with the proteins, AdoCbl exhibits an absorption peak at 460 nm, reflecting the conformational *base-off* state achieved by vitamin B12 upon binding to the proteins (insets, Fig. 44) [53]. The chromatographic profile of the MMACHC-WT protein in the presence of AdoCbl revealed a distinct peak corresponding to its dimeric structure, whereas the MMACHC-R161Q mutant displayed only a shoulder at the same position (Fig. 44). Quantitative analysis of the peak areas corresponding to the monomeric and dimeric species indicated that, in the absence of ligands, a small amount of dimers (dimer-to-monomer ratio equal to 0.06) were formed exclusively in the apo wild-type protein, while no dimers were detected in the apo R161Q mutant. Upon addition of AdoCbl, the dimer-to-

monomer ratio increased to 0.15 in the MMACHC-WT sample, whereas it remained very low (0.03) in the R161Q mutant.

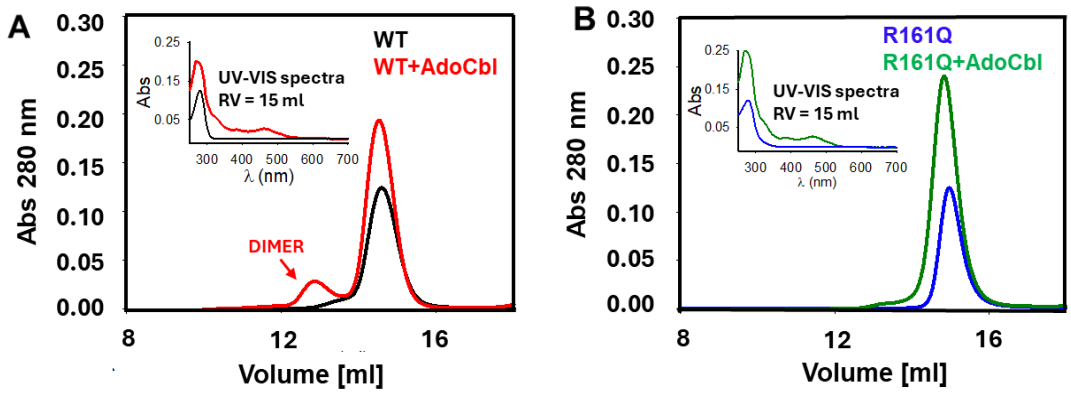

Figure 44. Chromatographic profile of MMACHC WT (15 µM) (**A**) and MMACHC R161Q mutant (15 µM) (**B**) in the absence and in the presence of AdoCbl. The insets reports the corresponding absorbance spectra relative to 15 mL retention volume (RV)

Overall, these results demonstrate that AdoCbl plays a critical role in dimer formation and that the R161Q mutant shows a significantly reduced ability to form homodimers compared to the WT. Although each technique has its specificities, the consistent results obtained across different methods probing the oligomeric state in various molecular milieu, allow us to draw these conclusions with high confidence.

Furthermore, to determine whether MeCbl and CNCbl can also promote dimer formation and whether the resulting changes in oligomeric equilibrium correlate with each cobalamin's binding affinity to the protein, we performed native gel electrophoresis experiments on MMACHC samples incubated with AdoCbl, MeCbl, or CNCbl. In addition, we examined the effect of GSH on this equilibrium. Our results confirmed that while the wild-type protein is essentially monomeric in its apo form (Fig. 45A, lane 2), a band corresponding to a dimeric structure, together with a higher-order oligomer, such as tetramers, becomes evident when the protein is incubated with all three analyzed cobalamins (lanes 3, 5, 7). We also quantified gel band intensities through a densitometric analysis, which allowed us to determine the fractions of monomers, dimers, and tetramers formed in the absence and in the presence of the various cobalamins (Fig. 45B). Our results indicated that the ability to form dimers/tetramers in the presence of each cobalamin mirrored the affinity ranking, with AdoCbl prompting more even-order oligomers, followed by MeCbl, and then CNCbl. Very interestingly, the copresence of GSH and cobalamin results in an almost invisible monomer band and a marked shift of the equilibrium toward the dimers, tetramers or even hexamers (lanes 4, 6, 8).

Also, in the case of the mutant MMACHC-R161Q, the number of dimers formed in the presence of the different cobalamins followed the same order as their affinity constants to the protein,

but dimer formation is impaired under all conditions, and no tetramers could be detected. Moreover, the presence of GSH, whose binding to MMACHC-R161Q is strongly impaired due to the disruption of the arginine 161 local environment, does not favor the shift of the oligomeric equilibrium toward even-order oligomers as observed for the WT protein.

These results again highlight the critical role of dynamic interactions between key domains involved in binding to ligands and cofactors essential for the functionality of the MMACHC protein.

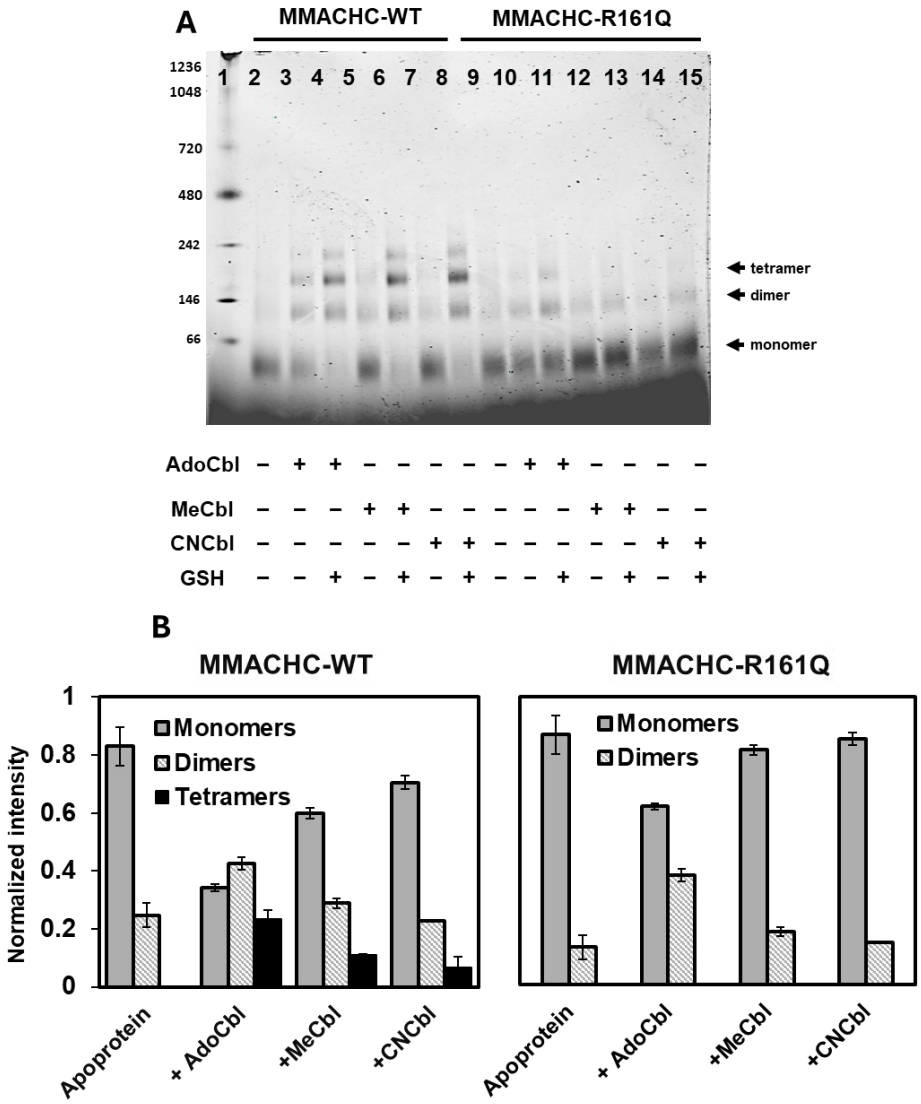

Figure 45. BN-PAGE of MMACHC-WT (12 µM) and MMACHC-R161Q mutant (12 µM). **A.** BN-PAGE gel showing: MMACHC-WT or MMACHC-R161Q mutant protein in the absence (lanes 2 and 9) or presence of AdoCbl (120 µM) (lanes 3 and 10), or in the or in the presence of GSH + AdoCbl (lanes 4 and 11), in the presence of MeCbl (120 µM) (lanes 5 and 12), or in the presence of GSH + MeCbl (lanes 6 and 13), in the presence of CNCbl (120 µM) (lanes 7 and 14), or in the presence of GSH + CNCbl (lanes 8 and 15). **B.** Band intensities from the gel, obtained via densitometric analysis and normalized by dividing each by the sum of intensities of all bands within the specific lane

4.8. MMACHC-R161Q shows an impaired enzymatic function compared to the wild type

The enzymatic ability of MMACHC to dealkylate MeCbl in the presence of GSH can be verified by UV-VIS spectroscopy, monitoring the changes in the spectrum of the cobalamin that occurs upon conversion of MeCbl into H_2OCbl. The occurrence of the reaction is revealed by two main spectral changes in the Cbl absorbance spectrum: the increase of the maximum at 353 nm together with the shift of the peak from 460 nm to 525 nm, as can be seen for the wild type in Fig. 46.

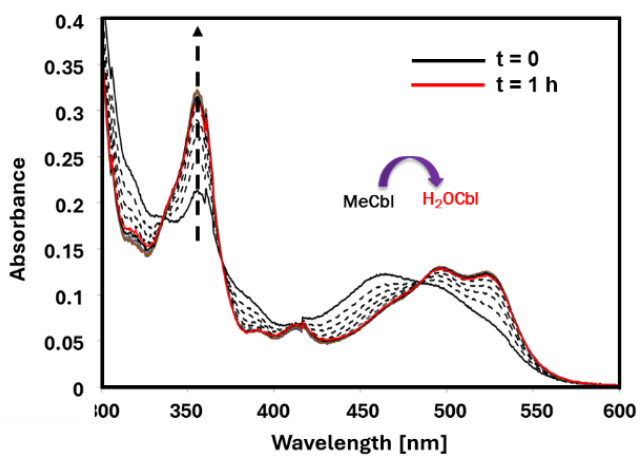

Figure 46. Conversion of MeCbl (12.8 µM) (red) in H_2OCbl (black) in time (black dashed lines) catalyzed by wild type MMACHC (16 µM) in the presence of GSH (1 mM)

By monitoring the absorbance at 353 nm as a function of time it is possible to estimate a dealkylation rate. Under our experimental conditions, the reaction catalyzed by MMACHC-WT reaches its completion within one hour. The MMACHC-R161Q mutant does bind MeCbl, as the absorption spectrum of the latter shifted from 530 nm to 460 nm, indicating its transition from the *base-on* to the *base-off* state. However, minimal changes in the Cbl absorption spectrum were observed within one hour of GSH addition, indicating that the mutant only retains a residual dealkylation functionality.

From the time dependence of the absorbance change at 353 nm (Fig. 47), the estimated dealkylation rates k_{obs} were $(38 \pm 4) \times 10^{-3}$ min^{-1} for the WT and $(2.0 \pm 0.5) \times 10^{-3}$ min^{-1} for the R161Q mutant. We conclude that, as previously assessed [62], the MMACHC-R161Q mutant is significantly less efficient than MMACHC-WT in removing the MeCbl upper ligand. This dramatic reduction is supposed to be heavily influenced by the absence of binding of GSH with the protein-Cbl complex.

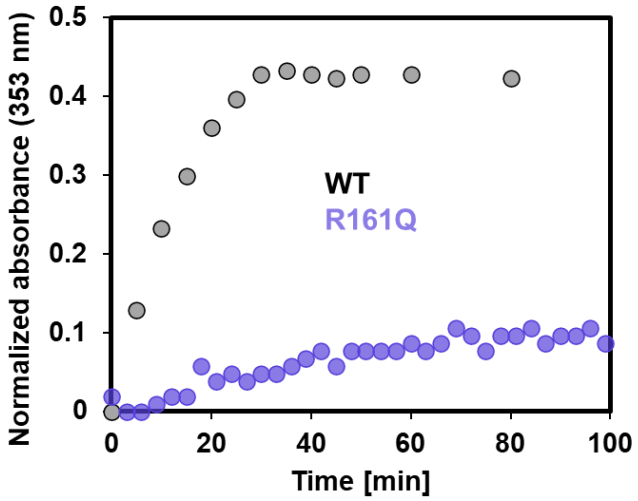

Figure 47. Dealkylation activities assessed by monitoring the time evolution of the absorbance at 353 nm of MeCbl (12.8 μM) incubated with MMACHC proteins (16 μM) after GSH (1 mM) addition. Data are expressed as the increase in absorbance at 353 nm normalized to the initial value

4.9. Role of betaine on MMACHC-R161Q stability and function

The use of chemical chaperones, osmolytes known for their ability to stabilize the protein structure, have been suggested as a potential route for rescuing the impaired activity of pathological mutants involved in rare metabolic conformational diseases [51], [118].

Given that this mutant is characterized by a significant loss-of-function, and found that its conformational stability is affected by the mutation, we decided to test the effect of different osmolytes.

In order to perform the simultaneous screening of several compounds and assess their ability to stabilize the wild-type protein and the R161Q mutant, we used a high-throughput assay detecting the kinetics of unfolding by monitoring the change in fluorescence of SYPRO Orange, a hydrophobic dye that interacts with the hydrophobic patches of the protein, that are exposed to solvent while the protein is unfolding, enhancing its fluorescence intensity [119].

To evaluate the unfolding behaviour of the proteins in the presence of the different osmolytes, we used an isothermal denaturation procedure and registered the time evolution of the dye fluorescence emission at 586 nm upon excitation at 490 nm at the fixed temperature of 38 °C.

The time dependence shows that the isothermal denaturation progresses as multistep process with the presence of different species, each one with a particular affinity for SYPRO orange and a particular contribution to the observed signal. Hence, the dissimilarity in the shape of the denaturation curves between the WT and the mutant (Fig. 48) can be ascribed to the distinct conformational populations shown by the two proteins [120].

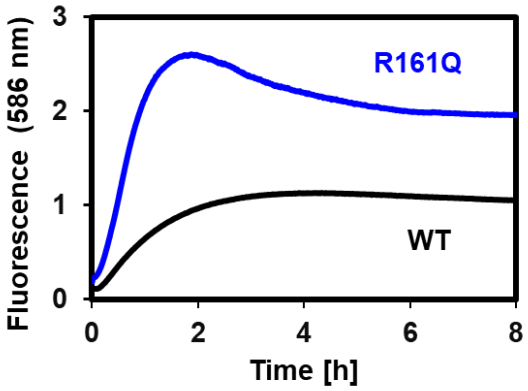

Figure 48. Time dependence of SYPRO Orange fluorescence emission at 586 nm upon excitation at 490 nm at the fixed temperature of 38 °C incubated with MMACHC-WT (3 μM) and MMACHC-R161Q mutant (3 μM)

As a next step we performed isothermal denaturation experiments of the proteins by using SYPRO orange in the presence of arginine, proline, betaine and trehalose (Fig. 49).

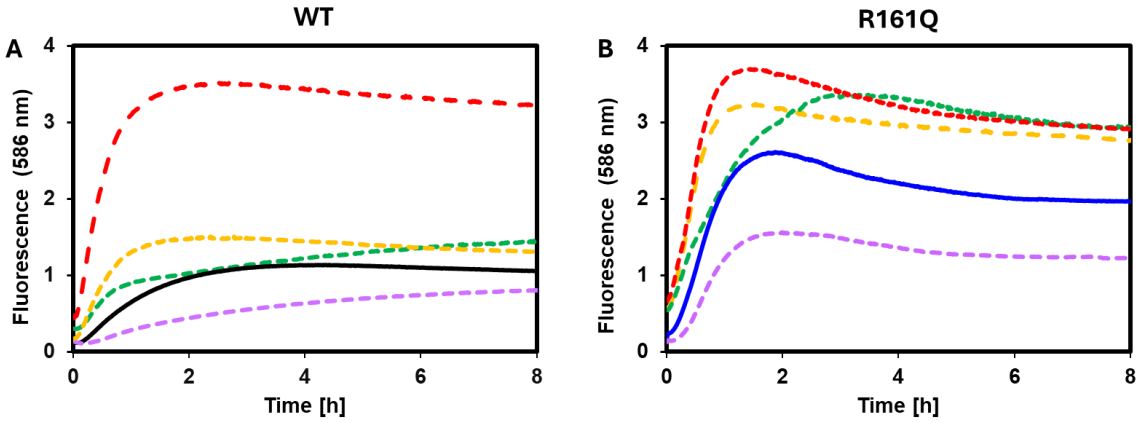

Figure 49. Time dependence of SYPRO Orange fluorescence emission at 586 nm upon excitation at 490 nm at of 38 °C incubated with MMACHC-WT (3 μM) (**A**) and MMACHC-R161Q mutant (3 μM) (**B**) in the absence (continuous black for wild type and continuous blue for R161Q mutant) and in the presence of several chemical chaperones (0.5 M) arginine (dashed red), proline (dashed yellow), trehalose (dashed green), betaine (dashed purple)

We found that only betaine was effective in reducing both the plateau and the initial slope of the denaturation curves (Fig. 45, purple dashed lines). This indicates an enhanced stabilization effect exerted by betaine on both MMACHC-WT and MMACHC-R161Q protein.

Of note, betaine is already employed therapeutically in *cblC* disease [121], primarily as a methyl donor to convert homocysteine into methionine, thereby lowering plasma total homocysteine levels in homocystinuria patients. Our results indicate that betaine can also

stabilize a MMACHC mutant protein associated with *cblC* disease, suggesting a potential chaperone-like activity.

To validate the protective effect of betaine, identified as the only effective compound in previous experiments, against MMACHC denaturation, and to exclude any bias from the extrinsic dye, we used CD spectroscopy to assess the thermal unfolding process exclusively for this osmolyte (Fig. 50). Once again, we confirmed the role of betaine in stabilizing both the wild-type protein and the R161Q mutant as also shown by the increase of unfolding temperatures induced by the presence of the osmolyte.

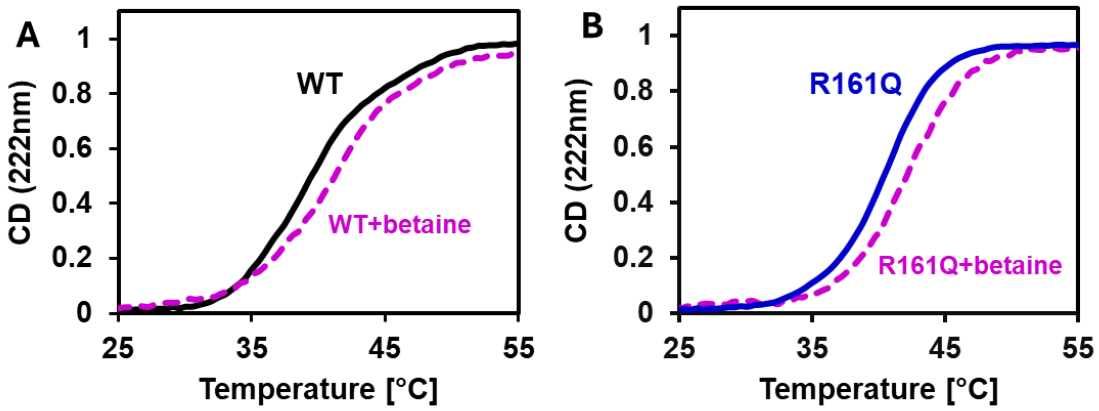

Figure 50. Thermal unfolding curves obtained by monitoring ellipticity at 222 nm as a function of the temperature for MMACHC-WT (10 µM) (**A**) and MMACHC-R161Q mutant (10 µM) (**B**) in the absence and in the presence of 0.5 M of betaine. The ellipticity values have been normalized for appropriate comparison

Hence, we wanted to understand whether betaine could also have a role in improving the dealkylation activity of MMACHC-R161Q.

Interestingly, when we repeated the dealkylation test for the MMACHC-R161Q mutant in the presence of betaine, we observed a partial recovery in protein function (Fig. 51), with a k_{obs} estimated by the absorbance variation at 353 nm equal to $(6.6 \pm 0.7) \times 10^{-3}$ min^{-1}, thus 60% higher than that measured in the absence of the osmolyte. Although we did not expect a complete recovery, given that the MMACHC-R161Q function is significantly impaired by its reduced binding to GSH in addition to overall destabilization, it appears that betaine can partially restore protein functionality. This result helps to elucidate the role of structural stabilization in designing therapeutic strategies for *cblC*.

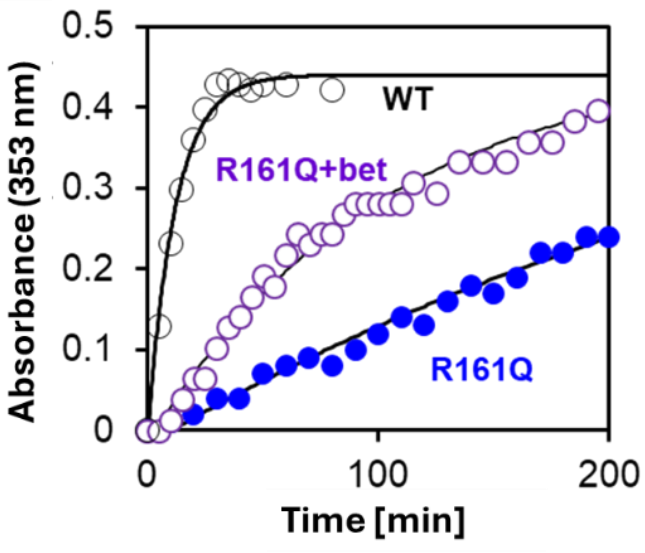

Figure 51. Dealkylation activities assessed by monitoring the time evolution of the absorbance at 353 nm of MeCbl (12.8 µM) incubated with MMACHC proteins (16 µM) after GSH (1 mM) addition. Data are expressed as the increase in absorbance at 353 nm normalized to the initial value. Continuous lines represent single-exponential fits to the experimental data obtained for MMACHC-WT, and MMACHC-R161Q in the absence and presence of 0.5 M betaine

4.*10. Therapeutic approaches for cblC disease: current treatments and experimental strategies*

The cblC disease, as many genetic disorders, is an orphan disease that remains without a definitive cure. Current therapy relies on hydroxocobalamin (OHCbl) supplementation, which partially restores metabolic functions but does not stop the progression of the disease. However, the response to treatment is highly variable among patients, depending on the nature of the underlying mutation. In this context, part of this research was aimed to identify small safe molecules capable of specifically binding, stabilizying and ultimately restoring the function of the MMACHC missense pathological proteins. To achieve this, we relied on molecular docking using two complementary approaches: the first involves the evaluation of the interaction of candidate molecules with the wild-type dimer, while the second focuses directly on the R161Q mutant form to assess the specificity of potential correctors. Last, since the use of translational readthrough-inducing drugs (TRIDs) could represent a viable strategy to restore full-length protein expression in nonsense variants, we generated a reporter system that could be used to transfect cellular models to test their effect.

4.10.1. Studies to investigate current cblC therapies: effects of OHCbl

Currently, hydroxocobalamin (OHCbl) is the only cobalamin used in the therapeutic treatment of the *cblC* disease [44]. When we assessed the thermal denaturation of MMACHC-R161Q mutant in its presence, we noticed that this cobalamin induces a different profile compared to

the others (Fig. 52, solid blue line), consisting in a more stretched unfolding curve. The fitting of the curve revealed the need of a two-transition model to interpolate these data, as for the wild type, instead of the single transition model used for all the other curves. This is an interesting result, that could help to explain the efficacy of OHCbl in the therapy, and the lack of clinical effect of the other forms of cobalamin: it is possible that the OHCbl induces the mutant to assume *a wild type-like* conformation, thus improving its functionality. These findings provide a molecular rationale for the clinical efficacy of hydroxocobalamin, and could have potential implications for the development of therapeutic strategies based on substrate replacement.

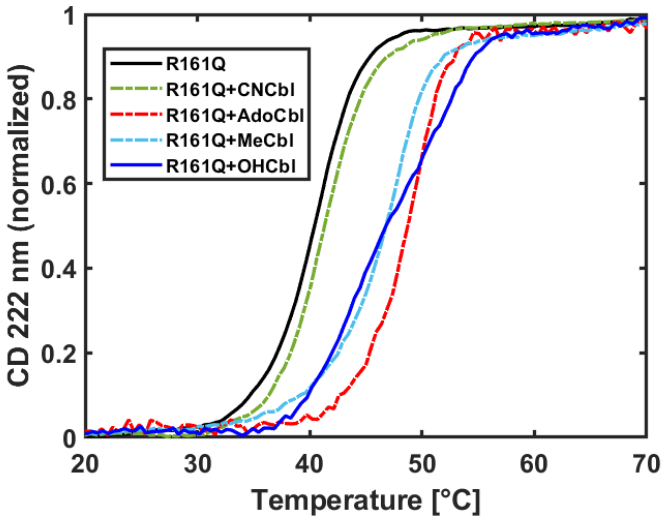

Figure 52. Denaturation profiles of MMACHC-R161Q (10 μM) in the presence of all the cobalamin tested (20 μM) monitored by circular dichroism. The ellipticity values have been normalized for appropriate comparison

4.10.2. Effect of small molecules from docking on the MMACHC-WT dimer

The stabilization of the MMACHC-R161Q mutant induced by betaine, which resulted in an improvement of its functionality, serves as a proof-of-concept that structural stabilization may represent a viable therapeutic strategy for the treatment of missense mutations causing *cblC* disease. Since betaine acts as a non-specific stabilizer, we focused our research in identifying compounds that could act as pharmacological chaperones, small molecules able to specifically bind to the mutant protein, stabilize it, and ultimately enhancing its enzymatic activity [47]. This approach is already being successfully applied in the treatment of other rare disorders caused by conformational defects.

Based on the available crystallographic structure of the protein dimer (PDBID: 3SOM), researchers from IBF-CNR Milan identified a pocket at the interface between two protomers. Then, by using the software autodock4, this site was targeted with a virtual library of *drug-like* molecules (https://www.chembridge.com), that were ranked based on their docking score).

The 11 best ranked molecules (Fig. 53) were selected to test their effect on MMACHC-R161Q in our laboratories.

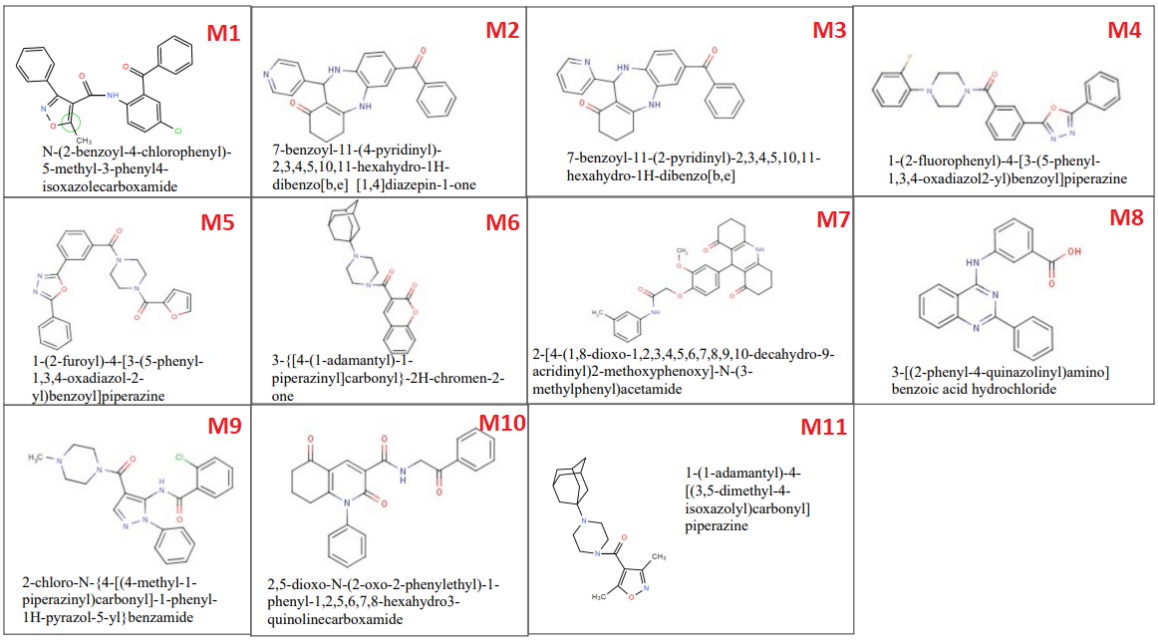

Figure 53. Chemical structures of the best ranked molecules from docking on the MMACHC dimeric structure

Among these, molecule 3 (M3) and molecule 6 (M6), showed a moderate affinity to MMACHC-R161Q, with a Kd respectively of 1.27 ± 0.08 μM and 11.4 ± 0.34 μM, obtained by ITC. However, the apparent stoichiometry obtained from the fitting of the binding isotherms is equal to 1 for both the molecules, meaning that one molecule is bound to one monomer, so the binding site cannot be the pocket explored by the docking. This is not surprising considering that the mutant is less able to form homodimers, and that the dimerization happens only in the presence of cobalamins, while the molecules were tested with the protein in the apo form.

The thermodynamic parameters obtained from the fitting of the ITC binding isotherms (reported in Table 5) for the two molecules showed that while M3 presents a higher affinity, its binding is entropically-driven; instead, M6 present a lower affinity but with an enthalpically-driven binding.

	ΔG (kcal/mol)	**ΔH** (kcal/mol)	**− TΔS** (kcal/mol)
M3	−8.04	−1.21	−6.83
M6	−6.74	−4.81	−1.93

Table 5. Thermodynamic parameters obtained for the binding of MMACHC–R161Q to M3 and M6

The next step was to assess the stability of the mutant in the presence of the two molecules, and both M3 and M6 showed a stabilizing effect on the protein structure (Fig. 54A). However, the

dealkylation assay performed in the presence of the molecules did not show any improvement in the mutant functionality (Fig. 54B).

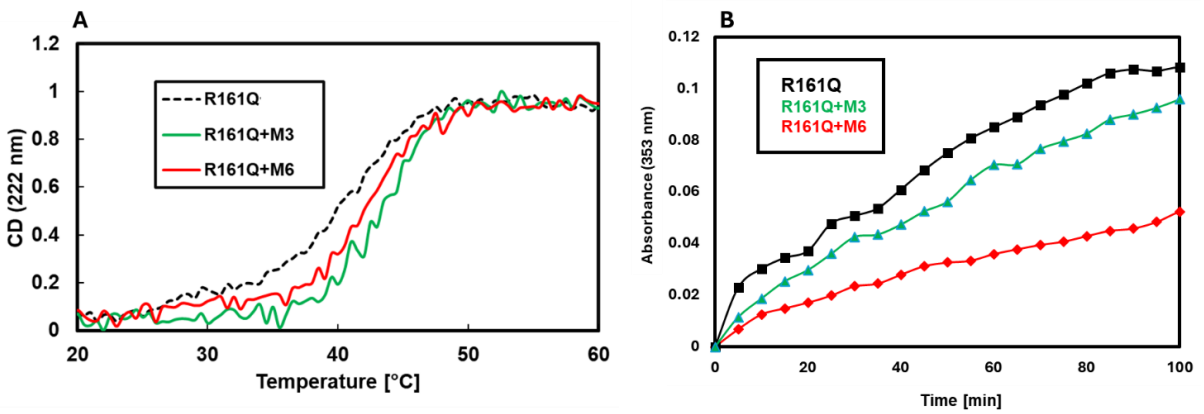

Figure 54. Effects of M3 and M6 on MMACHC-R161Q in a molar ratio protein-to-molecule 1:1. **A.** Thermal denaturation obtained monitoring ellipticity values changes at 222 nm. **B.** Dealkylation activity assessed by monitoring the time evolution of the absorbance at 353 nm of MeCbl (12.8 μM) incubated with MMACHC-R161Q (16 μM) after GSH (1 mM) addition in the absence and in the presence of M3 (16 μM) or M6 (16 μM).

4.10.3. Molecular docking on the MMACHC-R161Q mutant monomer

Considering the weaknesses of the model discussed in the previous paragraph, we decided to perform a different docking calculation starting from the monomeric structure of the MMACHCH-R161Q mutant, in complex with GSH and MeCbl. Since no druggable pocket of the protein is known in literature, we decided to explore the protein's surface using Maestro SiteMap to identify putative binding sites and evaluate their druggability. The tool provides a score characterizing the binding site in terms of size, degrees of enclosure by the protein and exposure to solvent, hydrophobicity and hydrophilicity and tendency to form hydrogen bonds [107]. The first map obtained, located between the GSH and the Cbl binding pockets (Fig. 55) was used to perform a virtual screening of the DrugBank Database and FDA-approved drugs library. The molecules were ordered on the basis of the obtained docking score.

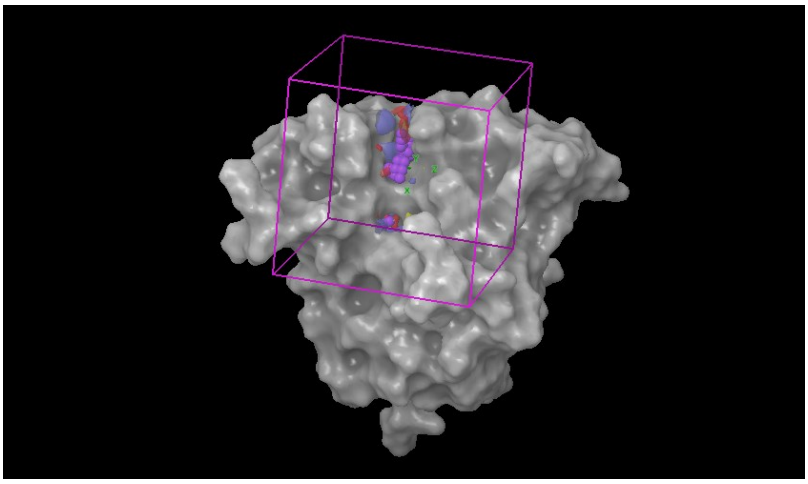

Figure 55. Grid generated on the map obtained by Site Map (surface of the protein shown)

The best ranked molecules (Fig. 56) were selected to be experimentally tested.

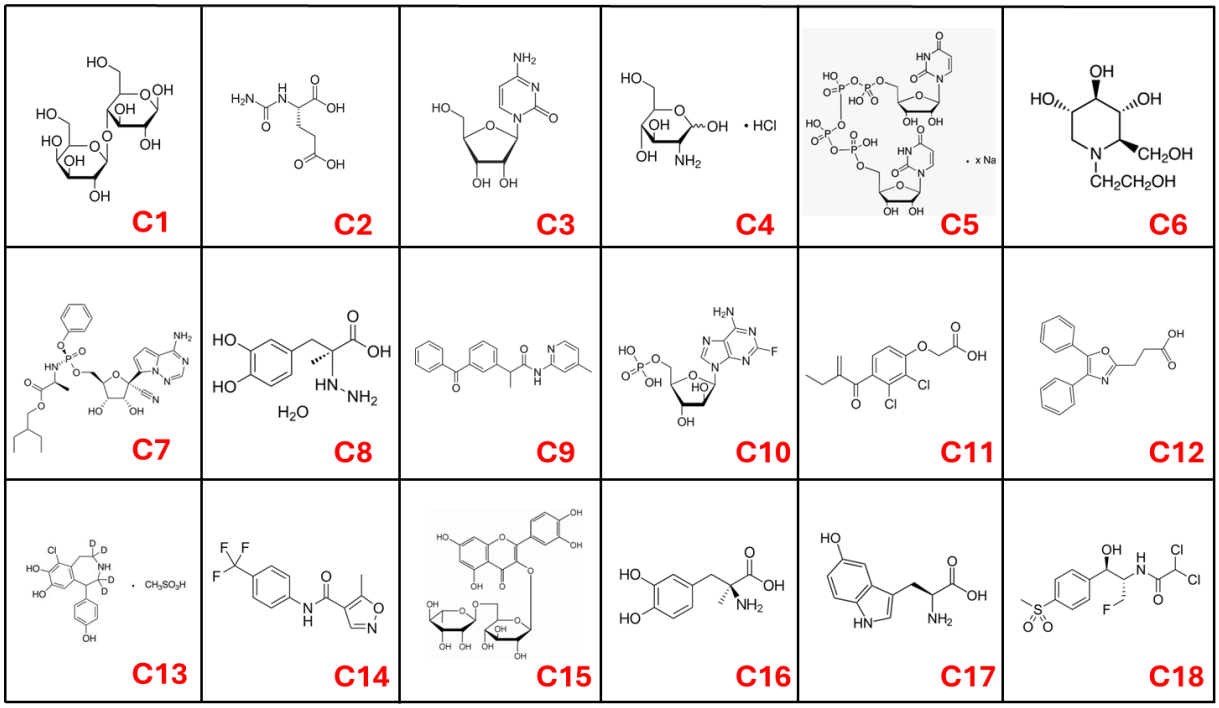

Figure 56. Chemical structures of the best ranked molecules from docking on the MMACHC monomeric structure

Preliminar high-throughput differential scanning fluorimetry using SYPRO Orange as reporter, performed in the presence of a fiftyfold molar excess of compounds C1 to C18, showed no stabilization effect exerted by any molecule, with the exception of rutin (quercetin-3-O-rutinoside, C15).

Very interestingly, the affinity of the R161Q mutant for this molecule was previously tested by ITC, giving a Kd = 4.27 ± 1.42 μM. With a ΔG = −7.3 kcal/mol, a ΔH = −4.7 kcal/mol and −TΔS= −2.6 kcal/mol, the interaction results enthalpically-driven.

However, the enzymatic functionality of the mutant in the presence of rutin was not significantly improved (Fig. 57).

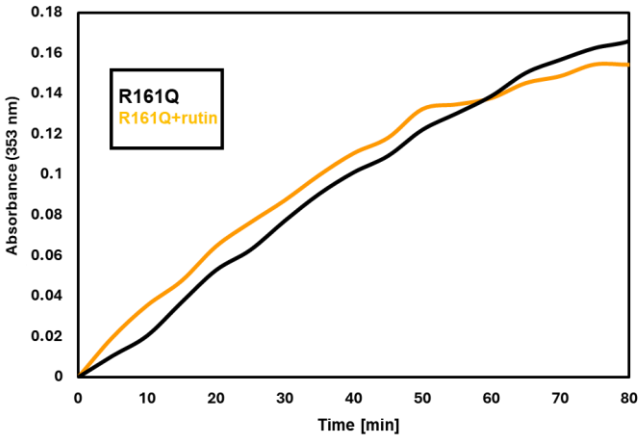

Figure 57. Dealkylation activitiy assessed by monitoring the time evolution of the absorbance at 353 nm of MeCbl (12.8 µM) incubated with MMACHC-R161Q (16 µM) after GSH (1 mM) addition in the absence and in the presence of a rutin (16 µM). Data are expressed as the increase in absorbance at 353 nm normalized to the initial value

4.10.4. Generation of the reporter system for testing TRIDs

Considering the high incidence of nonsense mutations in *cblC* disease, we suggest that these genotypes could benefit from treatment with TRIDs. However, the effect of these molecules must be evaluated in suitable cellular models, which is currently beyond our experise. Thus, to this end, we enstablished a collaboration with Prof. Laura Lentini's laboratory to deal with the cells. On our side, we constructed a reporter system in which MMACHC-WT was fused *in-frame* with GFP as control, from which MMACHC-R132X-GFP and MMACHC-Y222X-GFP were obtained.

We chose p-EGFP-N1 (4.7 kb) as vector, a plasmid that encodes a variant of green fluorescent protein (GFP) which has been optimized for brighter fluorescence and higher expression in mammalian cells.

The first step was to select a couple of restriction ezymes that were able to cut the multicloning site of the vector (Fig. 58), generating oriented ends (sticky-sticky or sticky-blunt). We selected the couple EcoRI and SmaI.

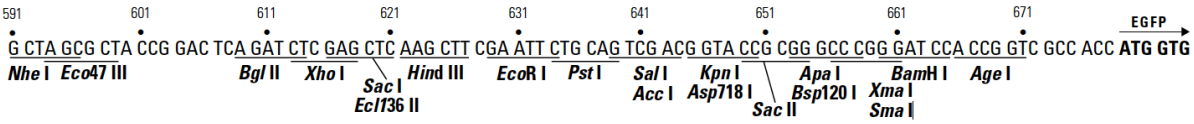

Figure 58. Multicloning site of p-EGFP-N1

Next we designed the primers to amplify the DNA sequence coding for MMACHC-WT protein (940 bp) without the stop codon, a mandatory step to ensure the expression of the protein fused

with the GFP at the C-terminal end. The primers were engineered to include an EcoRI restriction site at the 5' end and a SmaI site at the 3' end.

Cutting both the vector and the insert with the same restriction enzymes guarantees the formation of complementary ends, that can be ligated by a DNA ligase, generating a plasmid encoding for MMACHC-GFP. The successful insertion was verified by cutting the construct with EcoRI and SmaI to visualize the release of a DNA fragment of the correct size by agarose gel electrophoresis (Fig. 59, lane 1 and 5) and the correct formation of the open reading frame were verified by Sanger sequencing.

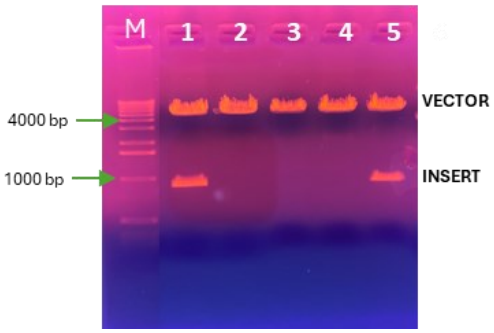

Figure 59. Agarose gel showing positive clones (lane 1 and 5) of pEGFP-N1-MMACHC-WT

From this construct, we introduced by site-directed mutagenesis the point mutation c.394C>T for introducing the opal codon TGA, giving the R132X variant, and c.666C>A for introducing the ochre codon TAA, giving the Y222X variant.

These plasmids were used in Professor Laura Lentini's laboratory to successfully transfect HCT116 human cell line and assess the efficacy of TRIDs. Briefly, cells transfected with pEGFP-N1-MMACHC-R132X or pEGFP-N1-MMACHC-Y222X do not display fluorescence, as the nonsense mutation occurs upstream of the GFP coding sequence. Consequently, only truncated MMACHC proteins are produced, lacking the GFP. Upon treatment with TRIDs, the detection of green fluorescent cells indicates that the tested TRIDs promote PTC readthrough, enabling the translation of the full-length MMACHC–GFP fusion protein.

4.11. Investigation on other MMACHC pathological missense mutants

As mentioned in the first paragraph of this section, four missense mutants, predicted to be destabilized by the pathological mutation, were initially selected for the assessment of their solubility when expressed as recombinant proteins. Three of these variants (MMACHC-G147A, MMACHC-Y130C, and MMACHC-R206) resulted exclusively localized in the inclusion bodies of the bacterial pellet. Among them, MMACHC-G147A was chosen for further

optimization attempts of recovery, as this mutation was considered relatively mild, given that the affected residue does not seem involved in key interactions and that the substitution of a glycine into an alanine only introduces a methyl group. Several attempts were made to extract this mutant as recombinant his-tagged protein from *E. coli*, but none of them was successful. Both denaturing and non-denaturing extraction attempts were made in order to recover the protein. After verifying by SDS-PAGE that the protein is expressed in *E.coli* BL21(DE3) but present exclusively in the insoluble fraction (Fig. 23), it was extracted from inclusion bodies under denaturing conditions, by using a buffer containing 8 M urea. After IMAC, an attempt of in column refolding was made trying to remove the urea with a linear gradient, but no protein was recovered. Gradual removal of the urea by dialysis in different conditions was also tried, but always ended in protein precipitation. Use of N-lauroyl sarcosine as mild solubilizing agent is suggested in the literature [122], but the concentration required (0.3% w/v) was denaturing for the protein and did not help to obtain the protein in solution. Change in the *E. coli* strain to Rosetta 2 (DE3) was also accompanied by performing an osmotic shock with NaCl before the induction of the expression of the recombinant protein to cause accumulation of betaine, supplemented in the medium, in the bacteria, to help the correct protein folding [123]. In this case, we were able to extract the protein as a monomer, according to the chromatogram profile, for the first time, but very low in concentration (0.03 mg/ml). When we tried to concentrate the fractions to 0.1 mg/ml, the protein formed visible aggregates.

The last condition was also applied to the purification of MMACHC-R206P and MMACHC-Y130C, but it always ended in protein precipitation. We conclude that these mutants are not soluble as recombinant proteins.

In the absence of an experimental system, to gain more insights on the behaviour of the MMACHC-G147A mutant we relied on Molecular Dynamics. The simulation of the MMACHC-G147A protein shows a progressive closure of the cobalamin binding pocket, mainly driven by the destabilization of the disordered protusion Pr3 and helix HI, until the complete disruption of the site. The C-alpha RMSD of the mutant protein after equilibration sits around 6 Å (Fig. 60A), with a significant contribution to the conformational change of both the structured (Fig. 60B) and the unstructured part (Fig. 60C) of the peptide chain.

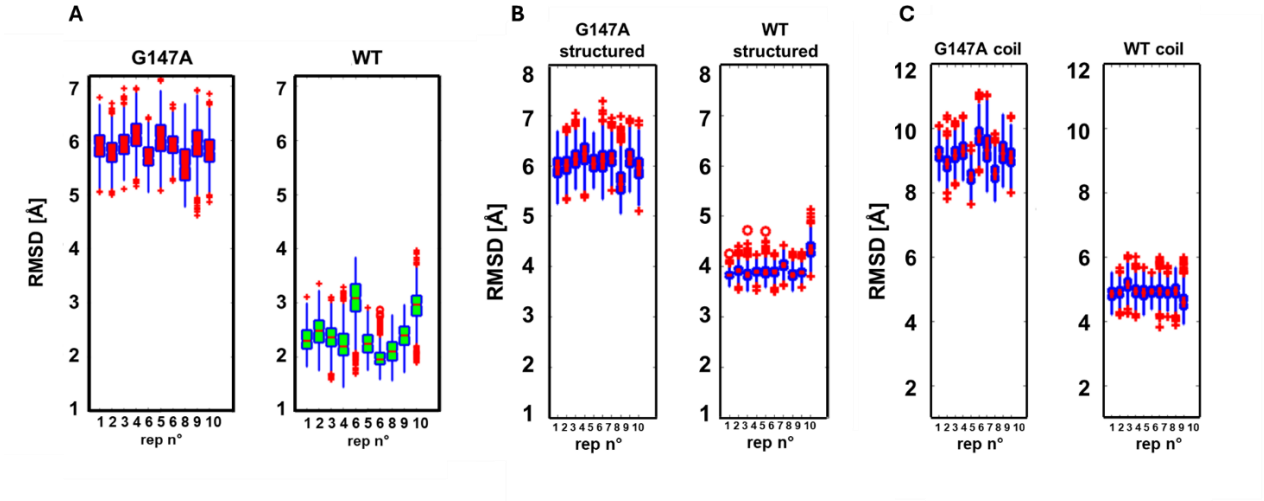

Figure 60. Distribution of RMSD after ten parallel trajectories of 300 ns each for MMACHC-G147A (left panels) and MMACHC-WT (right panels). **A.** RMSD of the protein backbone. **B.** RMSD of the structured part of the proteins. **C.** RMSD of the unstructured pat of the proteins

The preferred misfolded configuration (Fig. 59) adopted in the simulations can help to explain our difficulties in producing this mutant as a soluble protein.

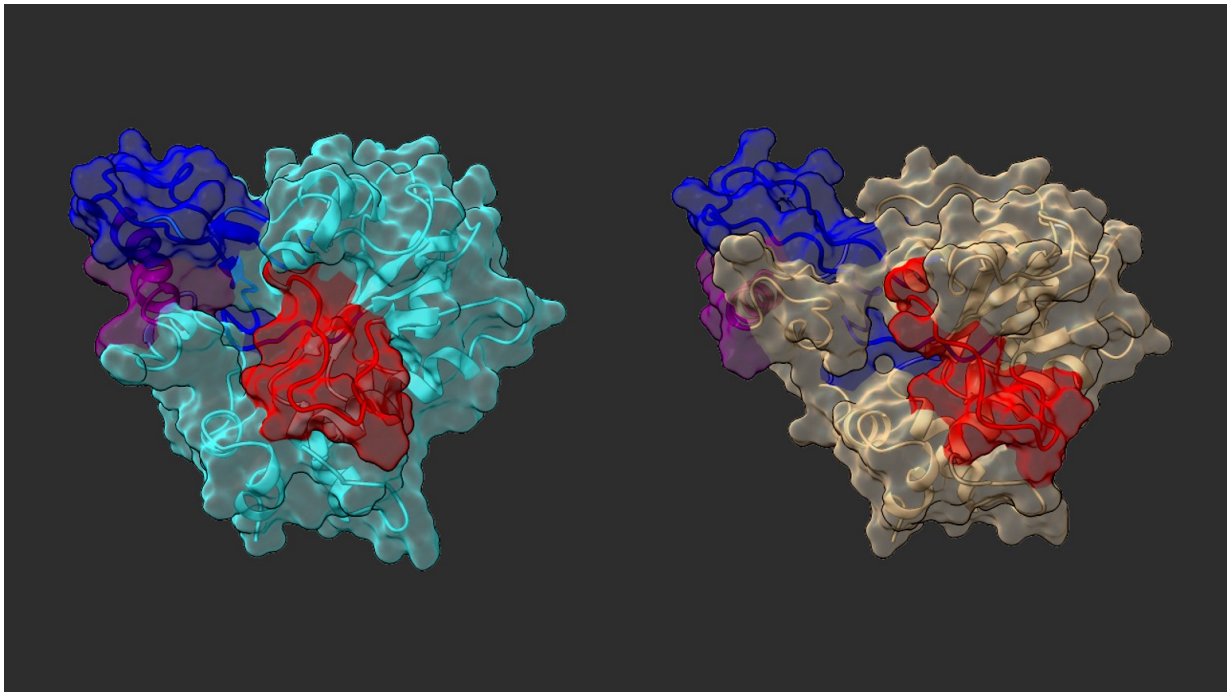

Figure 61. Snapshots from the MD simulations of MMACHC-WT (cyan, left) and MMACHC-G147A (beige, right) showing the disruption of the cobalamin binding site in the case of the mutant. For reference, Pr2 is colored in blue, helix HI in purple and Pr3 in red

5. Discussion

The *cblC* disease is a rare metabolic disorder that mainly affects children during early childhood, often leading to severe neurological and cardiovascular complications. It is caused by mutations in the gene encoding MMACHC, an enzyme that plays a crucial role in binding and removing the upper ligand of vitamin B12. This reaction requires specific cofactors, such as glutathione (GSH), which participates in the dealkylation activity of the enzyme.

The main aim of this PhD research was to compare the properties of the wild-type MMACHC protein with those of pathological variants, in order to identify the structural and physicochemical alterations underlying the disease. This comparative approach also provided the opportunity to investigate previously unexplored biophysical aspects of the wild-type enzyme, thereby deepening our understanding of the molecular mechanisms responsible for MMACHC function and dysfunction. This knowledge represented a crucial step toward the identification of strategies capable of correcting the physicochemical defects associated with the pathological variants, paving the way for potential therapeutic interventions.

Accordingly, our investigation primarily focused on the common c.482G>A point mutation, which gives rise to the MMACHC-R161Q variant, in which arginine is replaced by glutamine in position 161.

Although the c.271dupA frameshift mutation in the *MMACHC* gene is the most prevalent genetic alteration in *cblC* disease, around 10% of patients carrying this mutation on one allele also harbour a missense variant on the other. To date, more than 30 missense mutations have been identified, most of which are linked to later-onset symptoms [41], [42]. Hence, unlike c.271dupA, which dramatically reduces protein levels, these missense mutations are often associated with a reduced function of the expressed protein. Investigating these variants provides key insights into the relationship between genetic mutations and protein dysfunction leading to pathology [41].

The research on this thesis focused on the effect of the most frequent point mutation, c.482G>A, on the structure, stability, dimerization propensity, and binding properties of the resulting MMACHC-R161Q protein, proven by Gherasim et al. to be strongly impaired in the ability to catalyze the transformation of MeCbl to H_2OCbl in the presence of GSH [54]. In good

agreement with these results, we found, by using absorption spectroscopy, that MMACHC-R161Q, produced as soluble protein in our laboratories, presented an estimated dealkylation rate 16-fold lower compared to MMACHC-WT (Fig. 47). This allowed to conclude that, as previously assessed [54], the R161Q mutant is significantly less efficient in facilitating the removal of the MeCbl upper ligand. This result is not surprising since the mutation affects the arginine residue in position 161 belonging to the cluster of arginines which, through specific hydrogen bonds and ionic interactions, determines binding to MMACHC of GSH [62], an essential cofactor for the dealkylation functionality.

Within this PhD research thesis, for the first time, the binding of glutathione to MMACHC (WT or R161Q) complexed with a form of cobalamin, was quantitatively measured using ITC. The results show that while no binding of GSH to MMACHC-WT apoprotein was detected, a micromolar affinity was observed between the tripeptide and the wild type when complexed with AdoCbl (Fig. 35A). This suggests that cobalamin induces a conformational change in MMACHC, shifting the conformational equilibrium towards a GSH binding-competent conformation, allosterically modifying the GSH binding site, and enhancing its affinity for the tripeptide. In contrast, no binding was observed between GSH and the MMACHC-R161Q mutant, neither in the absence nor in the presence of AdoCbl (Fig. 35B). This result was also corroborated by the Molecular Dynamics simulations, that showed a significant instability of GSH when complexed to the mutant bound to the cobalamin (Fig. 36B). Indeed, while the arginine-to-glutamine substitution directly disrupts local interactions with negatively charged molecules such as GSH, we cannot exclude the possibility that the reduced ability to bind GSH results from an impairment of the cobalamin-induced allosteric conformational change in the R161Q mutant. Actually, the MD simulation of the MMACHC-WT complex showed that the occupancy of the bond between Arg161 and GSH is a mere 20%, suggesting a limited importance of this single direct interaction.

In fact, when we measured the binding affinity of AdoCbl to both proteins using ITC, we found that AdoCbl displayed a 7-fold reduction in affinity for MMACHC-R161Q compared to the wild-type protein (Table 3). This finding supports the idea of a functional interplay between cobalamin and GSH binding, which is likely important for MMACHC's role in vitamin B12 metabolism. Moreover, since MMACHC is expected to physiologically bind whatever form of cobalamin it encounters, we also directly assessed the binding affinity of the two MMACHC variants to MeCbl and CNCbl, obtaining a 3-fold and 10-fold reduced affinity of the mutant respectively (Table 3). While earlier studies could only infer vitamin B12 affinity indirectly, often by observing how ligand addition shifted protein stability [52] or by monitoring changes

in intrinsic fluorescence upon incremental ligand addition [53], within this PhD research project, by measuring the heat released during the titration of the ligands into the protein solution, we directly obtained the binding isotherms for AdoCbl, MeCbl and CNCbl binding to MMACHC, yielding for the first time K_d values, together with the complete thermodynamic binding profile (Gibbs energy, enthalpy, and entropy of binding).

These measurements allowed us to correlate binding affinity with the stabilizing effect of different forms of the vitamin, which was assessed using a dye-free spectroscopic technique such as CD (Fig. 29A). The order of stabilization found for MMACHC-WT mirrored the affinity rank, with AdoCbl being the most stabilizing ligand with the lower dissociation constant (i.e. with the higher affinity for the two proteins), followed by MeCbl and lastly CNCbl. The stronger affinity of AdoCbl likely arises from additional enthalpically favorable hydrogen bonds that the adenosyl group can form, thus enhancing stability and increasing affinity without causing major rearrangements of the protein backbone. A stronger binding of AdoCbl can reduce the conformational flexibility of the protein–Cbl complex more effectively than the MeCbl, mirroring the stabilizing effects observed in thermal assays. The different flexibilities of the MMACHC–MeCbl and MMACHC–AdoCbl complexes were confirmed by SAXS experiments performed by our group, that revealed that the MMACHC–AdoCbl complex appears more compact and less flexible than the MMACHC–MeCbl complex [124]. On the other hand, unlike the adenosyl or methyl cobalamin forms, where the relatively weaker cobalt–ligand bonds allow a more adaptable and accommodating interaction with MMACHC, the strong cobalt–cyano bond in CNCbl might restrict the conformational adjustments necessary for optimal binding. This rigidity may result in fewer overall energetically favorable protein–ligand contacts, contributing to a less-stable complex, as also hypothesized by Xu et al. [125]. Moreover, it is worth noting that CNCbl is not a natural ligand and therefore, while the protein is evolutionarily fine-tuned to bind adenosyl and methyl ligands, the cyanide form fails to establish equally favorable interactions.

In the case of MMACHC-R161Q, the stabilization and affinity order observed for the wild type is respected, but a lower stabilization (Fig. 29B) and reduced affinity are observed. A plausible explanation for the distorted cobalamin-binding is that the modified local environment around the glutamine 161 in the mutant triggers conformational changes that propagate throughout the protein, reaching the cobalamin-binding site. Since arginine 161 does not directly interact with cobalamin, we propose that the local environment of arginine 161, which is located in the GSH-binding site, is connected to the cobalamin pocket by a dynamic mechanism that likely plays a pivotal role in regulating the protein's function.

This direct measurement of the impaired Cbl-binding observed for the mutant could result from alterations in the global conformational stability induced by the mutation, as previously investigated by using an extrinsic dye fluorescence-based thermal shift assay or turbidity assays [52], [54]. In those works, by using a single transition model for analyzing the thermal unfolding process, the MMACHC-R161Q mutant was shown to unfold at a temperature about 2 °C lower than the wild-type protein. In this PhD research project, we investigated the MMACHC-WT and MMACHC-R161Q conformational stability by using DSC. Notably, these DSC data allowed us to unveil a more complex unfolding process in both proteins with the presence of conformational intermediate states (Fig. 27, Table 2).

While the three-state model for wild-type protein denaturation was originally proposed by Froese et al. as a theoretical framework based on the shape of the denaturation curve [52], our study provides experimental verification of this model. Moreover, DSC revealed that the MMACHC-R161Q mutant unfolds according to a two-transition model as well. However, while the two transitions in the wild-type protein occur at very distinct temperatures, giving rise to separate peaks in the DSC thermogram, the two unfolding temperatures in the mutant are very close, resulting in a broader single apparent peak. This result suggests that the intermediate conformational states could show a different stability or be differently populated, leading to an unfolding process with different cooperativity. Comparable unfolding enthalpy and temperature values for the first transition suggest that the first intermediate is stabilized to a similar extent in both proteins. In contrast, the reduced unfolding enthalpy and temperature observed for the second transition in the mutant suggest that its principal intermediate state is either less stable or structurally distinct from that of the wild type, potentially contributing to a facilitated overall unfolding process, as can be also observed when calculating the populations of the different states as a function of temperature for MMACHC-WT and MMACHC-R161Q (Fig. 28).

From that detailed description, it can be seen that, although the MMACHC-R161Q populates significantly both intermediate states, the overall unfolding cooperativity of MMACHC-WT is much lower than that of MMACHC-R161Q, because of the larger separation between the folded and unfolded states in temperature for the former, a gap that is occupied by a considerably populated stable first intermediate.

We also demonstrated that, unlike the wild type, these closer transitions in the mutant were not detectable by a spectroscopic assay such as CD (Fig. 26), which could only resolve a single unfolding curve, thus confirming the power of using DSC in providing deeper insights into the protein conformational landscape. Differences in the intermediate conformational populations

between the two proteins may underline the distinct isothermal denaturation curves observed by SYPRO Orange fluorescence emission upon incubation with the two apoproteins over time (Fig. 48). The specific affinities of the unfolding intermediates for the dye are responsible for the observed denaturation profile [120]. Differences in stability between the wild type and mutant proteins can also be detected by Molecular Dynamics, studying the behavior of the two apoproteins at both room and high temperatures. The comparison of the simulations of MMACHC-WT and MMACHC-R161Q at 303 K showed a marked instability of the mutant structure, mainly driven by the disordered regions, that evolves to a configuration that likely unfavour the binding to the cobalamin (Fig. 41). Of note, the MD trajectories also helped us rationalize the failure in producing the recombinant MMACHC-G147A mutant as a soluble protein, since the simulation showed the attainment of a severely misfolded conformation (Fig. 61), that likely leads to protein aggregation and precipitation. This result, together with the evidence of the insolubility of the other two variants (MMACHC-Y130C and MMACHC-R206P) that hampered the recombinant production, again confirms that a single point mutation can have significant structural effects that impair the global stability of the resulting protein, ultimately leading to a conformational disease. In addition, useful insights on the different unfolding pathways of MMACHC-WT and MMACHC-R161Q were obtained simulating temperature jumps by Molecular Dynamics. Indeed, although these jumps do not induce the complete unfolding of the proteins, they provide insights into differences in intermediate unfolding conformations. Despite the loss in secondary structure between the two proteins, wild type and R161Q mutant, is similar, the RMSD of the mutant increased significantly over a simulation period of one microsecond compared to the wild type. This indicates greater instability in the mutant tertiary structure of unfolding conformational intermediates (Fig. 30A). This instability in the tertiary structure may be attributed to either a reduction in molecular compactness or an enhanced propensity for aggregation, in good agreement with DLS results from our laboratory, that showed that apo MMACHC-WT was approximately 12 % smaller than the mutant apo MMACHC-R161Q, and SAXS experiments that revealed a higher flexibility and reduced structural compactness of the mutant [126].

In order to observe structural differences between MMACHC-WT and MMACHC-R161Q with the available experimental techniques it is necessary to induce a thermal stress. Indeed, while the secondary structure content of the two proteins shows minimal differences (Fig. 24) and the native fluorescence together with the near-UV CD spectra (Fig. 25) do not suggest significant differences in the aromatic residues environments at 20 °C, we found that the unfolding pathway of the two proteins is significantly different. Hence, we propose the R161Q

substitution as a “subtle” mutation, that, removing a critical positive charge given by the arginine, induces the alteration of local domains (as also suggested by the decrease of the quantum yields in the fluorescence spectra, Fig. 25B) that likely increases the flexibility of the mutant protein, as observed by SAXS and MD, and that could be confirmed by the study of the fluorescence lifetimes [84] in both MMACHC-WT and MMACHC-R161Q. It is well-established that protein residues are coupled to each other through both the hydrogen-bond network and packing interactions, leading to correlated motions or fluctuations in equilibrium that are critical for function [127]. While these alterations are not detectable observing the signal given by the average static structure, they became evident studying the conformational landscape or the binding to the natural ligands, suggesting that these alterations are not exclusively confined to the specific aminoacid location but propagate throughout the protein, influencing its dynamics and ultimately its key functions [127], [128]. Unfortunately, our studies do not give insights into the domains that characterize the two-transition unfolding. It would be of high interest to know more about the fragile domain of the mutant that make it so unstable. Other experimental techniques, like NMR spectroscopy, could be applied as it is able to resolve the dynamic structural details in a native-like environment [129].

Another important finding from this PhD research experiments was the reduced ability of MMACHC-R161Q to form dimers and tetramers compared to MMACHC-WT. It has been reported that MMACHC is able to form domain-swap homodimers in the presence of AdoCbl, and, from these, also tetrameric structures can form [62], [73]. Through native gel electrophoresis and size-exclusion chromatography, we found that, while MMACHC-R161Q retains the ability to form dimers, their abundance is strongly reduced compared to the wild-type protein (Fig. 43,44), also in accordance with static light scattering data from our laboratory [126]. This finding suggests that the changes in the Cbl-binding region render the MMACHC-R161Q unable to adopt the correct conformation to engage in subunit exchange, leading to a reduced dimerization efficiency. Additionally, native gel electrophoresis (Fig. 43) revealed that, in the case of MMACHC-WT, the addition of GSH to the protein-AdoCbl complex further increased dimer and tetramer formation, highlighting the functional and structural interplay between different regions of the protein. Again, testing the effect of MeCbl and CNCbl on the oligomeric equilibrium, we found that the propensity for dimerization in the presence of the different cobalamins mirrors the affinity ranking, and that, when driven by a higher affinity, a larger number of dimers is formed, which prompt the organization of even-order oligomers in the case of the wild type (Fig. 45).

Structural and biophysical studies have shown that protein dimerization plays a key role in regulating protein function [130]. Evidences from this research experiments indicate that MMACHC dimers form in the presence of essential cofactors, such as vitamin B12 and GSH. These observations provide indirect support for the idea that dimer formation represents a structural protein reorganization, and an additional regulation mechanism, necessary for this enzyme's proper functioning. Hence, the inability to form dimers in a pathological mutant further supports this hypothesis, although it is clear that further experiments are needed to fully understand the exact functional role of dimeric conformations.

Finally, part of this research project was devoted to shed light on the potential role of betaine (N-trimethylglycine) in the context of *cblC* disease, offering a new perspective beyond its conventional metabolic effect. Clinically, betaine is an established adjunct therapy for *cblC* patients, primarily used to lower elevated homocysteine levels by serving as a methyl donor in the betaine-homocysteine methyltransferase pathway [121]. It is known that small organic osmolytes like betaine can stabilize proteins against thermal denaturation without specific binding. Betaine and related osmolytes are preferentially excluded from the protein surface, thus increasing the water activity and favoring the compact native conformation and preventing unfolding [131], [132]. Given the reduced thermal stability exhibited by some mutant proteins involved in common inborn metabolic diseases, the use of chemical chaperones such as glycerol, proline, betaine, and trimethylamine N-oxide (TMAO) has been shown to partially rescue these proteins both *in vitro* and *in vivo* [133]. Our findings demonstrated that among the different tested osmolytes, only betaine increases the thermal stability of the MMACHC-R161Q mutant (Fig. 49B, 50B). Moreover, our results showed that betaine's general protein-stabilizing properties can partially restore the enzymatic functionality, as assessed *in vitro* (Fig. 51). This represents a proof-of-principle that enhancing protein stability could be a viable strategy for improving the impaired enzymatic activity in *cblC*, as resulting from MMACHC pathological mutants.

A potential next step from a therapeutic perspective could involve the identification of pharmacological chaperones—molecules capable to specifically bind to MMACHC mutants, increasing its thermal stability and stabilizing its correct folded and active state—through high-throughput screening of small-molecule libraries. In this context, preliminary results consisted in the identification of three small molecules able to bind MMACHC-R161Q mutant protein in the micromolar range of affinity, with two of them characterized by an enthalpically-driven binding, usually more suitable for drug-like candidates since it reflects specific and polar interactions between the compound and target [134]. Moreover, although these molecules

showed the ability to stabilize the mutant protein *in vitro*, the enzymatic assay performed in their presence did not lead to an improvement of the mutant functionality (Fig. 54B, 57) as hoped. However, an important aspect to consider when studying small molecules capable of binding pathological mutants is that their effect observed on isolated and purified protein does not necessarily reflect their functional impact in a more complex cellular context. *In vitro* enzymatic assays indeed typically measure the intrinsic catalytic activity of already folded proteins under highly controlled conditions, without the influence of cellular quality-control systems that play a pivotal role in determining the amount of functional protein that is ultimately available. An exemplificative case is migalastat, a pharmacological chaperone used in the treatment of Fabry disease: although it acts as a competitive inhibitor of recombinant purified α-galactosidase A, in cells it stabilizes certain misfolded variants during folding in the endoplasmic reticulum, reduces premature degradation, and promotes lysosomal trafficking, resulting in increased intracellular enzymatic activity [135]. For this reason, together with a more extensive search of small molecules from virtual or chemical libraries to obtain more candidates, it is necessary to establish a more complex model system to test the most promising molecules.

6. Conclusions and future perspectives

The results obtained within this PhD research project study provides novel insights into the thermodynamics underlying MMACHC stability and the impact of disease-associated mutations on its structure, its oligomeric organization and cofactors-binding properties. The R161Q mutation impairs key protein functions, including GSH and Cbl binding, dimerization, and protein stability, which directly contribute to the reduced enzymatic activity. Moreover, the obtained results elucidated how different forms of cobalamin modulate these molecular properties. We demonstrated that a single point mutation, although located at the GSH-binding pocket, produces structural alterations that propagate throughout the protein. By studying the unfolding process of MMACHC-WT and MMACH-R161Q we demonstrated the existence and thermodynamic properties of unfolding intermediates, and the lessened stability of the main unfolding intermediate in the case of the mutant. It would be of high interest to structurally characterize these intermediates by NMR, to identify the molecular causes of the mutant instability. By unveiling these molecular changes, we also demonstrated the potential therapeutic benefit of using osmolytes, specifically betaine, to enhance the thermal stability of the mutant protein and partially restore its function. Our findings suggest that targeting protein stability, through the use of small molecules with specific stabilizing effects, holds promise as a novel therapeutic strategy for *cblC* disease and other related inborn metabolic disorders. Further research, particularly into the identification of pharmacological chaperones, could pave the way for developing effective treatments aimed at stabilizing MMACHC and improving its function in *cblC* patients carrying mutations that destabilize the protein structure. In this regard, considering the limitations of the evaluation of the therapeutic effect in tube, it is necessary to test the effect of the identified molecules on cellular models, such as human cells genetically-edited by CRISPR/Cas9 to carry the c.482G>A (R161Q) or other point mutations, or fibroblasts derived from *cblC* patients, to evaluate the reversion of the pathological phenotype (i.e. the normalization of methylmalonic acid and homocystinuria levels) by mass spectrometry analysis.

Furthermore, considering the high incidence rate of nonsense mutations found in *cblC* patients, that seem not to be associated to nonsense RNA mediating decaying and thus leading to protein production, we proposed to evaluate the efficacy of TRIDs, molecules capable of restoring the

production of the full-length protein. In this framework, we generated the reporter systems for c.394C>T (R132X) and c.666C>A (Y222X) mutations that allow to evaluate the efficacy of these molecules in cell models, and established a collaboration with Professor Laura Lentini's laboratory (University of Palermo, Italy) to test the effect of three novel 1,2,4-oxadiazole compounds, already tested for other rare conditions. The preliminary results obtained are promising and we aim to translate them on more sophisticated models, such as organoids derived from pluripotent induced stem cells, generated from patients' fibroblast harbouring the same mutations, in collaboration with Professor Esra Erdal (Izmir Biomedicine and Genome Center, Turkey) within the granted project "EXploring therapeutic strategies for cblC Disease: Italy-Turkey collaboration".

Altogether, the results obtained within thid PhD thesis work provide a comprehensive framework for understanding the molecular basis of MMACHC dysfunction and suggest new viable avenues for the development of targeted therapeutic strategies in *cblC* disease. Although significant work remains to do to bridge the gap between *in vitro* observations and clinical applications, our findings establish a solid foundation for the development of innovative treatments that could substantially improve the management and quality of life of patients affected by this rare but severe metabolic disorder and that can be translated to other rare conditions.

7. Bibliography

[1] Stubbe J. Binding Site Revealed of Nature's Most Beautiful Cofactor. *Science* 1994;266(5191):1663-1664. doi:10.1126/science.7992049

[2] Hodgkin DC, Kamper J, Mackay M, Pickworth J, Trueblood KN, White JG. Structure of Vitamin B12. *Nature*. 1956;178(4524):64-66. doi:10.1038/178064a0

[3] Kräutler B. Vitamin B12: chemistry and biochemistry. *Biochemistry Society Transaction* 2005;33(4):806-810. doi:10.1042/BST0330806

[4] Firth RA, Hill HAO, Pratt JM, Williams RJP, Jackson WR. The Circular Dichroism and Absorption Spectra of Some Vitamin B12 Derivatives. *Biochemistry*. 1967;6(7):2178-2189. doi:10.1021/bi00859a040

[5] Martens JH, Barg H, Warren MJ, Jahn, D. Microbial production of vitamin B 12. *Applied Microbiology and Biotechnol*ogy 2002;58(3):275-285. doi:10.1007/s00253-001-0902-7

[6] Backstrand JR. Quantitative approaches to nutrient density for public health nutrition. *Public Health* Nutrition 2003;6(8):829-837. doi:10.1079/PHN2003507

[7] Sennett C, Rosenberg LE, Mellman IS. Transmembrane Transport of Cobalamin in Prokaryotic and Eukaryotic Cells. *Annual Review of Biochemistry* 1981;50(1):1053-1086. doi:10.1146/annurev.bi.50.070181.005201

[8] Gherasim C, Lofgren M, Banerjee R. Navigating the B12 Road: Assimilation, Delivery, and Disorders of Cobalamin. *Journal of Biological Chemistry*. 2013;288(19):13186-13193. doi:10.1074/jbc.R113.458810

[9] Beedholm-Ebsen R, van de Wetering K, Hardlei T, Nexø E, Borst P, Moestrup SK. Identification of multidrug resistance protein 1 (MRP1/ABCC1) as a molecular gate for cellular export of cobalamin. *Blood*. 2010;115(8):1632-1639. doi:10.1182/blood-2009-07-232587

[10] McCorvie TJ, Ferreira D, Yue WW, Froese DS. The complex machinery of human cobalamin metabolism. *Journal of Inherited Metabolic Disease* 2023;46(3):406-420. doi:10.1002/jimd.12593

[11] Banerjee R, Ragsdale SW. The Many Faces of Vitamin B12: Catalysis by Cobalamin-Dependent Enzymes. *Annual Review of Biochemistry* 2003;72(1):209-247. doi:10.1146/annurev.biochem.72.121801.161828

[12] Banerjee R, Gouda H, Pillay S. Redox-Linked Coordination Chemistry Directs Vitamin B12 Trafficking. *Accounts of Chemical Research* 2021;54(8):2003-2013. doi:10.1021/acs.accounts.1c00083

[13] Youngdahl-Turner P, Mellman IS, Allen RH, Rosenberg LE. Protein mediated vitamin uptake. *Experimental Cell Research* 1979;118(1):127-134. doi:10.1016/0014-4827(79)90590-1

[14] Banerjee R, Gherasim C, Padovani D. The tinker, tailor, soldier in intracellular B12 trafficking. *Current Opinion in Chemical Biology* 2009;13(4):484-491. doi:10.1016/j.cbpa.2009.07.007

[15] Rosenblatt DS, Hosack A, Matiaszuk NV, Cooper BA, Laframboise R. Defect in Vitamin B12 Release from Lysosomes: Newly Described Inborn Error of Vitamin B12 Metabolism. *Science* 1985;228(4705):1319-1321. doi:10.1126/science.4001945

[16] Lerner-Ellis JP, Tirone JC, Pawelek PD, et al. Identification of the gene responsible for methylmalonic aciduria and homocystinuria, cblC type. *Nature Genetics* 2006;38(1):93-100. doi:10.1038/ng1683

[17] Coelho D, Suormala T, Stucki M, et al. Gene Identification for the cblD Defect of Vitamin B12 Metabolism. *New England Journal of Medicine* 2008;358(14):1454-1464. doi:10.1056/NEJMoa072200

[18] Jusufi J, Suormala T, Burda P, Fowler B, Froese DS, Baumgartner MR. Characterization of functional domains of the cblD (MMADHC) gene product. *Journal of Inherited Metabolic Disease* 2014;37(5):841-849. doi:10.1007/s10545-014-9709-4

[19] Gherasim C, Hannibal L, Rajagopalan D, Jacobsen DW, Banerjee R. The C-terminal domain of CblD interacts with CblC and influences intracellular cobalamin partitioning. *Biochimie* 2013;95(5):1023-1032. doi:10.1016/j.biochi.2013.02.003

[20] Watkins D, Ru M, Hwang HY, Kim CD, Murray A et al. Hyperhomocysteinemia Due to Methionine Synthase Deficiency, cblG: Structure of the MTR Gene, Genotype Diversity, and Recognition of a Common Mutation, P1173L. *The American Journal of Human Genetics* 2002;71(1):143-153. doi:10.1086/341354

[21] Lempp TJ, Suormala T, Siegenthaler R, Baumgartner ER, Fawler B et al. Mutation and biochemical analysis of 19 probands with mut0 and 13 with mut− methylmalonic aciduria: Identification of seven novel mutations. *Molecular Genetics and Metabolism* 2007;90(3):284-290. doi:10.1016/j.ymgme.2006.10.002

[22] Dixon MM, Huang S, Matthews RG, Ludwig M. The structure of the C-terminal domain of methionine synthase: presenting S-adenosylmethionine for reductive methylation of B12. *Structure* 1996;4(11):1263-1275. doi:10.1016/S0969-2126(96)00135-9

[23] Leal NA, Park SD, Kima PE, Bobik TA. Identification of the Human and Bovine ATP:Cob(I)alamin Adenosyltransferase cDNAs Based on Complementation of a Bacterial Mutant. *Journal of Biological Chemistry* 2003;278(11):9227-9234. doi:10.1074/jbc.M212739200

[24] Dobson CM, Wai T, Leclerc D, et al. Identification of the gene responsible for the cblA complementation group of vitamin B12 responsive methylmalonic acidemia based on analysis of prokaryotic gene arrangements. *Proceedings of the National Academy of Sciences* 2002;99(24):15554-15559. doi:10.1073/pnas.242614799

[25] Froese DS, Fowler B, Baumgartner MR. Vitamin B12, folate, and the methionine remethylation cycle—biochemistry, pathways, and regulation. *Journal of Inherited Metabolic Disease* 2019;42(4):673-685. doi:10.1002/jimd.12009

[26] Rosenblatt DS, Cooper BA. Inherited disorders of vitamin B12 metabolism. *Blood Reviews* 1987;1(3):177-182. doi:https://doi.org/10.1016/0268-960X(87)90033-6

[27] Gravel RA, Mahoney MJ, Ruddle FH, Rosenberg LE. Genetic complementation in heterokaryons of human fibroblasts defective in cobalamin metabolism. *Proceedings of the National Academy of Sciences* 1975;72(8):3181-3185. doi:10.1073/pnas.72.8.3181

[28] Hannibal L, Kim J, Brasch NE, et al. Processing of alkylcobalamins in mammalian cells: A role for the MMACHC (cblC) gene product. *Molecular Genetics and Metabolism* 2009;97(4):260-266. doi:10.1016/j.ymgme.2009.04.005

[29] Lerner-Ellis JP, Tirone JC, Pawelek PD, Doré C, Atkinson JL et al. Identification of the gene responsible for methylmalonic aciduria and homocystinuria, cblC type. *Nature Genetics* 2006;38(1):93-100. doi:10.1038/ng1683

[30] Wiedemann A, Oussalah A, Lamireau N, Theron N, Julien M et al. Clinical, phenotypic and genetic landscape of case reports with genetically proven inherited disorders of vitamin B12 metabolism: A meta-analysis. *Cell Reports Medicine* 2022;3(7):100670. doi:https://doi.org/10.1016/j.xcrm.2022.100670

[31] Sloan JL, Carrillo N, Adams D, Venditti CP. Disorders of Intracellular Cobalamin Metabolism *In: GeneReviews, Adam MP, Feldman J, Mirzaa GM, Pagon RA, Wallace SE, Amemiya A editors, Seattle (WA): University of Washington* 1993. PMID: 20301503.

[32] Carrillo-Carrasco N, Chandler RJ, Venditti CP. Combined methylmalonic acidemia and homocystinuria, cblC type. I. Clinical presentations, diagnosis and management. *Journal of Inherited Metabolic Disease* 2012;35(1):91-102. doi:10.1007/s10545-011-9364-y

[33] Rosenblatt DS, Aspler AL, Shevell MI, Pletcher BA, Fenton WA, Seashore MR. Clinical heterogeneity and prognosis in combined methylmalonic aciduria and homocystinuria (cblC). *Journal of Inherited Metabolic Disease* 1997;20(4):528-538. doi:10.1023/A:1005353530303

[34] Arhip L, Brox-Torrecilla N, Romero I, Motilla M, Serrano-Moreno C, Miguélez M, Cuerda C. Late-onset methylmalonic acidemia and homocysteinemia (cblC disease): systematic review. *Orphanet Journal of Rare Diseases* 2024;*19*(1), 20. https://doi.org/10.1186/s13023-024-03021-3

[35] Weisfeld-Adams JD, Bender HA, Miley-Åkerstedt A, Frempong T, Schrager NL et al. Neurologic and neurodevelopmental phenotypes in young children with early-treated combined methylmalonic acidemia and homocystinuria, cobalamin C type. *Molecular Genetics and Metabolism* 2013;110(3):241-247. doi:10.1016/j.ymgme.2013.07.018

[36] Bonafede L, Ficicioglu CH, Serrano L, Han G, Morgan GIW et al. Cobalamin C Deficiency Shows a Rapidly Progressing Maculopathy With Severe Photoreceptor and Ganglion Cell Loss. *Investigative Opthalmology & Visual Science* 2015;56(13):7875. doi:10.1167/iovs.15-17857

[37] Richard E, Jorge-Finnigan A, Garcia-Villoria J, Merinero B, Desviat LR et al. Genetic and cellular studies of oxidative stress in methylmalonic aciduria (MMA) cobalamin deficiency type C (*cblC*) with homocystinuria (MMACHC). *Human Mutation* 2009;30(11):1558-1566. doi:10.1002/humu.21107

[38] Hannibal L, DiBello PM, Yu M, Miller A, Wang S et al. The MMACHC proteome: Hallmarks of functional cobalamin deficiency in humans. *Molecular Genetics and Metabolism* 2011;103(3):226-239. doi:10.1016/j.ymgme.2011.03.008

[39] Hannibal L, Dibello PM, Jacobsen DW. Proteomics of vitamin B12 processing *Clinical Chemistry and Laboratory Medicine* 2013;51(3):477-88. doi:10.1515/cclm-2012-0568

[40] Esser AJ, Mukherjee S, Dereven'kov IA, Makarov SV, Jacobsen DW et al. Versatile enzymology and heterogeneous phenotypes in cobalamin complementation type C disease. *iScience*. 2022;25:104981. doi.org/10.1016/j.isci.2022.104981

[41] Lerner-Ellis JP, Anastasio N, Liu J, Coelho D, Suormala T et al. Spectrum of mutations in MMACHC, allelic expression, and evidence for genotype-phenotype correlations. *Human Mutation* 2009;30(7):1072-1081. doi:10.1002/humu.21001

[42] Wang C, Li D, Cai F, Zhang X, Xu X et al. Mutation spectrum of MMACHC in Chinese pediatric patients with cobalamin C disease: A case series and literature review. *European Journal of Medical Genetics* 2019;62(10):103713. doi:10.1016/j.ejmg.2019.103713

[43] Landrum MJ, Lee JM, Benson M, Brown GR, Chao C et al. ClinVar: improving access to variant interpretations and supporting evidence. *Nucleic Acids Research* 2018;46(D1):D1062-D1067. doi:10.1093/nar/gkx1153

[44] Dionisi-Vici C, Martinelli D, Ceravolo F, Boenzi S, Pastore A. Optimizing the dose of hydroxocobalamin in cobalamin C (cblC) defect. *Molecular Genetics and Metabolism* 2013;109(4):329-330. doi:10.1016/j.ymgme.2013.05.013

[45] Huemer M, Diodato D, Schwahn B, Schiff M, Bandeira A et al. Guidelines for diagnosis and management of the cobalamin-related remethylation disorders cblC, cblD, cblE, cblF, cblG, cblJ and MTHFR deficiency. *Journal of Inherited Metabolic Disease* 2017;40(1):21-48. doi:10.1007/s10545-016-9991-4

[46] Wingert V, Mukherjee S, Esser AJ, Behringer S, Tanimowo S et al. Thiolatocobalamins repair the activity of pathogenic variants of the human cobalamin processing enzyme CblC. *Biochimie* 2021;183:108-125. doi:10.1016/j.biochi.2020.10.006

[47] Liguori L, Monticelli M, Allocca M, Mele BH, Lukas J et al. Pharmacological Chaperones: A Therapeutic Approach for Diseases Caused by Destabilizing Missense Mutations. *International Journal of Molecular Sciences* 2020;21(2):489. doi:10.3390/ijms21020489

[48] Damy T, Garcia-Pavia P, Hanna M, Judge DP, Merlini G et al. Efficacy and safety of tafamidis doses in the Tafamidis in Transthyretin Cardiomyopathy Clinical Trial ATTR-ACT and long-term extension study. *European Journal of Heart Failure* 2021;23(2):277-285. doi:10.1002/ejhf.2027

[49] Fiore M, Picco C, Moran O. Correctors modify the bicarbonate permeability of F508del-CFTR. *Scientific Reports* 2020;10(1):8440. doi:10.1038/s41598-020-65287-4

[50] Majtan T, L. Pey A, Ereño-Orbea J, Martínez-Cruz LA, Kraus JP. Targeting Cystathionine Beta-Synthase Misfolding in Homocystinuria by Small Ligands: State of the Art and Future Directions. *Current Drug Target*. 2016;17(13):1455-1470. doi:10.2174/1389450117666160302094910

[51] Clarke JTR. *Treatment In: A Clinical Guide to Inherited Metabolic Diseases, Cambridge University Press* 2005; 297-393. ISBN: 9780511544682 doi:10.1017/CBO9780511544682

[52] Froese DS, Healy S, McDonald M, Kochan G, Opperman U et al. Thermolability of mutant MMACHC protein in the vitamin B12-responsive cblC disorder. *Molecular Genetics and Metabolism* 2010;100(1):29-36. doi:10.1016/j.ymgme.2010.02.005

[53] Passantino R, Mangione MR, Ortore MG, Costa MA, Provenzano A et al. Investigation on a MMACHC mutant from cblC disease: The c.394C>T variant. *Biochimica et Biophysica Acta Proteins and Proteomics* 2022;1870(6). doi:10.1016/j.bbapap.2022.140793

[54] Gherasim C, Ruetz M, Li Z, Hudolin S, Banerjee R. Pathogenic mutations differentially affect the catalytic activities of the human B12-processing chaperone CblC and increase futile redox cycling. *Journal of Biological Chemistry* 2015;290(18):11393-11402. doi:10.1074/jbc.M115.637132

[55] Nagel-Wolfrum K, Möller F, Penner I, Baasov T, Wolfrum U. Targeting Nonsense Mutations in Diseases with Translational Read-Through-Inducing Drugs (TRIDs). *BioDrugs* 2016;30(2):49-74. doi:10.1007/s40259-016-0157-6

[56] Torices L, de las Heras J, Arango-Lasprilla JC, Cortés JM, Nunes-Xavier CE, Pulido R. MMADHC premature termination codons in the pathogenesis of cobalamin D disorder: Potential of translational readthrough reconstitution. *Molecular Genetics and Metabolism Reports* 2021;26:100710. doi:10.1016/j.ymgmr.2021.100710

[57] Campofelice A, Lentini L, Di Leonardo A, Melfi R, Tutone M et al. Strategies against Nonsense: Oxadiazoles as Translational Readthrough-Inducing Drugs (TRIDs). *International Journal of Molecular Sciences* 2019;20(13):3329. doi:10.3390/ijms20133329

[58] Branchini A, Ferrarese M, Campioni M, Castaman G, Mari R et al. Specific factor IX mRNA and protein features favor drug-induced readthrough over recurrent nonsense mutations. *Blood* 2017;129(16):2303-2307. doi:10.1182/blood-2016-09-738641

[59] Pibiri I, Melfi R, Tutone M, Di Leonardo A, Pace A, Lentini L. Targeting Nonsense: Optimization of 1,2,4-Oxadiazole TRIDs to Rescue CFTR Expression and Functionality in Cystic Fibrosis Cell Model Systems. *International Journal of Molecular Sciences* 2020;21(17):6420. doi:10.3390/ijms21176420

[60] Xue X, Mutyam V, Thakerar A, Mobely J, Briges RJ et al. Identification of the amino acids inserted during suppression of CFTR nonsense mutations and determination of their functional consequences. *Human Molecular Genetics* 2017;26(16):3116-3129. doi:10.1093/hmg/ddx196

[61] Koutmos M, Gherasim C, Smith JL, Banerjee R. Structural basis of multifunctionality in a vitamin B12-processing enzyme. *Journal of Biological Chemistry* 2011;286(34):29780-29787. doi:10.1074/jbc.M111.261370

[62] Froese DS, Krojer T, Wu X, Shrestha R, Kiyani W et al. Structure of MMACHC reveals an arginine-rich pocket and a domain-swapped dimer for its B12 processing function. *Biochemistry* 2012;51(25):5083-5090. doi:10.1021/bi300150y

[63] Ruetz M, Shanmuganathan A, Gherasim C, Karasik A, Salchner R, et al. Antivitamin B12 Inhibition of the Human B12-Processing Enzyme CblC: Crystal Structure of an Inactive Ternary Complex with Glutathione as the Cosubstrate. *Angewandte Chemie International Edition* 2017;56(26):7387-7392. doi:10.1002/anie.201701583

[64] Deme JC, Hancock MA, Xia X, Shintre CA, Plesa M et al. Purification and interaction analyses of two human lysosomal vitamin B12 transporters: LMBD1 and ABCD4. *Molecular Membrane Biology* 2014;31(7-8):250-261. doi:10.3109/09687688.2014.990998

[65] Kim J, Hannibal L, Gherasim C, Jacobsen DW, Banerjee R. A human vitamin B12 trafficking protein uses glutathione transferase activity for processing alkylcobalamins. *Journal of Biological Chemistry* 2009;284(48):33418-33424. doi:10.1074/jbc.M109.057877

[66] Kim J, Gherasim C, Banerjee R. *Decyanation of Vitamin B 12 by a Trafficking Chaperone*. *Proceedings of the National Academy of Sciences* 2008;105(38):14551-14554. https://doi.org/10.1073/pnas.0805989105

[67] Froese DS, Zhang J, Healy S, Gravel RA. Mechanism of vitamin B12-responsiveness in cblC methylmalonic aciduria with homocystinuria. *Molecular Genetics and Metabolism* 2009;98(4):338-343. doi:https://doi.org/10.1016/j.ymgme.2009.07.014

[68] Wirt MD, Kumar M, Wu J, Scheuring, EM, Ragsdale, SW, Chance MR. Structural and Electronic Factors in Heterolytic Cleavage: Formation of the Co(I) Intermediate in the Corrinoid/Iron-Sulfur Protein from Clostridium thermoaceticum. *Biochemistry* 1995;34(15), 5269–5273. https://doi.org/10.1021/bi00015a042

[69] Li Z, Gherasim C, Lesniak NA, Banerjee R. Glutathione-dependent one-electron transfer reactions catalyzed by a B 12 trafficking protein. *Journal of Biological Chemistry* 2014;289(23):16487-16497. doi:10.1074/jbc.M114.567339

[70] Li Z, Mascarenhas R, Twahir UT, Kallon A, Deb A et al. An Interprotein Co-S Coordination Complex in the B12-Trafficking Pathway. *Journal of American Chemical Society* 2020;142(38):16334-16345. doi:10.1021/jacs.0c06590

[71] Bassila C, Ghemrawi R, Flayac J, Froese DS, Baumgartner MR et al. Methionine synthase and methionine synthase reductase interact with MMACHC and with MMADHC. *Biochimica et Biophysica Acta Molecular Basis of Disease* 2017;1863(1):103-112. doi:10.1016/j.bbadis.2016.10.016

[72] Moras E, Hosack A, Watkins D, Rosenblatt DS. Mitochondrial vitamin B12-binding proteins in patients with inborn errors of cobalamin metabolism. *Molecular Genetics and Metabolism* 2007;90(2), 140–147. https://doi.org/10.1016/j.ymgme.2006.08.014

[73] Froese DS, Kopec J, Fitzpatrick F, et al. Structural insights into the MMACHC-MMADHC protein complex involved in vitamin B12 trafficking. *Journal of Biological Chemistry*. 2015;290(49):29167-29177. doi:10.1074/jbc.M115.683268

[74] Backe PH, Ytre-Arne M, Røhr ÅK, Brodtkorb E, Fawler B et al. Novel deletion mutation identified in a patient with late-onset combined methylmalonic acidemia and homocystinuria, CBLC type *In: JIMD Reports, John Wiley & Sons* 2013;11:79-85. doi:10.1007/8904_2013_225

[75] Barany F. Genetic disease detection and DNA amplification using cloned thermostable ligase. *Proceedings of the National Academy of Sciences* 1991;88(1):189-193. doi:10.1073/pnas.88.1.189

[76] Picard V, Ersdal-Badju E, Lu A, Bock SC. A rapid and efficient one-tube PCR-based mutagenesis technique using *Pfu* DNA polymerase. *Nucleic Acids Research* 1994;22(13):2587-2591. doi:10.1093/nar/22.13.2587

[77] Charlton A, Zachariou M. Immobilized Metal Ion Affinity Chromatography of Histidine-Tagged Fusion Proteins. *Methods in Molecular Biology* 2008;421:137-150. doi:10.1007/978-1-59745-582-4_10

[78] Smith BJ. SDS Polyacrylamide Gel Electrophoresis of Proteins *In: Proteins*, Humana Press; 41-56. doi:10.1385/0-89603-062-8:41

[79] Pauling L, Corey RB, Branson HR. The structure of proteins: Two hydrogen-bonded helical configurations of the polypeptide chain. *Proceedings of the National Academy of Sciences* 1951;37(4):205-211 doi:10.1073/pnas.37.4.205.

[80] Kelly SM, Jess TJ, Price NC. How to study proteins by circular dichroism. *Biochimica et Biophysica Acta Proteins and Proteomics* 2005;1751(2):119-139 https://doi.org/10.1016/j.bbapap.2005.06.005

[81] Anfinsen CB. Principles that Govern the Folding of Protein Chains. *Science* 1979;181(4096):223-230 doi:10.1126/science.181.4096.223.

[82] Sancho J. The stability of 2-state, 3-state and more-state proteins from simple spectroscopic techniques... plus the structure of the equilibrium intermediates at the same time. *Archives of Biochemistry and Biophysics* 2013;531(1-2):4-13 doi:10.1016/j.abb.2012.10.014.

[83] Juzeniene A, Nizauskaite Z. Photodegradation of cobalamins in aqueous solutions and in human blood. *Journal of Photochemistry and Photobiology B: Biology* 2013;122:7-14 doi:10.1016/j.jphotobiol.2013.03.001.

[84] Dos Santos Rodrigues FH, Delgado GG, Santana da Costa T, Tasic L. Applications of fluorescence spectroscopy in protein conformational changes and intermolecular contacts. *BBA Advances* 2023;3. doi:10.1016/j.bbadva.2023.100091

[85] Jelesarov I, Bosshard HR. Isothermal titration calorimetry and differential scanning calorimetry as complementary tools to investigate the energetics of biomolecular recognition. *Journal of Molecular Recognition* 1999;12(1):3-18. doi:10.1002/(SICI)1099-1352(199901/02)12:1<3::AID-JMR441>3.0.CO;2-6

[86] Velázquez-Campoy A, Ohtaka H, Nezami A, Muzammil S, Freire E. Isothermal Titration Calorimetry. *Current Protocolos in Cell Biology* 2004;23(1). doi:10.1002/0471143030.cb1708s23

[87] Bastos M, Abian O, Johnson CM, et al. Isothermal titration calorimetry. *Nature Reviews Methods Primers* 2023;3(1):17. doi:10.1038/s43586-023-00199-x

[88] Sinha S, Tam B, Wang SM. Applications of Molecular Dynamics Simulation in Protein Study. *Membranes* 2022;12(9):844. doi:10.3390/membranes12090844

[89] Huang J, MacKerell AD. CHARMM36 all-atom additive protein force field: Validation based on comparison to NMR data. *Journal of Computational Chemistry* 2013;34(25):2135-2145. doi:10.1002/jcc.23354

[90] Pavlova A, Parks JM, Gumbart JC. Development of CHARMM-Compatible Force-Field Parameters for Cobalamin and Related Cofactors from Quantum Mechanical Calculations. *Journal of Chemical Theory and Computation* 2018;14(2):784-798. doi:10.1021/acs.jctc.7b01236

[91] Jo S, Kim T, Iyer VG, Im W. CHARMM-GUI: A web-based graphical user interface for CHARMM. *Journal of Computational Chemistry* 2008;29(11):1859-1865. doi:10.1002/jcc.20945

[92] Kim S, Lee J, Jo S, Brooks CL, Lee HS, Im W. CHARMM-GUI ligand reader and modeler for CHARMM force field generation of small molecules. *Journal of Computational Chemistry* 2017;38(21):1879-1886. doi:10.1002/jcc.24829

[93] Abraham MJ, Murtola T, Schulz R, et al. GROMACS: High performance molecular simulations through multi-level parallelism from laptops to supercomputers. *SoftwareX* 2015;1-2:19-25. doi:10.1016/j.softx.2015.06.001

[94] Toukmaji A, Sagui C, Board J, Darden T. Efficient particle-mesh Ewald based approach to fixed and induced dipolar interactions. *Journal of Chemical Physics* 2000;113(24):10913-10927. doi:10.1063/1.1324708

[95] Berk Hess, Henk Bekker, Herman J. C. Berendsen, Johannes G. E. M. Fraaije. LINCS: A linear constraint solver for molecular simulations. *Journal of Computational Chemistry* 1997;18(12):1463-1472.

[96] Ghosh J, Marru S, Singh N, Vanomesslaeghe K, Fan Y, Pamidighantam S. Molecular parameter optimization gateway (ParamChem) *In: Proceedings of the 2011 TeraGrid Conference: Extreme Digital Discovery*. ACM; 2011:1-8. doi:10.1145/2016741.2016779

[97] Humphrey W, Dalke A, Schulten K. VMD: Visual molecular dynamics. *Journal of Molecular Graphics* 1996;14(1):33-38. doi:10.1016/0263-7855(96)00018-5

[98] Gowers RJ, Linke M, Barnoud J, Reddy TGE, Melo MN et al. MDAnalysis: A Python Package for the Rapid Analysis of Molecular Dynamics Simulations *In: Proceedings of the 15th Python in Science Conference* 2016 https://doi.org/10.25080/Majora-629e541a-00e

[99] Wittig I, Braun HP, Schägger H. Blue native PAGE. *Nature Protocols* 2006;1(1):418-428. doi:10.1038/nprot.2006.62

[100] Schneider CA, Rasband WS, Eliceiri KW. NIH Image to ImageJ: 25 years of image analysis. *Nature Methods* 2012;9(7):671-675. doi:10.1038/nmeth.2089

[101] Paggi JM, Pandit A, Dror RO. The Art and Science of Molecular Docking. *Annual Review of Biochemistry* 2024;93(1):389-410. doi:10.1146/annurev-biochem-030222-120000

[102] Pettersen EF, Goddard TD, Huang CC, Meng EC, Couch GS et al. UCSF ChimeraX: Structure visualization for researchers, educators, and developers. *Protein Science* 2021;30(1):70-82. doi:10.1002/pro.3943

[103] Madhavi Sastry G, Adzhigirey M, Day T, Annabhimoju R, Sherman W. Protein and ligand preparation: Parameters, protocols, and influence on virtual screening enrichments. *Journal of Computer-Aided Molecular Design* 2013;27(3):221-234. doi:10.1007/s10822-013-9644-8

[104] Banks JL, Beard HS, Cao Y, Cho AE, Damm W et al. Integrated Modeling Program, Applied Chemical Theory (IMPACT). *Journal of Computational Chemistry* 2005;26(16):1752-1780. doi:10.1002/jcc.20292

[105] Jacobson MP, Pincus DL, Rapp CS, Day TGF, Honig B et al. A Hierarchical Approach to All-Atom Protein Loop Prediction. *Proteins: Structure, Function and Bioinformatics* 2004;55(2):351-367. doi:10.1002/prot.10613

[106] RC, Yao K, Kaplan Z, Chelliah M, Leswing K et al. Epik: p K_a and Protonation State Prediction through Machine Learning. *Journal of Chemical Theory and Computation* 2023;19(8):2380-2388. doi:10.1021/acs.jctc.3c00044

[107] Halgren TA. Identifying and characterizing binding sites and assessing druggability. *Journal of Chemical Information and Modeling* 2009;49(2):377-389. doi:10.1021/ci800324m

[108] Wishart DS, Feunang YD, Guo AC, et al. DrugBank 5.0: A major update to the DrugBank database for 2018. *Nucleic Acids Research* 2018;46(D1):D1074-D1082. doi:10.1093/nar/gkx1037

[109] Friesner RA, Murphy RB, Repasky MP, Frye LL, Greenword JR et al. Extra Precision Glide: Docking and Scoring Incorporating a Model of Hydrophobic Enclosure for Protein−Ligand Complexes. *Journal of Medicinal Chemistry* 2006;49(21):6177-6196. doi:10.1021/jm051256o

[110] Szalay AA, Mackey CJ, Langridge WHR. Restriction endonucleases and their applications. *Enzyme and Microbial Technology* 1979;1(3):154-164. doi:10.1016/0141-0229(79)90022-X

[111] Aaij C, Borst P. The gel electrophoresis of DNA. *Biochimica et Biophysica Acta - Nucleic Acids and Protein Synthesis* 1972;269(2):192–200. https://doi.org/10.1016/0005-2787(72)90426-1

[112] Chen Y, Lu H, Zhang N, Zhu Z, Wang S, Li M. PremPS: Predicting the impact of missense mutations on protein stability. *PLoS Computational Biology* 2020;16(12):e1008543. doi:10.1371/journal.pcbi.1008543

[113] Meharenna YT, Poulos TL. Using Molecular Dynamics To Probe the Structural Basis for Enhanced Stability in Thermal Stable Cytochromes P450. *Biochemistry* 2010;49(31):6680-6686. doi:10.1021/bi100929x

[114] Karplus M, McCammon JA. Molecular dynamics simulations of biomolecules. *Nature Structural Biology 2002*;*9*(9), 646–652. https://doi.org/10.1038/nsb0902-646

[115] Day R, Bennion BJ, Ham S, Daggett V. Increasing Temperature Accelerates Protein Unfolding Without Changing the Pathway of Unfolding. *Journal of Molecular Biology* 2002;322(1):189-203. doi:10.1016/S0022-2836(02)00672-1

[116] Antony P, Baby B, Ali A, Vijayan R, Al Jasmi F. Interaction of Glutathione with MMACHC Arginine-Rich Pocket Variants Associated with Cobalamin C Disease: Insights from Molecular Modeling. *Biomedicines* 2023;11(12). doi:10.3390/biomedicines11123217

[117] Hospital A, Goñi JR, Orozco M, Jelpí JL. Molecular dynamics simulations: advances and applications. *Advances and Applications in Bioinformatics and Chemistry* 2015;19(8):37-47 doi: 10.2147/AABC.S70333.

[118] Convertino M, Das J, Dokholyan NV. Pharmacological Chaperones: Design and Development of New Therapeutic Strategies for the Treatment of Conformational Diseases. *ACS Chemical Biology* 2016;11(6):1471-1489. https://doi.org/10.1021/acschembio.6b00195

[119] Niesen FH, Berglund H, Vedadi M. The use of differential scanning fluorimetry to detect ligand interactions that promote protein stability. *Nature Protocols* 2007;2(9):2212-2221. doi:10.1038/nprot.2007.321

[120] Sarver RW, Rogers JM, Epps DE. Determination of Ligand-MurB Interactions by Isothermal Denaturation: Applicatio as a Secondary Assay to Complement High Throughput Screening. *Journal of Biomolecular Screening* 2002;7(1):21-28. doi:10.1177/108705710200700104

[121] Imbard A, Toumazi A, Magréault S, et al. Efficacy and pharmacokinetics of betaine in CBS and cblC deficiencies: a cross-over randomized controlled trial. *Orphanet Journal of Rare Diseases* 2022;17(1). doi:10.1186/s13023-022-02567-4

[122] Singh A, Upadhyay V, Upadhyay AK, Singh SM, Panda AK. Protein recovery from inclusion bodies of Escherichia coli using mild solubilization process. *Microbial Cell Factories* 2015;14(1). doi:10.1186/s12934-015-0222-8

[123] de Marco A, Vigh L, Diamant S, Goloubinoff P. Native folding of aggregation-prone recombinant proteins in Escherichia coli by osmolytes, plasmid- or benzyl alcohol–overexpressed molecular chaperones. *Cell Stress Chaperones* 2005;10(4):329. doi:10.1379/CSC-139R.1

[124] Longo L, Costa MA, Carrotta R, Mangione MA, Martorana V et al. Modulation of conformational features and oligomerization of MMACHC by cobalamin variants: impact of the R161Q mutation in cblC disease. *European Biophysics Journal* 2025 doi:10.1007/s00249-025-01777-5

[125] Xu Q, Zhou H, Li M, Wang W, Xu M, et al. Structural Study of the Complex of cblC Methylmalonic Aciduria and Homocystinuria-Related Protein MMACHC with Cyanocobalamin *Crystals* 2022;12(4):468. doi:10.3390/cryst12040468

[126] Longo L, Randazzo L, Bollati M, Carrotta R, Costa MA et al. Missense mutations in MMACHC protein from cblC disease affect its conformational stability and vitamin B12-binding activity: The example of R161Q mutation. *Molecular Genetics and Metabolism* 2025;145(3):109150. doi:10.1016/j.ymgme.2025.109150

[127] Naganathan AN. Modulation of allosteric coupling by mutations: from protein dynamics and packing to altered native ensembles and function. *Current Opinion in Structural Biology* 2019;54:1-9. doi:10.1016/j.sbi.2018.09.004

[128] Popovych N, Sun S, Ebright RH, Kalodimos CG. Dynamically driven protein allostery. *Nature Structural and Molecular Biology* 2006;13(9):831-838. doi:10.1038/nsmb1132

[129] Kleckner IR, Foster MP. An introduction to NMR-based approaches for measuring protein dynamics. *Biochimica et Biophysica Acta Proteins and Proteomics* 2011;1814(8):942-968. doi:10.1016/j.bbapap.2010.10.012

[130] Marianayagam NJ, Sunde M, Matthews JM. The power of two: protein dimerization in biology. *Trends in Biochemical Sciences* 2004;29(11):618-625. doi:10.1016/j.tibs.2004.09.006

[131] Dandage R, Bandyopadhyay A, Jayaraj GG, Saxena K, Dalal V et al. Classification of Chemical Chaperones Based on Their Effect on Protein Folding Landscapes. *ACS Chemical Biology* 2015;10(3):813-820. doi:10.1021/cb500798y

[132] Street TO, Bolen DW, Rose GD. A molecular mechanism for osmolyte-induced protein stability. *Proceedings of the National Academy of Sciences* 2006;103(38):13997-14002. doi:10.1073/pnas.0606236103

[133] Yue WW. From structural biology to designing therapy for inborn errors of metabolism. *Journal of Inherited Metabolic Disease* 2016;39(4):489-498. doi:10.1007/s10545-016-9923-3

[134] Claveria-Gimeno R, Vega S, Abian O, Velazquez-Campoy A. A look at ligand binding thermodynamics in drug discovery. *Expert Opinion on Drug Discovery* 2017;12(4):363-377. doi:10.1080/17460441.2017.1297418

[135] Asano N, Ishii S, Kizu H, Ikeda K, Yasuda K et al. In vitro inhibition and intracellular enhancement of lysosomal α-galactosidase A activity in Fabry lymphoblasts by 1-deoxygalactonojirimycin and its derivatives. *European Journal of Biochemistry* 2000;267(13):4179-4186. doi:10.1046/j.1432-1327.2000.01457.x